Technical University of Munich
TUM School of Medicine and Health

Deciphering the role of the RNA-binding protein Staufen 1 and Staufen 2 in the biology of germinal centre B-cells

Francisco Osorio-Barrios

Complete reprint of the dissertation approved by the TUM School of Medicine and Health of the Technical University of Munich for the award of the Doktor der Naturwissenschaften (Dr. rer. nat).

Chair: Prof. Dr. Radu Roland Rad

Examiners:

1. Prof. Dr. Marc Schmidt-Supprian
2. Prof. Dr. Danny Nedialkova

The dissertation was submitted to the Technical University of Munich on 15 February 2024 and accepted by the TUM School of Medicine and Health on 8 May 2024.

dedicado mis padres

“No tengo porque estar de acuerdo con lo que pienso”
Carlos Caszely. Futbolista chileno.

“Plaudite, amici, comoedia finita est”
(Allegedly) Ludwig van Beethoven on his deathbed.

„Fußball ist wie Schach, nur ohne Würfel“
Jan Böhmermann, deutscher Satiriker

ACKNOWLEDGEMENTS

This doctoral Thesis could have never been possible without the International Max Planck Research School in Life Sciences (IMPRS-LS). My application was selected among more than 1000 other intenders, and I have always been grateful to the IMPRS office for noticing me after three years of applying to graduate schools around the world, in particular the members who are now in retirement: Hans-Jörg, Ingrid and Maxi. Their help was constant and precise, and their goodwill always made me feel appreciated, which is a rare treatment from an institution.

Through IMPRS-LS, I got to know Prof. Dr Marc Schmidt-Supprian, who accepted me in his group and supported my long stay in his lab, always ensuring funding, feedback, and a long list of experiments to perform. I will always remember my *Doktorvater* and his critical thinking, which undoubtedly increased the one I already had. After many years together, I understood his passion for B-cells, which changed my mind, and now I also think they are interesting. Related to Prof. Dr Marc Schmidt-Supprian, I also want to express my gratitude to his European Horizon ERC grant, which funded my stay in Germany, and all the cutting-edge expensive research I did, which could have been impossible in my homeland. Moreover, through Prof. Dr Marc Schmidt-Supprian, I also got to know Prof. Dr Martin Turner, who received me in his laboratory for a research stay funded by the European Molecular Biology Organisation. This institution should also receive my gratitude since it allowed me to meet the friendly Dr Twm Mitchell and perform irCLIP experiments together, the results of which suggested a molecular mechanism mediated by Staufen proteins in B-cells.

During my doctoral work at Prof. Dr Marc Schmidt-Supprian's group, I got the best role models that a *Doktorand* can get; I will always be impressed by the professionalism and hard work I observed in the laboratory by Dra. Valeria Soberón, Dra. Carina Diehl, Dra. Sabrina Bortoluzzi, Dra. Seren Baygün and Dra. Sabine Helmrath. The power of these women doing science is my strongest argument to declare that academia is such an unfair place.

Also, in the *Arbeitgruppe*, I want to thank the real motors that made the machine work: Dr Tim Ammon and Claudia Mugler. Tim was my supervisor on the ground, and from him, I always got neat advice and strategies to accomplish my aims and lovely conversations on private topics. When he left the lab, the hole could never be filled, and it probably never will. The only consolation is he found a brighter path where he is fully appreciated. The other critical engine, Claudia, was my fundamental column during those (almost) six years. She dealt with unpleasant paperwork and experiments that I never liked to do, and from her, I always got a friendly shoulder to rest. She brought me peace in the storm and company in the loneliness.

Following unpleasant work, I want to thank the people who have always helped me process primary samples: Laura Kraus and Gönül Seyhan. All my experiments were always massive, and I always found their hands to help me. A lot of the data presented in the first part of my thesis was only possible because they were up to help me— eternal gratitude.

Since not everything is about work, I also want to thank the motivated people who follow my socialising ideas, particularly Vanessa Gölling and Daniel Kovacs, who are funnily related. Vanessa is the best person to have next to you when you have an idea because you can rely on *it* to happen and with high standards. Despite Daniel's not being that efficient, I found in him a German friend who was always there in the darkest and brightest moments. He was my moral support for many years. My companion in workshops, beers, movies, and much more… Orthogonal to these people, other motivated people who fancy joining our social events are

Ali Majesdi and Chia-I Lien, who were also part of the best office in the entire TranslaTUM building, who brought their enjoyable inner peace or rage into the table. I am grateful for getting them to know deeper.

Many more people come to my mind at the end: other technicians who helped me initially and all the professionals and HiWis working in the mice facility who made my life a bit easier. However, it is challenging to summarise six years of work and list all the people involved. Despite that, I feel the responsibility to mention my master's students who worked very hard under my supervision and from who I always got significant data: Eva Prötzl, Andreas Carr, Patrick Strasser, Ece Eralp, Luca Herrmann, Birgit Prinker and Julia Manseicher. Thank you for showing interest in my research, and I apologise for the hard work.

AGRADECIMIENTOS

Finalmente, este proceso llega a su fin, y no puedo cerrar este capítulo sin agradecer a las personas que me dieron su apoyo moral durante estos seis años. En primer lugar, y siendo lo más importante en mi vida, quiero agradecer a mis padres Luis Osorio y Ana Barrios por su constante apoyo. Con cada llamada, con cada abrazo en los esporádicos viajes a Chile y con cada te amo, incluso en la ausencia terrenal, llenaron el estanque para que llegara a la meta. También, quiero agradecer a mis hermanas Claudia y Alejandra Osorio por cuidar a mis padres en mi ausencia y por hacerse cargo de la tragedia en los momentos más duros de nuestras vidas. Su fuerza y trabajo dignifican la historia familiar y son un ejemplo para mí. También mencionar a mis sobrinas, que llenaron mi corazón de cariño en todas mis visitas a la patria: Emilia y Ailin Peñas y Sofía Mendoza, quienes son un eterno fuego que calienta el alma.

También quiero agradecer a mis amigos por darme atención y cariño y no olvidarse de mi a la distancia. Entre ellos a Juan Carlos Cuminao y su familia por recibirme en el desierto cada vez que lo desee. Además, agradecer a Ariel Campos por no ser rencoroso por mis largos silencios y por su disponibilidad en mis viajes a Chile, tanto como para jugar tenis en horario laboral como para estar hombro con hombro en la desgracia. También quiero agradecer las constantes conversaciones, stickers y memes que comparto con mis amigos Sebastián Álvarez, Mauricio Toledo, Hernaldo Muñoz y Miguel Salas, a los cuales puedo recurrir cada vez que el silencio se vuelve muy ruidoso. Muchas gracias por haber estado en la oscuridad y en la luz. También dentro de esta sección, quiero agradecer a mi hermano de otros padres Maximiliano Rojas por su constante cariño y apoyo, por haber sido una gran compañía en la alegría y un soporte en la tristeza. A su vez, muchas gracias a Max por haber cruzado el atlántico cuando la soledad me asfixiaba y por haber compartido mi viaje por Alemania y la cotidianeidad bávara.

A mis amigos en la ciencia, quiero agradecer a la Dra. Dafne Franz, mi gran amiga y familia en el extranjero por estar siempre disponible para hablar conmigo. Compartir la cotidianeidad con ella es un placer, no solo por el cariño que recibo, sino que también por los buenos consejos y experiencias de vida. Muchas gracias por recibirme en Londres en tantas ocasiones y junto con el Dr. David Villarroel hacerme sentir en casa. También en Londres, quiero agradecer a mi buen amigo, el Dr. Ernesto López por su fiel e *inconstante* amistad, por sus esporádicas conversaciones, y su honesto respeto y aprecio hacia mi persona. Muchas gracias también por venir a verme al principio y al final de esta aventura, lo aprecio y atesoro mucho. No muy lejos de Londres, quiero agradecer al Dr. Erick Armingol por su amistad, que pese al silencio mutuo hemos logrado mantener hasta este punto. Muchas gracias por ser la perfecta compañía en Nueva York. Ya en Santiago, quiero agradecer a la Dra. Carolina Prado y a la Dra. Daniela Elgueta por siempre hacer un espacio en su agenda en cada visita a Chile, abrirme las puertas de su casa, darme cariño y por haber estado ahí cuando más las necesité. Tengo la más alta apreciación de ellas, ya que éstas científicas y su trabajo duro fueron mi primer ejemplo en la sacrificada vida de investigación. Estoy muy orgulloso de mantenerlas en mi vida y espero que siempre sea así.

Al final, pero no menos importante, sino que, todo lo contrario, quiero agradecer a la Dra. Filipa Kaymakanova. Si tuviera que enumerar todas las cosas por la que estoy agradecido de ella, esta tesis tendría varias páginas más. Pero mencionaré lo más importante: muchas gracias por hacer mi vida mejor y por haberme ayudado a terminar esta tesis. Me siento muy afortunado de haber encontrado a tan increíble mujer y poder compartir mi vida con ella.

SUMMARY

Activated B-cells undergo a differentiation process in distinct secondary lymphoid structures termed germinal centres (GC) to become antibody-producing cells. Although the transcriptional networks guiding GCB-cell differentiation are well studied, the regulation at the translation level still needs to be better understood. Therefore, a proteome-wide analysis was performed to identify RNA binding proteins (RBPs) with high protein levels in GCB-cells, as this diverse protein family influences mRNA stability, localisation, and translation. Among the identified RBPs with high levels in GCB-cells was Staufen 2 (Stau2), a double-stranded RBP classically studied in a neuronal context. The RBP Stau2 mainly participates in the post-transcriptional regulation of neuronal genes either by localising the encoding transcripts or through an mRNA decay process where Stau1, a paralog of Stau2, is also involved. However, despite its specific expression in GC B-cells, potential roles for Stau2 in the immune system have yet to be thoroughly investigated.

Mice containing knockout(s) for Stau2 and Stau1 (specifically) in B-cells were generated during this thesis, and the roles of both paralogs were studied in the B lineage, especially in GCB-cells at steady state and upon immunisation with a T-cell-dependent antigen. The results collected indicate that the Staufen paralogs are not required the spontaneous differentiation of GCB-cells, which occurs normally in healthy individuals. However, I determined that the presence of Stau1 is required for the optimal expansion of GCB-cells and optimal antigen-specific IgG1 responses upon immunisation. Additional loss of Stau2 in B cells somewhat mitigated the reduced antigen-specific IgG1 responses observed in Stau1-deficient mice, pointing to a possible complex interplay between the two paralogs.

To investigate the functions of the Staufen paralogs at a molecular level, I identified and exploited a suitable cell line model. Twelve different cell lines were analysed at a transcriptional level, and the A20 cell line was found to be the most appropriate model to study GCB-cells since it recapitulates the expression of key signature genes. Therefore, I investigated the function of the Staufen paralogs through knockout and epitope-tagging of the endogenous genes by employing RNA sequencing, mass spectrometry-based proteomics, as well as interaction proteomics and UV-C crosslinking immunoprecipitation to directly interrogate Staufen-RNA interactions. Overall, these approaches revealed that Stau1 slightly regulates the proteome of A20 cells, while the deficiency of Stau2 generates more considerable transcriptomic and proteomic changes. Specifically, I found that the Staufen paralogs promote the expression of relevant GC-related proteins, including Bcl6 and AID, and other potentially relevant targets, such as Usp9x, Bach2, Neil1 and E2A. These results from the A20 cell line warrant detailed further functional and mechanistic validation and further investigation in primary cells.

ZUSAMMENFASSUNG

Auf dem Weg zu einer Antikörper-produzierenden Zelle durchlaufen aktivierte B-Zellen Differenzierungsprozesse in sekundären lymphoiden Strukturen, besonders in den sogenannten Keimzentren (GC). Die Transkriptionsfaktor-Netzwerke, welche die GCB-Zell Differenzierung steuern sind weitgehend bekannt, dagegen ist die Regulation auf der Ebene der Translation weniger gut untersucht. Daher wurde eine proteomweite Analyse durchgeführt, um RNA-bindende Proteine (RBPs) mit hoher Proteinexpression in GCB-Zellen zu identifizieren, da RBPs die Stabilität, Lokalisierung und Translation von mRNA regulieren. Diese Analyse identifizierte Staufen 2 (Stau2), ein RBP das bisher hauptsächlich in einem neuronalen Kontext untersucht wurde. Stau2 ist hauptsächlich an der post-transkriptionellen Regulation neuronaler Gene beteiligt, entweder durch Lokalisierung der kodierenden Transkripte oder durch regulierten mRNA-Abbau, an dem auch Stau1, ein Paralog von Stau2, beteiligt ist. Die mögliche Rolle von Stau2 im Immunsystem wurde jedoch trotz seiner spezifischen Expression in GCB-Zellen noch nicht gründlich untersucht.

Im Rahmen dieser Arbeit wurden Mäuse mit Knockout(s) für Stau2 und Stau1 (spezifisch) in B-Zellen erzeugt, und die Rolle beider Paraloge in der B-Linie, insbesondere in GCB-Zellen im Dauerzustand und nach Immunisierung mit einem T-Zell-abhängigen Antigen, wurde untersucht. Die gesammelten Ergebnisse deuten darauf hin, dass die Staufen-Paraloge für die spontane Differenzierung von GCB-Zellen, die bei gesunden Personen normalerweise stattfindet, nicht erforderlich sind. Ich habe jedoch festgestellt, dass das Vorhandensein von Stau1 für die optimale Expansion von GCB-Zellen und eine optimale antigenspezifische IgG1-Antwort bei Immunisierung erforderlich ist. Ein zusätzlicher Verlust von Stau2 in B-Zellen milderte die bei Stau1-defizienten Mäusen beobachteten reduzierten antigenspezifischen IgG1-Antworten etwas ab, was auf ein mögliches komplexes Zusammenspiel zwischen den beiden Paralogen hindeutet.

Um die Funktionen der Staufen-Paraloge auf molekularer Ebene zu untersuchen, habe ich ein geeignetes B-Zelllinienmodell identifiziert. Zwölf verschiedene B-Zelllinien wurden auf Transkriptionsebene analysiert, und die A20-Zelllinie erwies sich als am besten geeignetes

Modell für die Untersuchung von GCB-Zellen, da die A20-Zelllinie die Expression wichtiger GCB Signaturgene aufweist. Daher untersuchte ich die Funktion der Staufen-Paraloge durch Knockout und Epitop-Markierung der endogenen Gene anhand von RNA-Sequenzierung, Massenspektrometrie-basierter Proteomik sowie Interaktionsproteomik und UV-C-Crosslinking-Immunopräzipitation um Staufen-RNA-Interaktionen direkt zu untersuchen. Insgesamt zeigten diese Experimente, dass Stau1 das Proteom von A20-Zellen leicht reguliert, während der Stau2 Knockout weitgehende Veränderungen auf der RNA als auch der Proteinebene bewirkt. Ich identifizierte diverse neue Ziel mRNA Kandidaten für die Staufen-Paraloge, unter ihnen Bcl6 und AID, die essenziellen Rollen in GCB-Zellen spielen sowie weitere potenziell relevante Ziele, unter anderen Usp9x, Bach2 und Neil1. Diese Ergebnisse aus der A20-Zelllinie erfordern detaillierte weitere funktionelle und mechanistische Validierung sowie weiterführende Untersuchungen in Primärzellen.

LIST OF PUBLICATIONS

Authorships
"The Staufen paralogs are dispensable for immune cell development, but regulate antigen-specific germinal centre B cell responses and antibody production". **Francisco Osorio-Barrios**, Yuanyuan Chu, Christian Luber, Matthias Mann, Anne-Marie Marzesco, Katarzyna Jopek, Claudia Mugler, Gönül Seyhan, Laura Kraus, Maria Robles, Markus Moser and Marc Schmidt-Supprian. *In preparation*.

Co-authorships
"Cathepsin S Alterations Induce a Tumor-Promoting Immune Microenvironment in Follicular Lymphoma". Deepak Bararia, Johannes A. Hildebrand, Sebastian Stolz, Sarah Haebe, Stefan Alig, Christopher P. Trevisani, **Francisco Osorio-Barrios**, Michael D. Bartoschek, Michael Mentz, Alessandro Pastore, Erik Gaitzsch, Michael Heide, Vindi Jurinovic, Katharina Rautter, Jay Gunawardana, Muhammed B. Sabdia, Monika Szczepanowski, Julia Richter, Wolfram Klapper, Abner Louissaint, Jr., Christina Ludwig, Sebastian Bultmann, Heinrich Leonhardt, Sebastian Eustermann, Karl-Peter Hopfner, Wolfgang Hiddemann, Michael von Bergwelt-Baildon, Christian Steidl, Robert Kridel, Joshua W.D. Tobin, Maher K. Gandhi, David M. Weinstock, Marc Schmidt-Supprian, Menyhárt B. Sárosi, Martina Rudelius, Verena Passerini, Josef Mautner, and Oliver Weigert. **Cell Reports 31, 107522, May 5, 2020.**

"A hyperreactive B cell-induced T cell checkpoint regulates autoimmunity and lymphomagenesis". Carina Diehl, Valeria Rosa Lucia Soberón, Seren Baygün, Yuanyuan Chu, Laura Kraus, Thomas Engleitner, Martina Rudelius, Christoph Daniel, Sabrina Bortoluzzi, Sabine Helmrath, Pankaj Singroul, Vanessa Gölling, **Francisco Osorio-Barrios**, Gönül Seyhan, Lena Oßwald, Rupert Öllinger, Mohsen Honarpisheh, Maciej Lech, Ul Ain Qurrat, Joachim Pircher, Vanna Imširović, Vedrana Jelenčić, Felix Wensveen, Verena Passerini, Stefanie Bärthel, Dieter Saur, Katja Steiger, Roland Rad, Oliver Weigert & Marc Schmidt-Supprian. Accepted for publication.

International conferences

- **EMBO RNA localization and local translation workshop**, Catalunya, Spain. 17-21 July 2022. Poster Author.
- **ABC7: Autoimmunity, B-cells and Complement**. Tallinn, Estonia. 14-16 June 2023. Poster Author. Second place best poster award.
- **2nd IFReC-ImmunoSensation International School on Advanced Immunology**. Maria-Laach/ Bonn, Germany. 17-22 September 2023. Poster Author.

National conferences

- **DGfI B-cell Forum 2023**. Meschede, Germany. 27-29 March 2023. Poster Author.

TABLE OF CONTENTS

LIST OF ABBREVIATIONS

Abbreviation	long term
"-/-"	Knockout
"+"	Wildtype
"+/-"	Heterozygous
"Cre/+"'	Cre-recombinase knock-in
"fl or F"'	LoxP-flanked allele
"Tg"	Transgene
ACK	Ammonium-Chloride-Potassium
ACN	Acetonitrile
AGC	Automatic gain control
AID	Activation induced deaminase
APC	Antibody producing cell
BCR	B-cell receptor
BM	Bone marrow
bp	base-pair
BSA	Bovine serum albumin
CAA	2-chloracetamide
CDS	coding determining sequence
CGG	Chicken gamma globulin
crRNA	Spacers CRISPR RNA
CSR	Class-switch recombination
dC	Deoxycytidine
DC	Dendritic cells
DDR	DNA damage response
DEG	Differentially expressed gene
DEP	Differentially expressed protein
DIA	Data independent acquisition
DKO	Double knock out
DPBS	Dulbecco's phosphate-buffered saline
dsRNA	double-stranded RNA
DZ	Dark zone
EJC	Exon junction complex
ELISA	Enzyme-linked immunosorbent assay
FA	Formic acid
FACS	Fluoresce-activated cell sorting
FBS	Fetal bovine serum
FDC	Follicular dendritic cell
FoB	Follicular B-cell
FSC-A	Forward scatter-area
FSC-H	Forward scatter-height
FSC-W	Forward scatter-width
GC	Germinal center
GCB	Germinal center B-cell
HDD	Homology donor DNA
hDEP	Highly differentially expressed protein
HDR	Homologous-directed recombination
HRP	Horseradish peroxidase
i.p.	Intra-peritoneal
ICE	Inference of CRISPR Edits
Ig	Immunoglobulin

IP	Immunoprecipitation
irCLIP	infra-red UV-crosslinked IP
KO	knockout
LC-MS/MS	Liquid chromatography coupled mass spectrometry
LN	Lymph node
LZ	Light zone
MACS	Magnetic-activated cell sorting
MFI	Median fluorescent intensity
MHC	Major histocompatibility complex
miRNA	micro RNA
mLN	mesenteric lymph node
MZB	Marginal zone B-cell
NES	Normalised enriched score
Neu5Ac	N-acetylneuraminic acid
Neu5Gc	N-glycolylneuraminic acid
NIP	4-hydroxy-3-iodo-5-nitrophenylacetic acid
NMD	non-sense mediated decay
NP	4-Hydroxy-3-nitrophenylacetyl
nt	nucleotide
nTreg	natural regulatory T-cell
ON	overnight
ORF	Open reading frame
PC	plasma cell
PCA	principal component analysis
PCR	Polymerase chain reaction
PenStrep	Penicillin-streptomycin
PerC	Peritoneal Cavity
PNA	Peanut agglutinin
PP	Peyer's patches
PTGR	Post-transcriptional gene regulation
qRT-PCR	quantitative real-time PCR
RBD	RNA-binding domain
RBP	RNA-binding protein
RISC	RNA-induced silencing complex
RNAseq	RNA sequencing
RNP	Ribonucleoprotein
scd	Single-cell derived
sgRNA	Single-guide RNA
SHM	somatic hypermutation
SMD	Staufen-mediated decay
SSC-A	Sideward scatter-area
SSC-H	Sideward scatter-height
SSC-W	Sideward scatter-width
Stau	Staufen protein
TCR	T cell receptor
T_{FH}	T follicular helper cell
TKO	Triple knockout
TMB	3,3',5,5'-tetramethylbenzidine
tracrRNA	Tracer RNA
TSO	Template switch oligo
UMI	Unique molecular identifiers
UTR	Untranslated region
WT	Wildtype

LIST OF FIGURES AND TABLES

INTRODUCTION

Immune System

The immune system protects the organism against external threats, including viruses and bacteria and internal malignancies like cancer, by orchestrating the function of several cell types. The immune response and its comprised cells are grouped into two branches: the innate immune response, which clears the danger fast without generating memory, and the adaptive immune response, which prevents recurrent events of the same threats by memory generation.

Adaptive immune response

Cells originated in the thymus and are called T-lymphocytes, and the cells differentiated from lymphoid precursors in the bone marrow, called B-lymphocytes, mainly mediate the adaptive immune response. Mature lymphocytes populate secondary lymphoid organs, including the spleen and lymphoid organs, where they sense the circulating antigens from the blood and lymph, respectively. Also, in these organs, innate antigen-presenting cells give all the required signals to activate T and B-lymphocytes, thereby initiating the adaptive response. Adaptive immune responses culminate with the effector cells migrating to the site where the action of the immune system was triggered and antibody-producing cells secreting antibodies against the threat to the bloodstream.

T-cell development

Common lymphoid progenitors from the bone marrow or fetal liver populate the thymus and rapidly expand depending on available IL-7. Later, the precursors committed to the T-cell lineage up-regulate the genes that mediate the T-cell receptor (TCR) assembly, which ultimately, after an antigen-independent differentiation process, culminates as a functional complex comprised γ and δ, or α and β chains. The Tαβ cells transit from a pre-T to a double-positive T cell, expressing CD4 and CD8.

Double-positive T cells recognising self-antigen-loaded major histocompatibility complex (MHC) with low avidity are positively selected in the thymus epithelium, while those that fail to bind to MCH die, a process termed death by neglect. On the contrary, clones that recognise self-antigen/MHC with high avidity are negatively selected in the thymus medulla. Double-positive thymocytes that pass both positive and negative selection convert into mature $CD8^+$ or $CD4^+$ single-positive T-cells by interaction with MHC class I or II during the differentiation process, respectively.

B-cell development

Hemopoietic stem cells residing in the bone marrow give rise to B-cells. In this tissue, B-cells develop through several stages regulated by numerous transcription factors, including PU.1, EBF, IRF8 and Pax5, among others, ending with lymphocytes carrying a B-cell receptor (BCR) or immunoglobulin (Ig) with antigen specificity. When exiting the bone marrow, B-cells complete their development to the mature or naïve state, which can be identified by the

presence of IgD in the plasmatic membrane together with IgM. The Ig consists of a heavy and a light chain assembled from different segments. Heavy chains consist of the V_H, D, J_H and C_H segments, which can generate nine different heavy chain types: IgM, IgD, IgG_{1-4}, IgA_{1-2}, and IgE. Light chains are constituted by the V_L, J_L, and C_L segments, and they can constitute two types: κ and λ [1].

B-cell subsets

Early in the ontogeny, fetal liver-derived B1 B-cells populate different tissues, including the peritoneal cavity, where they are the primary B-cell type. B1 B-cells, identified in mice by the expression of CD19 but low B220, generally do not undergo somatic hypermutation (SHM) and secrete polyspecific IgM upon differentiation into plasma cells. On the other hand, B2 or conventional B-cells (hereafter named just B-cells) are $CD19^+$ $B220^+$, and after activation, they secrete specific antibodies. Due to the critical role of B-cells in antibody secretion and systemic immunity, I focused this thesis mainly on this cell type, particularly in their differentiation process.

Germinal Centre B-cells and high-affinity humoral response

To become high-affinity antibody-producing cells comprising plasma cells (PC) and plasmablast, activated B-cells, after diversifying the immunoglobulins to other heavy chains in a process called class switch recombination (CSR)[2], undergo affinity maturation in distinct secondary lymphoid structures called germinal centres (GCs). From a classical point of view, in the GCs, there is a cyclic, structural and functional separation in the differentiation process of the B-cells. In the dark zone (DZ) of the GCs, B-cells undergo massive proliferation, expanding related cognate cells. At the same time, their encoding BCR segments acquire mutations during SHM depending on the activation-induced cytidine deaminase (AID) enzyme. In the light zone (LZ) of the GCs, the resulting affinity of the mutated BCR is tested in the presence of the antigen. The cells that recognise the antigens are positively selected by the limiting survival signals in the LZ and then clonally expanded in the DZ before exiting the GCs as PC or memory cells. B-cells that poorly recognise the antigen return to the DZ to perform SHM before re-entering into the LZ or dying [3], as summarised in Figure 1.

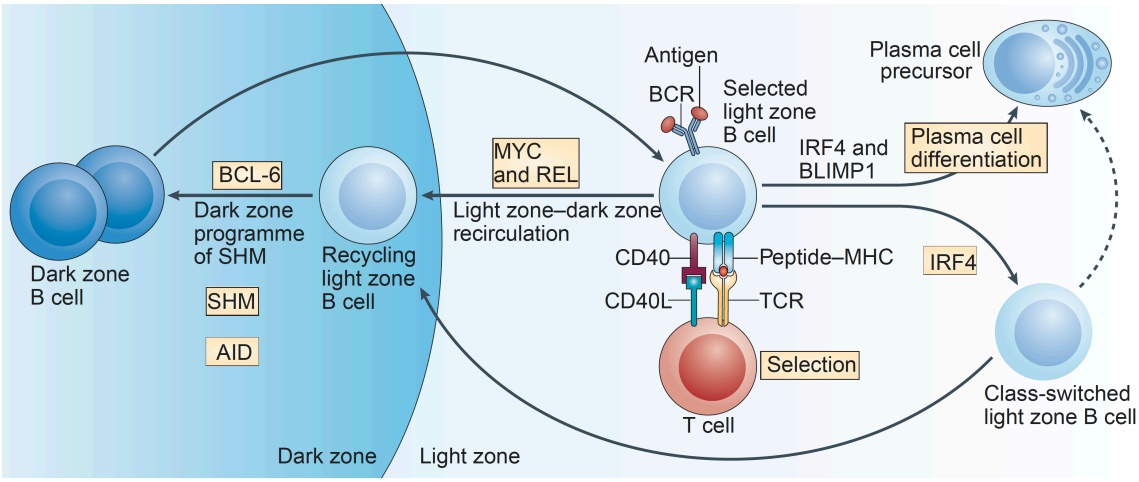

Figure 1: Germinal centre B-cells and their function compartmentalisation. Activated B-cells by up-regulating key transcriptional factors transit from the dark and light zones, where they undergo different processes to generate plasma cells. Figure modified from [4].

The molecular networks involved in the GC reactions rely on gene expression programs orchestrated by the timing of different transcription factor expression and activity. Early activated B-cells up-regulate MYC and IRF4 shortly, initiating the GC reaction by upregulating BCL6, the master regulator of the GC B-cells (GCBs). The transcriptional repressor BCL6 retains B-cells in the GC by increasing the tolerance to DNA damage produced in the SHM and CSR, controlling apoptosis, and suppressing the cell cycle arrest and the expression of the PC-related transcription factor BLIMP1. After positive selection in LZ, a second wave of MYC and IRF4 expression depending on NFκB allows B-cell re-entry to DZ for clonal expansion and later exit of the GC-program downregulating Bcl6 [5].

Considering the timing of the expression of antagonist transcription factors in the GCBs, studying post-transcriptional regulation is crucial for understanding their expression and its diverse mechanisms. While transcription lays the foundation for RNA synthesis, post-transcriptional processes control RNA fate, including RNA splicing, modification, localisation, and degradation, as summarised in Figure 2.

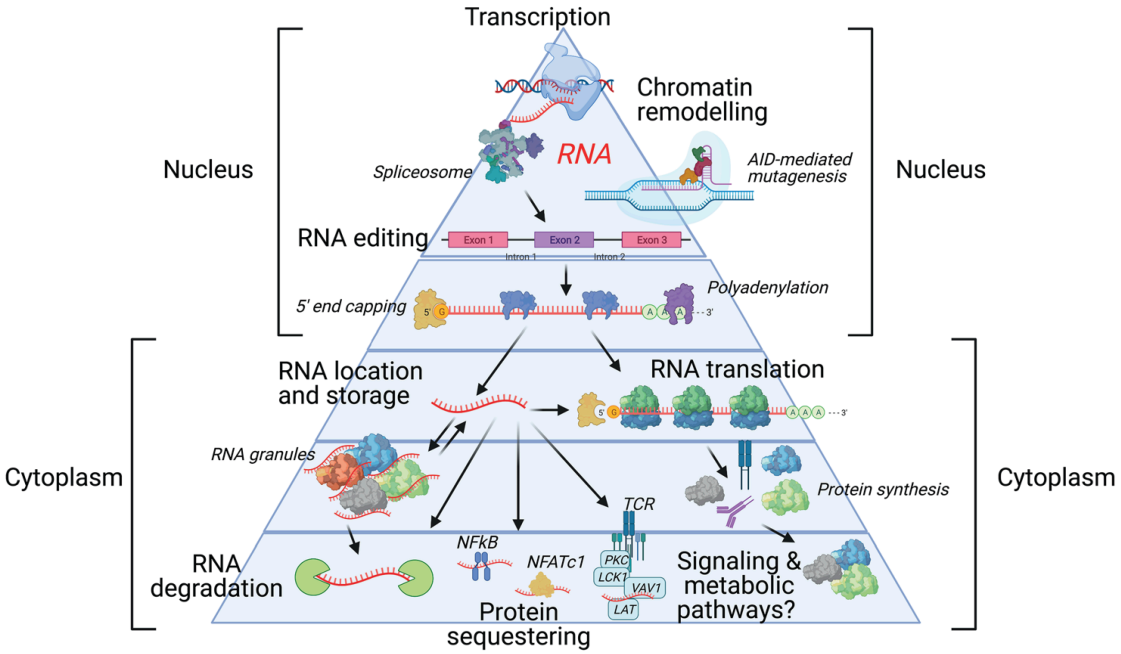

Figure 2: Post-transcriptional regulation levels. Pyramid drawing showing the potential fate of RNA from transcription to degradation. Scheme obtained from [6].

These regulatory steps play pivotal roles in fine-tuning gene expression and influencing protein abundance, localisation, and functionality [7]. Thus, by deciphering the intricacies of post-transcriptional regulation in GCB cells, our understanding of the differentiation process will increase, offering potential insights for therapeutic interventions and precision medicine approaches to treat, for instance, infections with an inefficient B-cell response, including Malaria, Dengue and HIV [8, 9].

Post-transcriptional Regulation of Germinal Centre B-cells

Post-transcriptional regulation emerges as a critical process to tightly regulate the intricate molecular network ruling the biology of lymphocytes, as reviewed in [6]. In GCB cells, one mechanism is based on controlling the abundance of mRNA of genes with critical functions during B-cell differentiation. In this regard, the small non-coding RNAs called microRNAs (miRNA) have been well studied in GCB cells [10]. These molecules participate in silencing target genes, mediating their mRNA degradation by complementary sequences in the 3' untranslated region (UTR) in a DICER-dependent fashion. Mice lacking DICER expression in

AID-expressing cells severely impair GC-formation in naïve and immunised mice and, consequently, a reduced antibody response [11]. GC-specific microRNAs, which might explain that phenotype, include the miR-17 family members miR-17-5p and miR-106a [12], which may promote the cell cycle progression from G1 to S regulating the expression of the cyclin CDKN1A [13].

On the other hand, miR-28 regulates proliferation in the GC, interfering with the ERK1/2 signal transduction and the antiapoptotic capacity of MYC [14]. However, proliferation is not the only feature regulated by miRNAs since miRNA-155 regulates the expression of AID, SHM, and CSR, avoiding mutations outside the Ig locus and an early exit of the GC of low-affinity B-cells [15]. Similarly, miR-127 retains the cells in the GCs by targeting the *Prdm1* mRNA, limiting the expression of BLIMP1 [16]. On the other hand, the differentiation and survival of PCs are promoted by the miR-148a, which targets antiapoptotic genes and Bach2 [17], another transcription factor essential for GC formation and maintenance [18, 19].

Despite the relevant role of DICER/miRNAs in the biology of GCB cells, more than controlling the abundance of critical mRNAs is required to understand the molecular processes undergoing the GC reactions, as was suggested by *Tan et al*. to describe the poor correlation between RNA and proteins in activated T-cells [20]. In GCB cells, for instance, the Bcl6 encoding mRNA is already present in naïve B-cells, but it is not until B cells reach the GC stage that the protein is identified [21]. Similarly, the E3-ubiquitin ligases Cbl and Cbl-b are transcribed in naïve B-cells, but they are expressed only in LZ GCB cells where they control the expression of IRF4 and, as a consequence, the maintenance of the cells in the GCs, avoiding an early exit as PC [22]. Thus, the timing in the mRNA translation, given its availability to the translation machinery or its localisation, also seems relevant in the GCB cells to explain the discrepancy between proteins and their encoded mRNAs.

RNA binding proteins in germinal centre B-cells

All the processes related to the maturation, stability, localisation, translation and modification of the RNA are also regulated by diverse and conserved protein families called RNA binding proteins (RBPs). Classically, an RBP binds an RNA in target sequences and motifs by a well-defined RNA binding domain (RBD) [23]. The interaction of given RBPs with their target RNA conforms ribonucleoprotein (RNP) complexes, which can interact with others in a liquid-liquid phase separation to establish membrane-less granules, where other member proteins might bind RNA without having a canonical RBD [24].

The RBPs have recently started to be studied in the GCBs. In addition to the previously mentioned DICER, which regulates the abundance of RNA, other RBPs, including the methyl-transferase like 14 (Metl14) and their functional partner YTHDF2, both related to the modification of the RNA, promote the GC differentiation and, as a consequence, the humoral response upon immunisation [25, 26]. Similarly, the mRNA stabiliser HuR (encoded by *Elavl1*), expressed in all B-cells with a peak in GC B-cells, regulates their differentiation and the resulting humoral response upon immunisation [27]. Moreover, PTPB1, which controls the alternative splicing and polyadenylation, promotes GC differentiation, the transition between LZ and DZ, and the humoral response [28]. Likewise, Tia1/Tial1 promote the differentiation and survival of GCBs upon immunisation and their respective antibody response [29]. The latter is also promoted by the RBPs hnRNPLL and hnRNP F [30, 31].

Nevertheless, considering the relevance of the RBPs in GC biology, a systematic and unbiased proteome-wide study identifying the abundance of RBPs in vivo could identify candidate RBPs controlling critical regulatory pathways in the differentiation of B-cells.

Preliminary RBPome in primary GCBs

To quantify protein expression in GCB cells compared to surrounding mantle zone B-cells, previously to this doctoral Thesis, wild-type (WT) mice were immunised with OVA/LPS in Alum adjuvant, and 10 days later, the GCB cells and mantle zone B-cells were purified by magnetic separation (MACS) followed by fluorescence-activated cell sorting (FACS). The whole proteome of the cell populations was determined by label-free quantitative mass spectrometry and is shown in Figure 3.

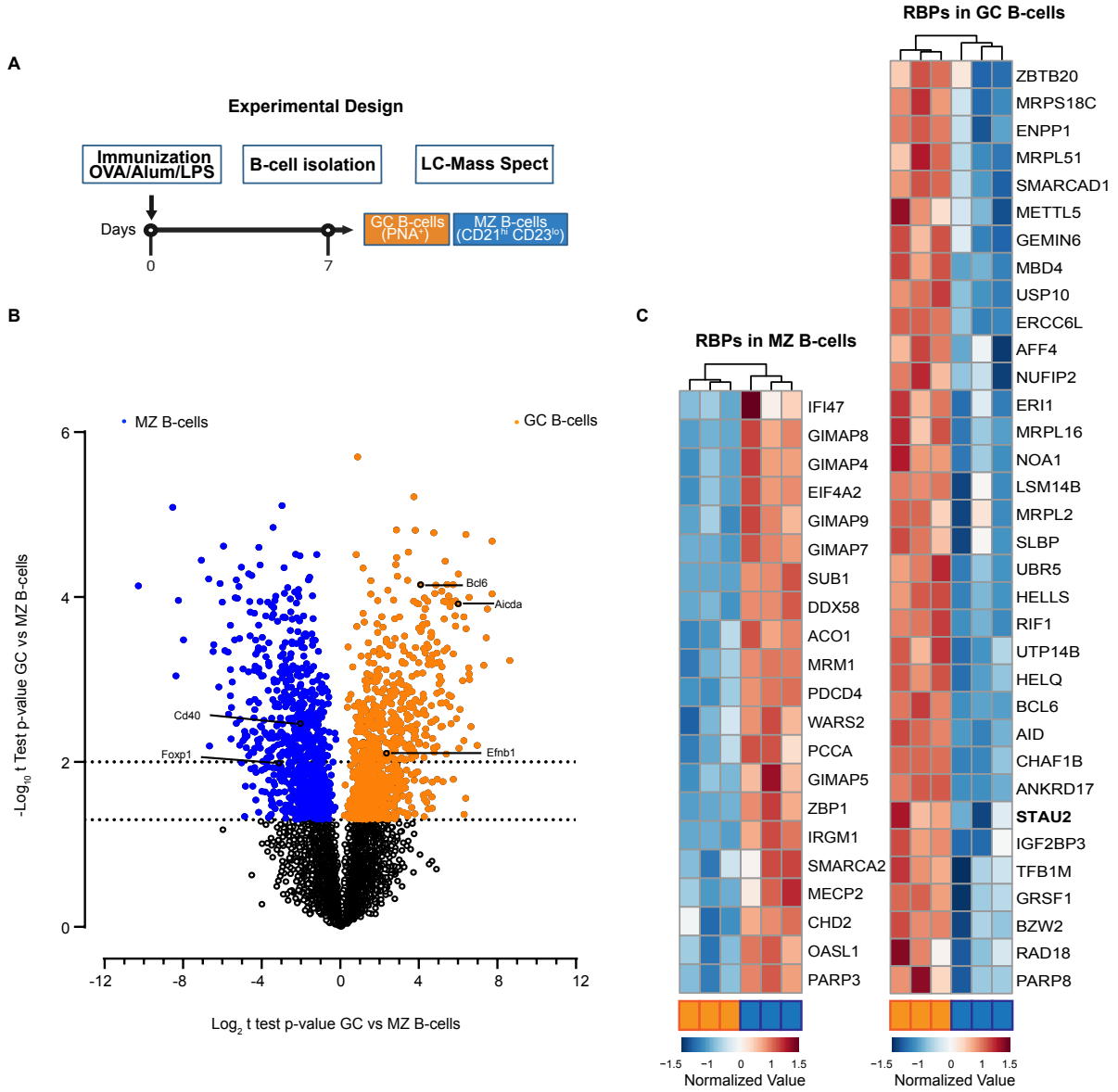

Figure 3: The RBP Stau2 is differentially expressed in GCBs. **A**. Experimental Design Scheme. **B**. Differentially expressed proteins (*p*-value<0,05 dotted line at y=1,3 and *p*-value <0,01 dotted line y=2) for GCB (orange) and mantle zone (Blue) B cells are shown in a volcano plot. **C**. RBPs enriched >5-fold in the mantle zone B (left) and in GCB (right) cells are shown for each replicate.

The differentially expressed genes between GCBs and mantle zone B cells, coloured in the volcano plot (Figure 3B), showed 847 proteins statistically up-regulated in the mantle zone B cells (in blue) and 892 proteins up-regulated in GCB cells (in orange), where the classical GCB cell-markers are highlighted.

To determine the RBP proteins with differential abundance between these two populations, previously reported canonical RBPs [16], classified as such for bearing structural domains able or reported to bind RNA, were cross-referenced with all the differentially expressed proteins (1739 proteins with a *p*-value<0,05) finding that 262 of them belong to this family. Among those RBPs, 73% (192 out of 262) are up-regulated in the GCBs, while only 27% are preferentially expressed in mantle zone B cells. To focus on the most enriched RBPs in each cell type, I identified those with a |Fold Change| > 5, finding 21 proteins for mantle zone B cells and 34 for GCB cells (Figure 1C). Among the RBPs enriched in mantle zone B cells, I detected the translational repressor PDCD4, which was also recently reported to increase in this B-cell population, restricting the immune response to a T-cell-independent antigen [17]. On the other hand, among the RBPs enriched in GCB cells, I observed the Myc expression potentiator IGF2BP3, which was previously reported as a GC B-cell-related protein [18, 19]. In addition, ENPP1 and ZBTB20 were observed, which are up-regulated in GCB cells compared to naïve B-cells and are important for long-lived PC generation [20, 21]. Besides, the proteins related to class switch recombination, a pivotal process to diversify the humoral immune response, MBD4 [22], HELLS [23], RIF1 [24], and the extensively described AID were also found enriched in the analysis. Similarly, the GC master regulator BCL6, included in the RBP category due to its C2H2 and C2H2-type zinc fingers, was also identified as highly up-regulated in GCB cells.

The in-depth studied GC-regulating RBPs HuR (Log2FC=0.24), PTBP1 (Log2FC=0.32) and Tial1 (Log2FC=0.37) showed a statistically not significant higher expression in GCB cells, while Dicer1 (Log2FC=-0,32), hnRNPLL (Log2FC=-0,68) and hnRNP F (Log2FC=-0,63) show a trend for higher expression in mantle zone B-cells.

To study the RBPs up-regulated in GCB cells and their specificity within the immune system, I analysed their mRNA expression pattern across several cell types using Skyline from Immgen [25], as observed in Figure 4.

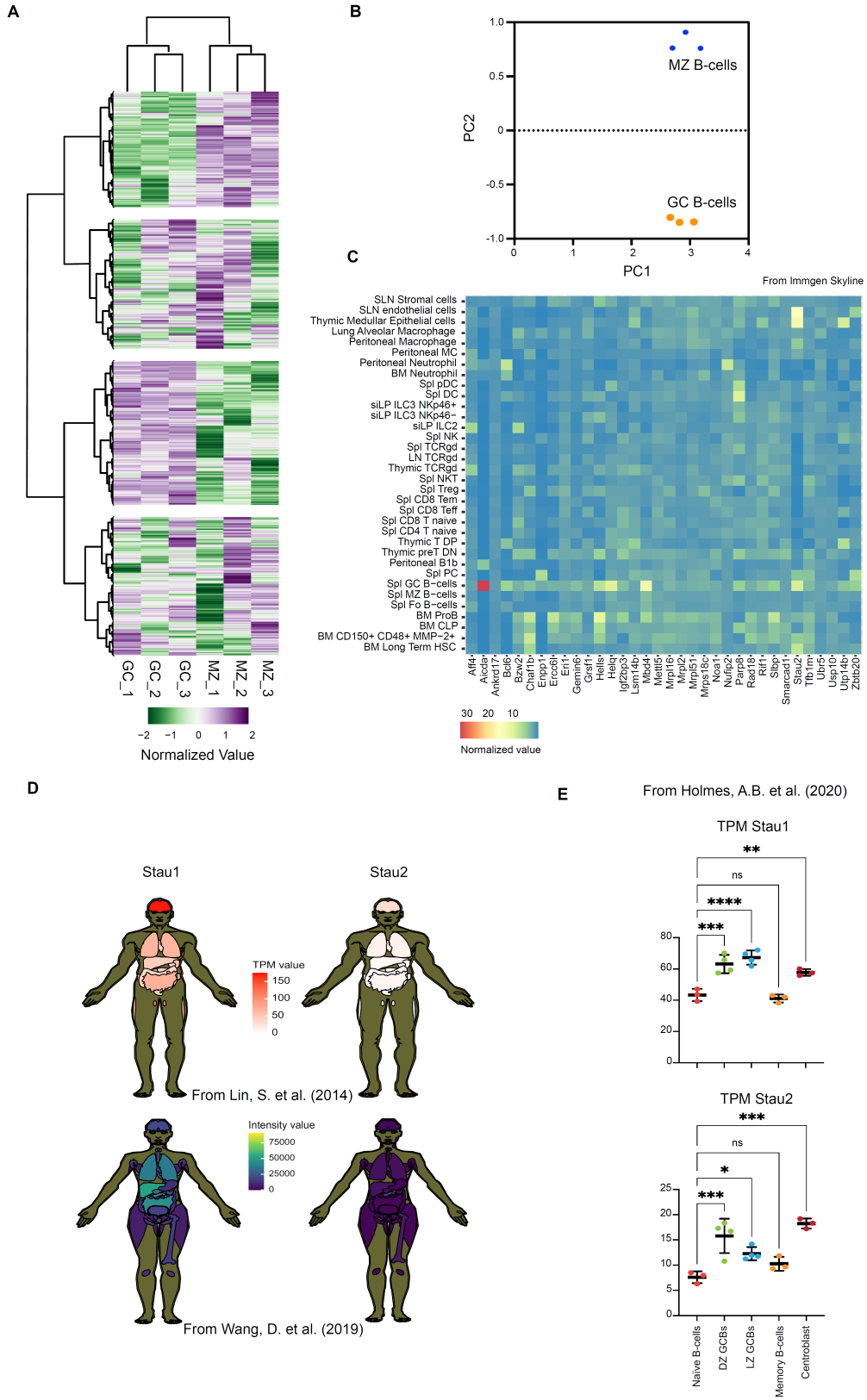

Figure 4: Stau2 is distinctly expressed in GCB cells. **A**. Heat plot showing normalised LFQ value by protein among the different samples. **B**. PCA plot of the proteome LFQs values of GCB cells and MZBs is shown. **C**. Heat plot showing normalised TPM value by gene transcription and populations in immune populations for all the relevant RBPs in the GCB cells.

D. TPM value (RNA; top) obtained from [32] and intensity value (protein; bottom) obtained from [33] of Stau1 (left) and Stau2 (right) in human tissues. **E**. Mean ± SD of the TPM value for Stau1 (top) and Stau2 (bottom) in different human B-cell populations obtained from [34] is shown where * represents *p*-value<0.05, ** *p*-value<0.01 and ****p*-value<0.001.

As expected, AID (Aicda) is the highest enriched RBP in GCB cells, as observed in Figure 4C. However, it is not restricted to that population since it is also transcribed in peritoneal B1 B-cells. Similarly, Bcl6 mRNA, besides being highly transcribed in GCB cells, is also elevated in neutrophils and thymic double-positive T-cells. Likewise, the already mentioned Enpp1, Hells, Helq and Mbd4 are preferentially transcribed in the GCB cells, but their respective mRNAs are also present in other immune populations. Interestingly, the RBP Staufen 2 (Stau2), almost exclusively transcribed in GCB cells and PC, has yet to be studied in these immune populations. Thus, we decided to explore the potential functions of this RBP in B-cells.

Neuronal functions of Staufen proteins

Staufen (Stau) is an RBP that was primarily described in Drosophila, where it regulates the patterning in the expression of *Oskar*, *Prospero* and *bicoid* mRNAs (among others), which are critical for the early embryo and neuronal development [35]. Stau recognises double-stranded features in the RNA using dsRNA-binding domains (dsRBD), which consist of two α-helices flanking three-strand antiparallel β-sheets [36]. Two different Stau orthologues, Stau1 and Stau2, have been identified across vertebrate species by sequence homology, and they are present in several splice variants [37-40].

Stau1 is present in most tissues (Figure 4D), whereas Stau2 is mainly expressed in the brain and heart [41]. Although both homologs are expressed in neurons, neuromuscular junctions and oligodendrocytes, they contribute to different RNP complexes in distinct parts of the somatodendritic compartment [41-44]. Stau1 and Stau2-containing RNPs share just a fraction of their respective mRNA targets [45], and there were no functional compensatory effects by Stau1 in the absence of Stau2 reported [46]. In addition, mice expressing a truncated Stau1 do not show perturbation in Stau2 expression [47]. Altogether, the current literature suggests overlapping but non-redundant functions between the paralogs.

High throughput transcriptional analysis on Stau1-downregulated cells showed a similar number of upregulated and downregulated genes [48], which, in addition to the interaction of Stau1 with the components related to the nonsense-mediated mRNA decay (NMD) [49-51],

suggest a homeostatic mRNA surveillance role for this paralog, which is called Staufen-mediated mRNA decay (SMD) [52]. Despite Stau2 being involved in SMD [44], its downregulation in neurons mainly resulted in the downregulation of gene expression [45], indicating an mRNA stabilisation role.

The subcellular localisation of Staufen 2

After translation, Stau2 folding and early transport in the cytoplasm could be mediated by the chaperon Hsc70 since the proteins interact in the absence of ATP [53, 54]. Then, unbound Stau2 can shuttle from the cytoplasm to the nucleus due to two nuclear localisation sequences, one in the link between dsRBD3-dsRBD4 and the other within the dsRBD4 [55, 56]. Stau2 probably binds RNA inside the nucleus in the nucleoplasm or nucleoli [52]. Then, RNA-bound Stau2 can interact with p62 or other proteins to generate Stau2-containing RNP complexes in an RNA-dependent or -independent manner [57, 58]. Conspicuously, Stau2 binds intronic regions even on its mRNA [59], suggesting that Stau2-RNPs inside the nucleus could be related to the splicing of pre-mRNA. However, there are opposing reports on Stau2 as an interactor of Y14 and Magoh, two prominent members of the exon junction complex (EJC)[60]. One report showed the interaction between Stau2 and Y14/Magoh by immunoprecipitation (IP) experiments in mature rat cortical neurons [57]. In contrast, another article detected no interaction between the EJC members and Stau2 using IP followed by liquid chromatography-mass spectrometry in the E17 rat brain lysates [53], hinting at development-specific functions.

Different mechanisms can be used for Stau2 to shuttle from the nucleus. Stau2^{62}-containing granules can be exported out of the nucleus through Exportin5 [55] in a way potentiated by the zinc-finger protein ZFR [61], whereas Stau2^{59}, and possibly Stau2^{52}, containing complexes can be exported either by using CRM1 (Exportin1) through a nuclear export signal in its N-terminus or, a mechanism depending of interactors that can target the dsRBD3 [56]. Stau2^{56} RNPs, in contrast, could also use the protein Tap, which has been involved in the export of RNA and co-localize and co-IP with p62-Stau2 complexes in the nucleus [57, 62].

In the cytoplasm, mRNAs associated with RNP complexes are often considered translationally dormant because RNP granules lack tRNAs and other factors required to initiate translation [63]. In agreement with this notion, Stau2-containing granules present the nuclear-cap-binding protein 80 (CBP80), the Poly(A)-binding protein (PABP) and the PABP nuclear 1 (PABPN1) but no translation factors [58]. Therefore, it seems likely that Stau2 controls the spatiotemporal

regulation of the translation of their bound mRNAs, moving the cargos through the cell using the cytoskeleton towards spots where PABP and PABPN1 can be removed, and CBP80 can be replaced by eIF4E to initiate the translation. In particular, the Stau2 C-terminus can interact with the Kinesin heavy chain, generating the displacement of Stau2-containing complexes in a microtubule-based movement, which mitogen-activated protein kinase (MAPK) enhances [64]. More detailed, in the region dsRBD3-4, Stau2 harbours two docking sites for extracellular signal-regulated kinase (ERK) 1/2, and ERK2 is critical for speeding up the movement of the Stau2-containing granules to the dendrites in neurons [65].

Mechanisms of Stau2 to regulate translation of its target mRNAs

Stau2 interact with the helicase Upf1 [51, 58, 66] and participates in SMD [51] where either mRNAs with a premature stop codon are degraded or misplaced-intronic mRNAs translation is aborted or stalled. In this regard, it has been observed that Stau2 can pause the translation in the soma of neurons, generating stalled polysomes through Upf1 interaction. Stalled polysomes are transported to the synaptic dendrites, where the translation can be reanimated upon metabotropic glutamate receptor activation, which is also highly relevant for long-term depression [67, 68]. In addition to Upf1, Stau2 may control the translation of the targeted mRNAs using the RNA-induced silencing complex (RISC) since it can interact with the helicase Mov10, the Dicer-related dsRBP PACT and both Ago2 and its RNA-duplex-loading chaperon Hsc70 [54, 58, 69]. However, Stau2 can also potentiate the translation of target mRNAs in an Upf1-dependent manner, as observed in GFP or luciferase-tethered experiments [66].

Features in mRNAs targeted by Staufen

Performing IP of tagged or endogenous Stau2 protein, using mono or polyclonal antibodies in mammal samples, followed by microarrays or next-generation sequencing analysis, have identified targets related to signal transduction, cellular chemical hemostasis, cellular ion homeostasis and, to a lesser extent to metabolic-related processes. To identify common characteristics in Stau mRNA targets, the mean length of 5'UTR, open reading frame (ORF) and 3'UTR of Stau-regulated mRNAs were compared by *Laver et al.* [70]. This analysis shows consistently that 3'UTR length is a significant feature, being nearly three to four times larger in the mRNA targets than in the non-targets. The mean length 3'UTR of the mRNAs targets of a co-expressed single-stranded RBP was also determined as a control using available data, showing it also binds long 3'UTRs; however, the length of the Stau2-targeted 3'UTR was

higher. Reliably, using the data from *Furic et al.* [45], it was determined by *Laver and colleagues* that the mean length of 3'UTR is also a significant feature in a human context, being ~ four times larger in the Stau2 targets than in the non-targets.

Moreover, a focused determination was carried out by *Heraud-Farlow et al.* [71] in a subgroup of 38 Stau2-mRNAs targets susceptible to the Stau2 downregulation: the median length of 3'UTR was determined to be 2,4-fold larger in the subset than the whole rat 3'UTRome. However, mRNA with short 3'UTR (i.e. ~100 bp) and mRNAs lacking 3'UTR sequence can also be bound and transported by Stau2 [72, 73], proposing that other mRNA regions could be relevant for Stau2 binding.

One decade ago, a pioneering method called individual-nucleotide resolution Cross-Linking and Immune-Precipitation (iCLIP) was developed to study the role of hnRNP C in pre-mRNA processing by determining its binding sites to RNA [74]. This study demonstrated that iCLIP is a powerful tool for studying RBPs-RNA interactions, and it sparked the development of diverse derivative methods [75]. Performing iCLIP in an E18 mouse brain, it was determined that Stau2 mainly binds RNA structures present in introns, 3'UTR, intergenic regions and, to a lesser extent, coding sequences (CDS) and 5'UTRs [59]. Surprisingly, the binding of Stau2 to intronic areas is not only related to the maturation of the RNA since it has been reported that Stau2 mobilises intron-retained mRNAs into the dendritic compartment in hippocampal neurons for a later expression [59, 76]. On the other hand, using RNA-hybrid and iCLIP (hiCLIP), which serves to identify mRNA duplex structures, it was determined that Stau1 binds structures mainly present in rRNA, tRNA and 3'UTR and, to a lesser extent, CDS, introns and extended non-coding RNAs [77]. Functionally, the duplexes recognised by Stau1 in CDS are associated with translational repression, whereas the duplexes present in 3'UTR are associated with enhanced translation [77].

Studies investigating the Stau2 protein and its mRNA targets have revealed significant insights into its binding preferences and functional implications. Analyses utilising various techniques such as immunoprecipitation, microarrays, sequencing, and iCLIP have shown that Stau2 predominantly targets mRNAs with long 3'UTRs, suggesting a role in post-transcriptional regulation. However, exceptions exist, with evidence of Stau2 binding to mRNAs with short or lacking 3'UTRs. Additionally, Stau2 exhibits a diverse binding pattern across different RNA regions, including introns, 3'UTRs, intergenic regions, and coding sequences, implying multifaceted functions beyond canonical mRNA processing. These findings underscore the complexity of Stau2-RNA interactions and shed light on its diverse regulatory roles in cellular processes.

Stau2 and the cell cycle

Stau2 is expressed in all cell cycle stages [73] and might play a different role in each gap. During the S/G2 transition, DNA repair typically occurs, where Stau2 may have a function since it targets many transcripts related to the DNA damage response (DDR) [45]. Moreover, it was reported that the transcription of *Stau2* is downstream of the kinase ATR and the intermediate CHEK1, both highly related to the DDR [78]. More specifically, ATR/CHEK1 promotes the activity of the transcription factor E2F1 in the steady state. Thus, the Stau2 transcription is bound to the cis-element `putative E2F1 transcription factor binding site´ within the Stau2 promotor [78]. However, after a replication stress outbreak, E2F1 is displaced from the *Stau2* promotor, leading to its downregulation and, speculatively, decreasing the chances of the cells to respond to DDR, originating apoptosis [78].

Stau2 also targets mRNA-encoding proteins related to spindle formation, chromosome alignment and cytokinesis during cell division [79]. Besides, Stau2 is phosphorylated at TBD-dsRBD5-like region by Cdk1 [80], advocating a role in mitosis and proliferation, which is strongly supported by the literature. Previously, downregulation of Stau2 ex vivo in neuronal precursors was shown to dampen its proliferation [81]. Similarly, silencing of Stau2 in retinal precursors has decreased proliferation in both ex vivo and in vivo [82]. Similarly, primordial germ cells of *Zebrafish* expressing a negative-dominant inhibitor of Stau2 failed to generate clusters *in vivo* [37]. Consistently, in DF1 cell lines, the silencing of Stau2 showed a decrease in BrdU uptake. In contrast, the ectopic expression of Stau2 in HEK293 cells increased proliferation, as indicated by the enhanced BrdU uptake [82]. Despite that, the mechanism of Stau2 to regulate the proliferation in progenitor cells and cell lines is unlikely the same.

Very recently, the role of Stau2 in myeloid leukaemia was described, giving new insights into the relevance of this protein in cell proliferation. In *Bajaj et al.* [83], it was identified that Stau2 expression is downstream of the chromosome-translocation generated oncogenes BCR-ABL and NUP98-HOXA9, being enhanced by around fourfold in cells with both mutations. Moreover, performing enhanced CLIP in the K562 blast crisis chronic myeloid leukaemia cell line, it was determined that Stau2 promote the expression of chromatin remodelers like KDM1A, Maz, Noc2l and others, promoting epigenetic changes and, ultimately, proliferation. The last correlated with leukaemia stem cells or cell lines with a Stau2 deficiency showed reduced *in vitro* and *in vivo* expansion.

Lymphocytes undergo massive proliferation in their undifferentiated state and upon activation when mature. Stau2 was highly up-regulated in GCBs, which might contribute to B-cell proliferation. However, the role of Stau2 in the precursor cells should also be considered.

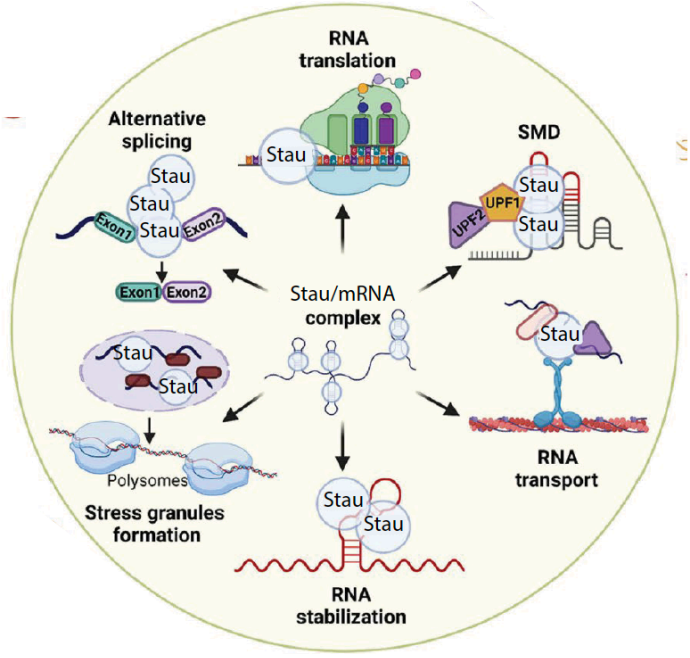

Figure 5: Different role of the Staufen paralogs in cell biology. The diagram was modified from [84], indicating all the roles Stau paralogs play in the post-transcriptional regulation.

Staufen paralogs in the immune system

Baseline murine RNAseq data obtained from Expression Atlas (https://www.ebi.ac.uk/gxa) [85] using the experiment E-MTAB-3079 indicate that $Kit^{+}Sca1^{+}$ hematopoietic stem cells, E15 liver hematopoietic stem and common lymphoid and myeloid progenitors express *Stau2* mRNA. In agreement with that, protein Stau2 was detected in hematopoietic stem and progenitor cells, granulocytic precursors and mesenchymal/stromal cells from human bone marrow samples [86]. Strikingly, Stau2 (KO) knockout mice showed less cellularity in femur bone marrow cells than the WT counterpart [83], suggesting a role of this protein in that compartment. Moreover, Stau2 transcript and protein have been detected in bone marrow, lymph nodes and spleen in the omics analysis [32, 33]. Notwithstanding all comments above, the expression of Stau2 in all tissues is lower than Stau1, as is shown in Figure 4. Thus, the expression of both paralogs must be considered in a deep study of the role of these RBPs in the immune system.

HYPOTHESIS AND AIMS

Rationale

In their differentiation process into high-affinity antibody-producer cells, germinal centre B-cells undergo an intricate transcriptional landscape mediated by the action of antagonist transcriptional factors. As a significant player in post-transcriptional regulation, the RNA binding proteins might regulate the transcriptional changes by regulating the expression of critical molecular mediators. After performing unbiased genome-wide proteomic analysis in germinal centre B-cells, the RBP Staufen 2, classically associated with the transport of relevant transcript to the neuronal dendrites and with unknown function in B-cells, was observed to be highly up-regulated and specifically expressed in this cell population. Considering that Staufen 2 promote mitosis and participate in the DNA damage control:

Hypothesis

"Staufen 2 plays a role in the germinal centre B-cells differentiation."

Aims:

1.- To determine whether the absence of Staufen 2 affects the spontaneous germinal centre B-cells in the periphery.
2.- To determine possible compensatory effects of Staufen 1 in the absence of Staufen 2 in B-cells.
3.- To study the role of the Staufen paralogs in the immune response against a T-cell-dependent antigen.
4.- To propose the possible pathways that Staufen paralogs might be involved in B-cells.

MATERIALS AND METHODS

Mice

B-cells Stau2 knockout mice: the promotor-driven “knockout-first” reporter tagged allele [87], called Tm1a, in the neighbourhood of the exon 4, which encodes the majority of dsRBD1 and its link with dsRBD2, in the Stau2 locus (C57BL/6N-A$^{tm1BrdStautm1a(EUCOMM)Wtsi/WtsiH}$) were generated by the Wellcome Trust Sanger Institute Mouse Genetics Project. Adult mice with one Tm1a allele were obtained from the European Mouse Mutant Archive partner MRC Harwell Institute and then crossed with mice expressing an optimised Flp recombinase [88] (B6N(B6J)-$^{Tg(CAG-Flpo)1Afst}$; MGI: 4453967) to obtain the LoxP-flanked exon 4 allele (Tm1c) in the offspring.

Stau1 knockout mice (C57BL/6-Stau1$^{tm1MSS/N}$; termed as Stau1$^{-/-}$) were generated *in-house* by electroporation of embryos with sgRNA/Cas9 RNPs targeting simultaneously the coding exon 1 (crRNA: ACCTACAGCTATGGCATGCG) and 10 (crRNA: CACAGCCGCCTCTCGTCAGT). Embryos with the desired ~14kb deletion (checked by PCR) were then implanted in pseudo-pregnant females. Later, the offspring were crossed with *wild-type* (WT) mice to determine the individuals with the mutation in the germline. The resulting heterozygous mice (Stau1$^{+/-}$) were backcrossed, showing the Mendelian ratio in the progeny. Later, Stau1$^{+/-}$ littermates were crossed to obtain either Stau1$^{+/-}$, Stau1$^{-/-}$ and WT mice. Stau1$^{-/-}$ mice were also crossed with Stau2$^{-/-}$ mice to generate Stau double knockout (Stau1$^{-/-}$/2$^{-/-}$) viable, fertile animals without any obvious abnormality.

All the breeding strategies to generate the desired mouse lines and the subsequent analysis or experiments on target genotypes complied with the regulations dictated by the Regierung of Oberbayern. The Centre for Preclinical Research at the Faculty of Medicine of the Technical University of Munich housed all the above-described mouse lines under specific pathogen-free conditions. There, mice were fed *ad libitum* and kept in individually ventilated cages with a 12h/12h dark/light cycle.

Primers and PCR genotyping strategy

The genotype of all mice was determined by PCR using 1-2μL of DNA from ear punches obtained with Proteinase K-supplemented DirectPCR®-Ear (Viagen Biotech, CA, USA) as input. Depending on the reaction, either GoTaq® (Promega, WI, USA), DreamTaq (Thermo Fisher Scientific, MA, USA) or homebrew Taq DNA polymerase were used. As primers, 100 μM HPLC-purified oligonucleotides were ordered from Eurofins Genomics (Luxemburg) and used to a final concentration of 0,34-0,5 μM in a 20-30μL final reaction. The sequence of the different line-related primers is shown in Table I.

Table I: Sequence and product sizes of all the genotyping PCR performed

Line	Allele	Primer	Sequence	Product
Stau2	WT Tm1a	5'arm_WTF	GAAATGTCCGTGGACTCAGC	WT: 470 nt Tm1a: 112 nt
		5'mut_R1	GAACTTCGGAATAGGAACTTCG	
		Crit_WTR	CAGGTACCAAACCTGGTGGT	
	Tm1c Tm1d	5'Cas_F1	AAGGCGCATAACGATACCAC	Tm1c: 575 nt Tm1d: 180 nt
		Crit_WTR	CAGGTACCAAACCTGGTGGT	
		3'LoxP	ACTGATGGCGAGCTCAGACC	
Stau1	WT KO	Stau1_1b_F	TGGCTGTTAGCATCAGTGTC	WT: 460 nt KO: 300 nt
		Stau1_10b_R	GTTAGTGGCCTCAGAAAGAGG	
		Stau1_10b_F	GTCTGGGATGAGAATGGCTTAT	
Mb1	WT hCre_Tg	hCre_F	ACCTCTGATGAAGTCAGGAAGAAC	Mb1 WT: 400 nt hCre: 500 nt
		hCre_R	GGAGATGTCCTTCACTCTGATTCT	
		Mb1_F	CTGCGGGTAGAAGGGGGTC	
		Mb1_R	CCTTGCGAGGTCAGGGAGCC	
VavP_Bcl2	hBcl2_Tg	VavBcl2_F	ACGGTGGTGGAGGAGCTCTTC	500 nt
		VavBcl2_R	AAAACCTCCCACACCTCCCCCTGAA	
FLPO	FlpO_Tg	FLPo_F	GCCACCTTCATGAGCTACAACACC	400 nt
		FLPo_R	AACAGGAACTGGTACAGGGTCTTGG	

Cell lines

Several murine B-cell lines were collected from different sources. Balb/c B-cell lymphoma A20 [89] and plasmacytoma MPC-11 [90] were kindly donated by Prof. Dr Ralph Mocijak (Helmholtz Zentrum München). Balb/c plasmacytoma J588L [91] and modified J558L expressing IgM able to recognise 4-hydroxy-3-iodo-5-nitrophenylacetic acid (NIP) were kindly donated by Prof. Dr Michael Reth (University of Freiburg). Lymphoma C57BL/6 lines $B220^+$ IgM^+ with constitutive expression of c-MYC driven by Eμ promotor, named Emu449, Emu483 and Emu 665, were generated and donated by Prof. Dr Gisela Keller (Technical University of Munich). Similarly, C57BL/6 lines expressing c-MYC under Cγ1 locus isolated from tumours infiltrating the spleen (165 Spl) and Peyer's patches (19 PP) were generated and donated by Dra. Sandrine Sander (Deutsches Krebsforschungszentrum). A pre-B-cell line knockout for RAG2, SLP65 and Igλ5 (triple knockout; TKO) [92] was generated and contributed by Prof. Dr Hassan Jumaa (Universitäts Uniklinikum Ulm). *In-house*, B-cells B1 lymphomas C57BL/6 lines TR28 and TR50 were isolated from tumours with constitutive expression of IκB Kinase 2 (IKK2ca).

A20 cells were cultured in 10% heat-inactivated 0,22 μm-filtered fetal bovine serum (FBS; Merck, Darmstadt, Germany) Glutamax-supplemented RPMI 1640 media (Gibco™, Thermo Fisher Scientific) in the presence of 2-mercaptoethanol (50 μM; Gibco™), HEPES (25 mM; Gibco™) and Penicillin-Streptomycin (Pen/strep; 1X; Gibco™). MPC-11 cells were cultured in 10% heat-inactivated 0,1-μm filtered horse serum (Kraeber & Co, Ellerbek, Germany) Glutamax-supplemented DMEM (Gibco™) in the presence of Pen/Strep (1X). J558L were cultured in 10%-FBS Glutamax-supplemented RPMI 1640 in the presence of 2-mercaptoethanol (50 μM) and Pen/Strep 1X. J558L cells expressing IgM to recognise NIP (J558L-NIP) were cultured similarly to J558L but adding mycophenolic acid (1 μg/mL; Merck), xanthine (1,2 mM; Merck) and Hypoxanthine (110 μM; Merck). Eμ lines were cultured in 10%-FBS Glutamax-supplemented RPMI 1640 in the presence of non-essential amino acids (NEEA, 1X, Gibco™), 2-mercaptoethanol (5 μM) and Pen/Strep (1X). 165Spl, 19PP, TR28 and TR50 lines were cultured in 10%-FBS Glutamax-supplemented RPMI 1640 in the presence of HEPES (10 mM), NEAA (1X), sodium pyruvate (1X; Gibco™), 2-mercaptoethanol (50 μM) and Pen/strep (1X). TKO cells were cultured in 1% heat-inactivated 0,22 μm-filtered premium fetal calf serum (FCS; Pan-Biotech, Bayern, Germany) Glutamax-supplemented IMDM (Gibco™) in the presence of 2-mercaptoethanol (50 μM), Pen/Strep (1X) and recombinant murine IL-7 (10 ng/mL; Peprotech, Thermo Fisher Scientific).

Cell lines were stored at -80ºC or -160ºC in 10%DMSO/FBS. After thawing, cells were seeded at $2x10^5$ cells/mL and passages were made twice to thrice a week. On every occasion, the concentration of cells and viability were checked using a Countess™ 2 automated cell counter (Invitrogen™), ensuring the maintenance of >90% viability. When not reached, apoptotic cells were cleared using the Dead Cell Removal Kit (Miltenyi Biotec, Bergisch Gladbach, Germany) following the manufacturer´s guidelines. The cells were incubated typically at 37ºC 5% CO_2, except for TKO cells cultured at 7,5% CO_2.

Antibodies

For the detection of Stau paralogs by western blot, rabbit IgG monoclonal anti-STAU1 [clone EPR7966; 1/2000] was purchased from Abcam (Cambridge, United Kingdom), rabbit IgG polyclonal anti-STAU2 [Batch H7; 1/2000] was kindly donated by Prof. Dr Michael Kiebler (Ludwig-Maximilian-Universität Munich) and mouse monoclonal IgG1 anti-GAPDH [clone 6C5: 1/10000] was acquired from Merck and used as loading control. For the detection of 3xFLAG-tagged proteins, the mouse monoclonal M2 antibody [1/2000] was purchased from Merck.

Monoclonal antibodies for flow cytometry were purchased from BD Bioscience (Franklin Lakes, NJ, USA), BioLegend (San Diego, CA, USA), eBioscience (Thermo Fisher Scientific), Jackson Immunoresearch (Ely, Cambridgeshire, UK) or Miltenyi Biotec. The antibodies were coupled to biotin or fluorophores excitable at different laser wavelengths; for 355 [nm] laser, Brilliant Ultra Violet® (BUV) 395, BUV661 and BUV 737 were used. For 405 [nm] laser: Brilliant Violet® (BV) 421, eFluor® (eF) 450, VioBlue®, BV510, BV605, BV650, BV711 and SuperBright® (SB) 780 were used. For the 488 [nm] laser: fluorescein isothiocyanate (FITC), Alexa Fluor® (AF) 488, Peridin-Chlorophyll-protein (PerCP), and PerCP-Cyanine (Cy) 5.5 were used. For the 561 [nm] laser, Phycoerythrin (PE), PE/Dazzle594®, PEvio615, PerCPeF710, PE/Cy7 and PEvio770 were used. For 638 [nm] laser AF700, Allophycocyanin (APC), APC/Cy7, and APCeF780 were used. Streptavidin was conjugated either to BUV395 or APCeF780 to detect biotin. The clones, fluorophores, and concentrations used to detect all target antigens are specified in Table II.

Table II: Antibodies clone and concentration for the detection of all targets antigens

Antigen	Clone	Isotype	Fluorophore	Dilution	Brand	Order-Nr
Bcl6	K112-91	Mouse / IgG1, kappa	PE/Cy7	400	BD Biosciences	563582
CD11b (Mac-1)	M1/70	Rat / IgG2b, kappa	Bv510	200	BioLegend	101263
CD11c	N418	Armenian hamster / IgG	PE/Cy7	500	eBioscience	25-0114-82
CD127	A7R34	Rat / IgG2a, kappa	PE	200	eBioscience	12-1271-82
CD138	281-2	Rat / IgG2a, kappa	Bv421	100	BioLegend	142523
	281-2	Rat / IgG2a, kappa	APC	50	BD Biosciences	561705
CD170 (SiglecF)	E50-2440	Rat / IgG2a, kappa	PE	200	BD Biosciences	552126
CD184 (CXCR4)	2B11	Rat / IgG2b, kappa	PE	200	eBioscience	12-9991-82
CD184 (CXCR4)	2B11	Rat / IgG2b, kappa	PerCPeF710	50	eBioscience	46-9991-82
CD185 (CXCR5)	L138D7	Rat / IgG2b, kappa	biotin	100	BioLegend	145510
CD19	6D5	Rat / IgG2a, kappa	Bv510	200	BioLegend	115546
	eBio1D3	Rat / IgG2a, kappa	APCeF780	300	eBioscience	47-0193-82
	eBio1D3	Rat / IgG2a, kappa	AF700	200	eBioscience	56-0193-82
CD1d	1B1	Rat / IgG2b, kappa	PerCP/Cy5.5	400	BioLegend	123514
CD21/CD35	7G6	Rat / IgG2b, kappa	FITC	200	BD Biosciences	553818
CD23	B3B4	Rat / IgG2a, kappa	AF700	400	BioLegend	101632
CD24	M1/69	Rat / IgG2b, kappa	APCeF780	1600	eBioscience	47-0242-82
CD249 (BP-1)	REA988	Human IgG1	APC	300	Miltenyi Biotec	130-116-701
CD25	PC6.1	Rat / IgG1, lambda	FITC	50	BioLegend	102006
CD273 (PD-L2)	TY25	Rat / IgG2a, kappa	BUV661	100	BD Biosciences	741674
	TY25	Rat / IgG2a, kappa	BUV737	100	eBioscience	741889
CD279 (PD-1)	J43	Armenian hamster / IgG	PE	800	eBioscience	12-9985-82
CD317 (PDCA-1)	927	Rat / IgG2b, kappa	Bv711	200	BD Biosciences	747604
CD38	90	Rat / IgG2a, kappa	APC/Cy7	400	BioLegend	102712
CD4	RM4-4	Rat / IgG2b, kappa	Bv711	1600	BD Biosciences	740651
CD43	REA840	Human IgG1	VioBlue	300	Miltenyi Biotec	130-112-891
CD44	IM7	Rat / IgG2b, kappa	PerCP/Cy5.5	1000	BioLegend	103032
CD45R (B220)	RA3-6B2	Rat / IgG2a, kappa	FITC	200	eBioscience	11-0452-82
	RA3-6B2	Rat / IgG2a, kappa	Bv650	300	eBioscience	416-0452-82

	RA3-6B2	Rat / IgG2a, kappa	Bv510	100	BioLegend	103248
	RA3-6B2	Rat / IgG2a, kappa	AF700	200	BD Biosciences	557957
CD5	53-7.3	Rat / IgG2a, kappa	eF450	1500	eBioscience	48-0051-82
CD62L	MEL-14	Rat / IgG2a, kappa	Bv650	200	BD Biosciences	564108
	MEL-14	Rat / IgG2a, kappa	Bv510	400	BioLegend	104441
CD69	H1.2F3	Armenian hamster / IgG	Bv650	100	BioLegend	104541
CD80	REA983	Human IgG1	PEvio615	50	Miltenyi Biotec	130-116-467
CD83	Michel-17	Rat / IgG1, kappa	Bv650	50	BioLegend	121515
CD86	GL-1	Rat / IgG2a, kappa	APC	200	eBioscience	17-0862-82
	GL-1	Rat / IgG2a, kappa	Bv650	50	BD Biosciences	564200
CD8α	53-6.7	Rat / IgG2a, kappa	Bv605	100	BioLegend	100744
CD93 (AA4.1)	AA4.1	Rat / IgG2b, kappa	APC	100	eBioscience	17-5892-82
CD95	Jo2	Armenian Hamster / IgG2, λ2	PE	200	BD Biosciences	554258
	Jo2	Armenian Hamster / IgG2, λ2	Bv421	800	BD Biosciences	562633
	Jo2	Armenian Hamster / IgG2, λ2	Bv605	50	BD Biosciences	740367
c-Rel	REA397	Human IgG1	APC	100	Miltenyi Biotec	130-106-138
F4/80	BM8	Rat / IgG2a, kappa	AF488	100	BioLegend	123120
FoxP3	FJK-16s	Rat / IgG2a, kappa	PE	50	eBioscience	12-5773-82
	FJK-16s	Rat / IgG2a, kappa	APC	50	eBioscience	17-5773-82
GL-7	GL-7	Rat / IgM	eF450	200	eBioscience	48-5902-82
Gr-1	RB6-8C5	Rat / IgG2b, kappa	APCeF780	400	eBioscience	47-5931-82
ICOS	C398.A4	Armenian Hamster IgG	Bv421	1000	BioLegend	313524
Ig λ1	R11-153	Rat / IgG1, kappa	Biotin	100	BD Biosciences	553431
IgA	11-44-2	Rat / IgG1, kappa	PE	100	eBioscience	12-5994-81
IgD	REA772	Human IgG1	PEvio770	300	Miltenyi Biotec	130-111-498
	11-26c.2a	Rat / IgG2a, kappa	PerCP	300	BioLegend	405710
	11-26c (11-26)	Rat / IgG2a, kappa	FITC	200	eBioscience	11-5993-82
	11-26c.2a	Rat / IgG2a, kappa	PE/Dazzle594	100	BioLegend	405742
IgG1	A85-1	Rat / IgG1, kappa	FITC	200	BD Biosciences	553443
IgG2a	R19-15	Rat / IgG1, kappa	BV605	100	BD Biosciences	564024
IgG2b	R12-3	Rat / IgG2a, kappa	BUV737	100	BD Biosciences	749137
IgG3	R40-82	Rat / IgG2a, kappa	BV421	400	BD Biosciences	565808

IgM	Polyclonal	Goat / F(ab')2	PerCP	100	Jackson ImmunoResearch	115-126-075
	II/41	Rat / IgG2a, kappa	PE/Cy7	800	eBioscience	25-5790-82
	II/41	Rat / IgG2a, kappa	SB780	50	eBioscience	78-5790-82
IRF4	3E4	Rat / IgG1, kappa	PerCPeF710	800	eBioscience	46-9858-82
NK1.1	PK136	Mouse / IgG2a, kappa	APC	100	eBioscience	17-5941-82
	PK136	Mouse / IgG2a, kappa	PE/Cy7	200	eBioscience	25-5941-82
Streptavidin			APCeF780	100	eBioscience	47-4317-82
			BUV395	200	BD Biosciences	564176
TCRβ	H57-597	Armenian Hamster / IgG2, λ1	Bv605	100	BD Biosciences	562840
	H57-597	Armenian Hamster / IgG2, λ1	Bv510	100	BioLegend	109234
TCRγδ	GL-3	Armenian Hamster IgG	Bv421	100	BioLegend	118119

Western Blot

Cell pellets or animal tissue were lysed with phosphatase/protease inhibitors cocktail (1X; Halt™, Thermo Scientific) supplemented RIPA buffer (Thermo Scientific) on ice for 15 minutes with occasional gentle mixing. Later, the extractions were centrifuged at 16000g for 20 minutes at 4ºC, and the protein fraction was moved into a pre-cooled fresh 1,5 mL protein LobindTubes® (Eppendorf, Hamburg, Germany) and kept at -20ºC until used. The protein concentration was absorbance-based determined using the microplate setting of the DC™ Protein Assay kit (Bio-Rad, CA, USA) and 750 [nm]-measurement in a plate reader (Spark, Tecan Group, Männedorf, Switzerland) following the manufacturer's instructions.

Between 20-60 µg of protein were mixed 1:1 with DTT-supplemented (50 mM final concentration; Pierce™, Thermo Scientific) 2X Laemmli sample Buffer (Bio-Rad) in a 50 or 70 µL final volume. Then, the samples were heated at 90ºC for 10 minutes and ice-cooled until use. Later, half of the sample volume was loaded into a 4-12% Bis-Tris pre-cast gel (NuPage™, Invitrogen™, Thermo Scientific) with colour-stained protein standards (Precision Plus™, Bio-Rad). Gels were run for 65 min at 180 V with 0,5 L of MOPS buffer (1X; NuPage™, Invitrogen™), and later, the proteins were semi-dry transferred into a nitrocellulose membrane (Power Blotter Transfer Stacks; Invitrogen™) using the 7 minutes mixed-range voltage pre-set method of a Power Blotter (Invitrogen™) with its respective transfer stacks.

The nitrocellulose membranes were briefly washed with MilliQ water and then blocked for 1 hour with Intercept® Blocking Buffer (Li-Cor Bioscience, NE, USA) with gentle shaking. Then, the blots were incubated for 4 hours at room temperature or overnight at 4°C, with gentle shaking with the primary antibodies mixed in T20 antibody diluent Buffer (Li-Cor Bioscience). After, the membranes were three times vigorously washed with 0,2%-Tween 20 PBS for 5 minutes each time, to later being incubated with the dye-conjugated secondary antibodies Goat anti-rabbit IgG-IRDye800CW and or Donkey anti-mouse IgG IRDye680RD both [1/15000] in T20 antibody diluent during 2 or 6 hours. Finally, the blots were once more three times washed with solid shaking, and the fluorescence of the secondary antibodies was acquired using an Odyssey Scanner (Li-Cor Bioscience).

When necessary, the relative expression of the target proteins was calculated after normalising the pixel intensity of its bands with their respective loading control band in the blots, using ImageStudio Lite v5.2 (Li-Cor Bioscience).

Single-cell suspension and flow cytometry analysis

Male or female 10-20 weeks-old mice were sacrificed by isoflurane (CP Pharma, Burgdorf, Germany) inhalation for 3 minutes. Either spleen, thymus, inguinal lymph nodes (iLN), mesenteric lymph nodes (mLNs) and Peyer's patches (PPs) were collected and mechanically disaggregated in MACs Running Buffer (Miltenyi Biotec; hereafter as MACs) using frosted microscopy slides. Bone marrow (BM) was collected by cutting the bone ends from the tibia and femur and flushing out the medullar content with 1 mL of MACs *per* bone using a 3 mL syringe (Luer-Lok™ Tip, BD) coupled to a 25G x 1'' needle (Microlance™, BD).

Peritoneal cavity (PerC) cells were collected after a *lavage*; 5 mL of Glutamax-supplemented DMEM were injected with a 10 mL syringe (Injekt®, B.Braun) coupled to a 23G x 1'' needle (Eclipse™, BD) in the bottom left or right side of the mouse PerC. After, the mouse was shaken gently for 2 minutes. Then, the upper part of the cavity was cut, and all the previously injected media was recovered by pipetting.

The suspension cells from all mentioned tissues or cavities were treated with Ammonium-Chloride-Potassium (ACK: Gibco™) lysis buffer for 3 minutes. After, MACs was added to each reaction to stop the erythrolysis and cells were washed by centrifugation at 1400 rpm for 7 minutes at 4ºC. Later, the cell pellets were resuspended in MACs, 70 µm-filtered, and the cell number of a 1:1 dilution with Trypan Blue 0,4% (Gibco™) was determined using a Neubauer's

chamber. The cells were either frozen in 10%-DMSO/FBS ($2x10^7$ cells/mL) or used for immunostaining.

For flow cytometry, between 1-$5x10^6$ cells were resuspended in 100µL 1X of Dulbecco's phosphate buffered saline (DPBS: Gibco™) buffer and incubated for 15 minutes with anti-CD16/CD32 (1/200; Fc Block™, BD Bioscience) and iFluor™ 840 maleimide (1/1000; AAT Bioquest, CA, USA) to avoid later unspecific antibody binding and identify dead cells, respectively. To determine the expression of surface molecules, cells were immunostained with fluorochrome-conjugated antibodies (see Table II) for 30 minutes in 100µL of MACs at room temperature. Later, the cells were fixed with 1%-formaldehyde (ROTI®Histofix, Carl Roth, Karlsruhe, Germany) in DPBS. For intracellular antigen detection, after the surface staining, cells were resuspended in fixation/permeabilisation solution (eBioscience) and incubated for at least 30 minutes at 4ºC. Then, intracellular immunostaining was carried out in permeabilisation buffer (eBioscience) on the ice during 1-4 h or overnight at 4ºC. Data were collected with a 5-laser Cytoflex LX (Beckman Coulter, CA, USA) cytometer acquiring 50,000 events of the target population or the whole sample, and results were lastly analysed with FlowJo v10.8 software (TreeStar, Ashland, OR, USA).

Blood serum obtention

From just sacrificed mice, before any dissection, the left and after the right heart ventricle was punched with an Insulin syringe (Omnifix®, B.Braun, Hesse, Germany) coupled to a 25G x 1'' needle (Microlance™), and blood was withdrawn. Then, it was deposited into 1,3 mL serum tubes (Sarstedt, Nümbrecht, Germany), which were later centrifuged at 10,000g for 10 minutes to separate the protein fraction from the coagulated cells. The serum was then moved into a fresh 1,5 mL tube and centrifuged at 16000g for 10 minutes to separate any remaining coagulated debris. Finally, the clean serum was collected and stored at -80ºC in LobindTubes®.

From living mice, ~50µL of blood was obtained from the facial vein using a sterile steel blood lancet (Centramed®, Koblenz, Germany). Later, the blood was deposited in conventional 1,5 mL tubes, which were centrifuged as described above to obtain the protein fraction, which was ultimately stored at -80ºC in protein LobindTubes® until use.

NP immunisation

4-Hydroxy-3-nitrophenylacetyl (NP) hapten conjugated to chicken gamma globulin (CGG) was purchased in a molar ratio 30-39:1 (NP:CGG; Biosearch technologies, Hoddesdon, UK), resuspended at 1 mg/mL and storage at -20ºC. On immunisation day, NP:CGG was diluted 1:1 with Imject^{TM} Alum adjuvant (Thermo Scientific), and 100µL of the mix (50µg NP:CGG) or Alum alone were intra peritoneal injected into 12-20 weeks old mice using an Insulin syringe (Omnifix®) coupled to a 30G x 1/2'' needle (Sterican®, B.Braun). Every 7 days, alternating right and left chick, serum from blood was collected as described above. Ten or 28 days after immunisation, mice were sacrificed, and blood (serum), spleen and bone marrow were dissected as previously detailed. By the staining of $2x10^7$ splenocytes, responder B-cells to NP were identified by flow cytometry using NP conjugated to PE (1/400; Biosearch Technologies) and anti-Igλ1 (table II), as it has been reported it is the most common light chain in the NP response [93, 94].

Automated magnetic immune cell separation

Total resting untouched B-cells from spleen single-cell suspension (aka splenocytes) were obtained using the B-cell Isolation Kit (Miltenyi Biotec). Briefly, $4x10^7$ splenocytes were resuspended in 160µL of MACs. Then, the no-B-cells were automatically stained and depleted from the samples by the autoMACS Pro Separator (Miltenyi Biotec) using the auto labelling followed by the DEPLETES program. Similarly, $CD43^-$ cells from splenocytes, largely B-cells, were purified after the autoMACS stained and depleted $CD43^+$ splenocytes ($4x10^7$ cells/320 µL MACs) using CD43 microbeads (Miltenyi Biotec). The purity of B-cells ($CD19^+$ $B220^+$) was checked by flow cytometry, always reaching >90%.

Germinal Centre B Cell (PNA) MicroBead Kit (Miltenyi Biotec) enriched GCBs from purified B-cells or splenocytes. According to the manufacturer's guidelines, the cells were first incubated with peanut agglutinin (PNA) coupled to biotin and then with anti-biotin microbeads. Afterwards, the cells expressing ligands to PNA were isolated by the autoMACS Pro Separator using the sensitive POSSELDS program. The enrichment of GCBs was checked by flow cytometry ($CD19^+B220^+CD95^+CD38^-$ or $CD19^+B220^+CD95^+Bcl\text{-}6^+$).

Enzyme-linked immunosorbent assay (ELISA)

ELISA's detection of NP-specific immunoglobulins in blood sera of immunised mice was conducted similarly to what was previously described [95]. In detail, Nunc-Immuno^{TM} 96-well flat-bottom plates (Sigma-Aldrich) were coated overnight at 4ºC with 100μL of either NP_2-BSA (Biosearch technologies, rows B-H, columns 1-10) or NP_{36}-BSA (rows B-H, columns 1-10) at 5 μg/mL, and in row A with 50μL of goat anti-mouse IgG1 or IgM at 10 μg/mL in 0,1 M carbonate buffer. After the unspecific binding sites were blocked using 1% bovine serum albumin (BSA) DPBS, a standard curve was generated in the first row of every plate by loading from 10000 to 0 ng/mL of purified murine IgM or murine serum-derived IgG1 (RS10-101-5; Bethyl Laboratories), following a dilution factor of 2. In the other rows, 50μL of the blood sera of each mouse collected at different time points and sequentially diluted seven times in 1:4 ratios (starting at 1:200) were loaded (one dilution a row). Then, the samples were incubated in their respective plates for at least 1 hour.

Detection goat anti-mouse IgG1 or IgM antibodies coupled to horseradish peroxidase (HRP) were diluted at 6,67 ng/mL in 1%BSA/DPBS, and 50μL were incubated for 1h at room temperature (RT). The bound immunoglobulins were colourimetrically identified by adding 3,3',5,5'-tetramethylbenzidine (TMB) substrate (100 μL/well; BD Bioscience). Finally, the colourimetric reaction was stopped between 5 and 30 minutes after using H_3PO_4 (1 M; 50 μL/well). The absorbance of each well was determined using a plate reader at 450 [nm], and the concentration of anti-NP immunoglobulins was determined by the average of at least three interpolated dilutions absorbance within the linear range using the standard curve made in each plate.

Immunohistochemistry

50.000 to 70.000 cells were loaded into cytofunnels and centrifuged using the Shandon cytospin 2 centrifuge at 700 rpm for 3 minutes. Afterwards, cells were fixed in 4% methanol-free formaldehyde for 30 minutes at room temperature and washed twice with 1x DPBS. Samples were then incubated in a blocking buffer for at least 2 hours at room temperature. Primary antibodies were then loaded onto the sample slides and incubated overnight at 4°C, followed by washing three times in 1xDPBS and incubation with secondary antibodies and phalloidin for 2 hours at room temperature. After washing (three times with 1x DPBS), nuclear counterstaining was performed with DAPI for 10 minutes. Samples were then mounted with slide covers using a mounting medium and sealed with nail polish. The mounting medium was

allowed to solidify at room temperature before the samples were stored at 4°C in a dark environment to preserve their integrity.

In vitro testing of nuclease activity of RNPs

To determine the best sgRNA among several candidates, the Cas9/sgRNA nuclease activity was assessed *in vitro*. Several spacers CRISPR RNA (crRNA) were ordered from Integrated DNA Technologies (IDT; Iowa, USA) and coupled to a universal tracer RNA (tracrRNA). Then, 3 μM of crRNA:TracrRNA duplex was mixed with 1 μg of homebrew spCas9 and incubated for 1 hour at 37ºC with 150 ng of purified PCR product containing the target region, which was obtained using: Phusion High-Fidelity polymerase (Thermo Scientific), the primers listed in Table III and 100 ng of genomic DNA from A20 cells obtained with QIAmp DNA Micro Kit (Qiagen, Hilden, Germany) following the manufacturer's instructions.

The nuclease reaction was stopped with the sequential incubation for 15 minutes at 37ºC with RNAse A [4 μg] and 1μL of stop solution (30% glycerol, 1,2% SDS, 250 mM EDTA). Finally, the entire reaction was loaded and ran for 1 hour at 180 [V] into a 1,5%-agarose gel with its respective control (minus spCas9 or scrambled sgRNA). The chosen crRNA for the following experiments was the one which cut most, or everything, of the PCR amplicon among the candidates.

Cas9/sgRNA RNP-driven Stau1, Stau2 and Stau double knock-out A20 cells

The sequence of several sgRNAs targeting the exon 4 of Stau2 and their respective scrambles controls were obtained from the Brie [96] and Yusa [97] libraries and tested *in vitro*. Later, the two best sgRNAs were mixed with Alt-R® spCas9 v2 (IDT) following the manufacturer's guidelines to conform to RNPs. Equally amount of the two RNPs were mixed, and 1μL of that or control sgRNA/Cas9 RNP was added to $4x10^5$ A20 cells resuspended in 9μL of Buffer R (From Neon™ electroporation system; Invitrogen) one day after *cell passage*. In addition, 2μL of electroporation enhancer [10,8 μM; IDT] was added to each reaction and 10μL of the final volume was electroporated with 2 pulses of 1100 [V] during 20 [ms] using a 10μL-Neon®-pipette transfection system (Invitrogen). Two days later, cells were harvested, and single cells were seeded in wells of 96-U-well plates by limited dilution, following previously published guidelines [98]. Ten to twelve days after, single-cell-derived (scd) A20 cell clones were selected, and the genomic DNA was isolated using the blue reaction of PrepGEM universal kit (MicroGEM, Southampton, UK) following the manufacturer's protocol. From the DNA

preparation, 2µL were used to perform Phusion High-Fidelity PCR reactions generating amplicons of the genomic region targeted for each or both sgRNAs, as detailed in Table III. The PCR products were either directly loaded into a 1%-agarose gel or purified using QIAquick PCR purification Kit (Qiagen), Sanger-sequenced (Eurofins Genomics) and analysed by the web tool Inference of CRISPR Edits (ICE; Synthego, CA, USA). The clones with large deletions in the target region, produced presumably by the simultaneous cutting of both RNPs, were selected by gel amplicon size. On the other hand, clones without a notorious deletion but with a >90% probability of being Stau2 knock-out (Stau2-KO) given by ICE were then expanded and stored.

Stau1 knock-out (Stau1-KO) scd A20 clones were generated using the same sgRNAs delivered in mice embryos (*see* Mice section). Moreover, the clones were analysed using the same PCR strategy that the mice used for genotyping. The expression of STAU1 by the most promising candidates was checked by western blot, and the Stau1-KO A20 cells were then expanded and stored.

To generate deficiency of both paralogs, two Stau1-KO A20 clones were electroporated with the Brie-library-contained sgRNA/Cas9 targeting Stau2. Similarly, two Stau2-KO A20 clones were delivered with the mentioned RNP targeting exon 1 of Stau1. The knockout index of the scd clones for the second targeted paralog was analysed using ICE considering Stau1 exon 1 or Stau2 exon 4 sequences. The candidate's Stau double knock-out (Stau1/2-DKO) A20 cells were chosen based on >90% knock-out probability, expanded and storage.

Homologous directed recombination (HDR) in A20 cells

To generate A20 cells with STAU-tagged proteins, sgRNAs targeting the neighbourhood (± 18 nt) of the first encoding methionine for Stau1 and the encoding stop codon for Stau2 were tested in vitro, as detailed previously. After choosing the best possible sgRNA for each target (see Table III), 200 nt homology donor DNA (HDD) oligos considering left homology arm: 3xFlag coding sequence: right homology arm in a 1:1:1 ratio were purchased as LabReady [100µM, pH=8] from IDT. When the sgRNAs sequence was predicted to recognise the HDD, silent mutations were incorporated using SnapGene® 5.0.8 software (Dotmatics, Boston, MA, USA) to avoid recurrent endonuclease activity *in vivo*. The complete sequence of the HDD can be found in the supplementary material.

One day after *cell passage*, $4x10^5$ A20 cells resuspended in 8,5µL of Buffer R were mixed with 3µL of the target RNP (sgRNA:spCas9 in 4:4,8 µM ratio), 0,52µL of 100µM HDD oligo and

0,52µL of 100µM electroporation enhancer. Then, as commented above, 10µL of the volume was electroporated using the Neon™ system. The cells were incubated in 2 mL of A20 media (*see* cell lines section) without antibiotics supplemented with 1,7µL of 0,69 mM Alt-R HDR Enhancer V2 (IDT) or DMSO. The day after, the cells were harvested and counted, and the DMSO and Alt-R HDR Enhancer V2 conditions commonly merged due to the HDR Enhancer's high toxicity. Two days later, cells were harvested, and single cells were seeded in wells of 96-U-well plates by limited dilution, as commented before. Ten to twelve days later, the DNA of scd A20 cells was obtained as detailed previously and the clones with the knock-in the targeted region were detected by the number and sizes of PCR amplicons since a 3xFlag-recognising

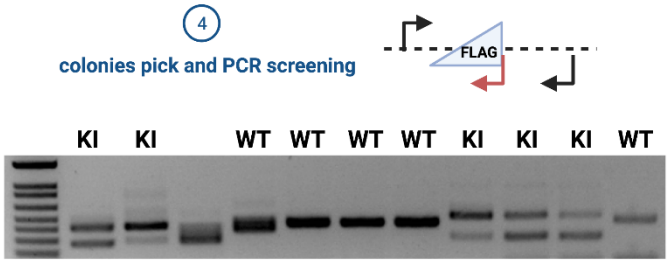

primer (5'- cttgtcatcgtcatccttgta 3') was included as it is shown in Figure 6.

Figure 6: **Three-primers PCR to the detection of 3xFlag knock-in clones**. In black, the representation of primers is used to amplify the target amplicon, and in red, the primer is used to recognise clones bearing the coding 3xFlag sequence. Each line represents a different clone. The clone was identified as knock-in (KI) when two amplicons were identified. Conversely, a wild-type (WT) locus was assumed for that clone when a single PCR product was observed.

The zygosity of the candidate clones was analysed in a second PCR without the 3xFlag primer. The PCR amplicons were later sanger-sequenced to corroborate the fidelity of the HDD incorporated, and homozygous knock-in clones were then expanded and stored. The 3xFlag-tagged protein expression was ultimately verified by western blot.

Table III: Primers used to generate amplicons of interest and their related sgRNAs

Target	Experiment	Sense	Primer (5´ → 3´)	sgRNA (5´ → 3´)
Stau1	Knock-out	Exon1_Forward	TGGCTGTTAGCATCAGTGTC	ACCTACAGCTATGGCATGCG
		Exon10_Reverse	GTTAGTGGCCTCAGAAAGAGG	
		Exon10_Forward	GTCTGGGATGAGAATGGCTTAT	CACAGCCGCCTCTCGTCAGT
	Knock-in (N-terminus)	Forward	CCCAGGTTTTTCCCGTGATTCTG	GGGTCCACGGGCTTATACAT
		Reverse	ACAGTCCCAGCACAGTACCAA	
Stau2	Knock-out	Brie_Forward	GCATACATTTCTGGGGTATTTATAAAATTGATATCCAAAC	AGAGCTAACTACAACTTCCG
		Brie_Reverse	ATGCAAGGCCATTAACGCAG	
		Yusa_Forward	TACTGCTAACCCTGTATTAATTGCTAATGTTTACT	GGTAGTATAACTCCAACTG
		Yusa Reverse	GTACATTAGCAAAGAAAGCTTCTGAGGCTA	
	Knock-in (C-terminus)	Forward	CTTTAAAATGTCACTTTTGTGGTGACCTTTGAAT	GGACTGCAAGAAATCAAAGT
		Reverse	GAAATGCTCAAAGTTTTATTTTCCCCCAGT	
		Reverse	AGTTCAGCCTTTCCAAATAAAACATTCCT	

3xFlagged-proteins immune-precipitation (IP)

The scd A20 clones bearing the 3xFlagged proteins commented above, and not-tagged scd control clones were expanded, harvested, counted and then extensively washed with cold DPBS 1x. Later, cell pellets were resuspended (2,5-3x10^7 cells/mL) in proteases/phosphatases inhibitor cocktail-supplemented IP Buffer (Pierce, Thermo Fisher Scientific) and frozen at -80ºC until use. On an experimental day, the protein extracts were thawed and centrifuged at 16000g for 15 minutes at 4ºC to separate the proteins from cell debris and DNA. Then, the clear proteinic phase at pH ~7 was 0,22 μm-filtered, pre-cleared by 30 minutes incubation with 20 μL/mL of IgG crosslinked to agarose beads (Sigma-Aldrich), and its concentration was ultimately determined using DC™ Protein Assay kit.

Pre-cleared 7,5 mg of protein extract of each clone was incubated with 40μL of Ultra-pure bovine serum albumin (BSA; Fermentas; Thermo Fisher Scientific) and yeast tRNAs (Roche, Basel, Switzerland) blocked magnetic M2 beads (Merck) overnight at 4ºC with gentle rotation. The next day, the beads loaded with the target 3xFLAG-RBPs were separated from the unbound fraction by magnetic separation and incubated with 30μg of RNase A/T1 mix (Thermo Scientific) for 1 hour to release RNA-dependent interactors in the so-called first fraction. Afterwards, the magnetic beads were obtained and resuspended with 40μL of 2x Tris-glycine buffer (125 mM Tris, 384 mM Glycine, 0,5% SDS). The mix was boiled at 95ºC for 10 minutes to release the tagged proteins and their interactors from the beads in the so-called second

fraction (eluate), which was ultimately depleted of destroyed beads and diluted two times with Halt^{TM}-supplemented IP buffer.

The enrichment of the tagged proteins was confirmed by 3xFLAG western blot comparing the input, the unbound and the second fraction of the IP. After, the proteins present both in the first and second fractions were determined by liquid chromatography coupled to mass spectrometry (LC-MS/MS).

Sample preparation of scd A20 cells for proteome determination by LC-MS/MS

Scd A20 control, single and double Stau knockout clones were cultured, expanded, and harvested, and 10^7 cell pellets were frozen at -80ºC until use. These samples were then processed by the proteomics core unit BayBioMS@MRI (TranslaTUM, Faculty of Medicine, Technical University of Munich). In detail, cells were lysed in 200µL of 8 M Urea in 50 mM Tris-HCl (pH = 7,5) and sonicated three times for 1 minute. Then, the DNA was hydrolysed, adding 2µL of 1% trifluoroacetic acid (TFA) and the pH was subsequently adjusted to 8,5, adding 7µL of 3 M Tris solution. The whole preparation was centrifuged at 18000g for 5 minutes at 4ºC, and the protein phase was moved to a fresh ProteinLobin® tube. The protein concentration was determined, and 200 µg was used as input. Disulfide bonds were reduced with 10 mM DTT for 45 minutes at 25°C, followed by alkylation of cysteines with 55 mM 2-chloracetamide (CAA) for 30 minutes at room temperature. Then, the proteins were 1:5 diluted with digestion buffer (2 mM $CaCl_2$ in 50 mM Tris-HCl, pH 8.5) and incubated with Trypsin [1:50 (w/w) enzyme-to-protein ratio] overnight at 37°C with gentle agitation (700 rpm). The next day, samples were desalted by adding formic acid (FA) to a final 1% concentration.

Peptide purification was performed using SepPAC50 columns equilibrated consecutively with 250µL 100% acetonitrile (ACN), 250µl elution solution (50% ACN, 0,1% FA; from now on as ds_B) and three times with 250µL washing solution (0.1% FA; hereafter as ds_A) at 1000g. Samples were loaded on the column and spun for 5 minutes at 500g, followed by reapplication of the flow through. Subsequently, the columns were washed two times with ds_A. Finally, the peptides were eluted twice with 150µL ds_B. Peptide eluates were vacuum-dried and frozen at -80ºC.

To perform the fractionation of the peptides, these were resuspended in pH-Reverse-Phase Buffer (5% ACN, 2,5 mM Ambic; bRP_A) at 2,5 µg/µL and then 75µL were loaded onto Xbridge BEH130 C18 columns with a 3,5 µm particle size and a 2,1 x 150 mm length. Finally, 96

fractions were collected, pooled to 48 and then acidified with 2µL 100% FA before vacuum dried and frozen at -80ºC.

Sample preparation for 3xFlagged-proteins interactors determination by LC-MS/MS

Also, in the proteomics core unit BayBioMS@MRI, the proteins from the eluate of the IPs (mentioned before) were precipitated with cold acetone and then dissolved in 50µL of water. To remove any salt and SDS remaining, 200µL of methanol, 50µL of chloroform and 150µL of water were sequentially added to the samples. The proteins were then precipitated by centrifugation, washed with methanol and then precipitated again by centrifugation for 5 minutes at 1300 rpm. Lastly, the protein pellets were vacuum-dried and frozen at -80ºC until use.

Proteins were treated with 30µL of urea buffer (8 M urea, 50 mM Tris-HCl, 10 mM DTT, pH=7,5) for 45 minutes at 37ºC. Then, the alkylation of cysteine and digestion of proteins for the cell pellets was performed as discussed. Later, stage tip peptide purification was performed using *in-house* build C18 tips with three C18 discs. Stage tips were equilibrated consecutively with 250µL 100% ACN, ds_B and then twice ds_A. Samples were loaded on the column and spun for 5 minutes at 500g, followed by reapplication of the flow through. Subsequently, the stage tips were washed once with ds_A. Finally, the peptides were eluted two times with 40µL of ds_B. Peptide eluates were vacuum dried and resuspended in 20µL 0,1% FA before LC-MS/MS analysis.

LC-MS/MS data acquisition

LC-MS/MS analysis for the fractioned peptides derived from the cell pellets was performed on an Exploris mass spectrometer (Thermo Fisher Scientific) coupled to a Vanquish Neo microflow system.

LC-MS/MS analysis of the peptides derived from the IP eluates was performed on an Eclipse mass spectrometer (Thermo Fisher Scientific) coupled online to a Dionex Ultimate 3000 RSLCnano system. The liquid chromatography setup consisted of a 75 µm x 2 cm trap column and a 75 µm x 40 cm analytical column, packed *in-house* with Reprosil Pur ODS-3 3 µm particles (Dr. Maisch GmbH). Peptides were loaded onto the trap column using 0,1% FA in water at a flow rate of 5 µL/min and separated using a 110 min linear gradient from 4% to 32%

of solvent B (0,1% (v/v) formic acid, 5% (v/v) DMSO in acetonitrile) at 300 nL/min flow rate. NanoLC solvent A was 0,1% (v/v) formic acid and 5% (v/v) DMSO in HPLC-grade water. The Eclipse mass spectrometer was operated in data-independent acquisition (DIA) and positive ionisation mode. DIA was performed with one entire MS event followed by 40 MS/MS windows in one cycle, resulting in a cycle time of 3 seconds. The full MS settings included an automatic gain control (AGC) target value of 100% in the 360 – 1,300 m/z range with a maximum injection time of 50 ms and a resolution of 120 000 at m/z 200. Forty variable DIA precursor windows ranged from 368 m/z (lower boundary of 1st window) to 1,179 m/z (upper boundary of 40th window). Precursor ions were fragmented by HCD and had a normalised collision energy of 30%. MS/MS spectra were acquired with an AGC target value of 1000% for the precursor window with a maximum injection time of 54 ms and a resolution of 30,000 at m/z 200.

LC-MS/MS data analysis

DIA-NN version 1.8.1 (PMID31768060) was used to generate an in-silico predicted spectral library composed of the mouse proteome (UniProtKB reference proteome, UP000000589) and common contaminants (MaxQuant contaminants. fasta) with trypsin as digestion enzyme and one missed cleavage specified. Subsequently, the acquired raw files were processed in library-free mode using DIA-NN default settings, and the match between runs function was enabled.

Bulk 3’ RNA sequencing

The total RNA from $5x10^6$ cells pellets of scd A20 single and double Stau knock-out cells was obtained using RNeasy Micro Kit (Qiagen) following the manufacturer’s guidelines. Then, the quality and concentration of RNA were measured with a fragment analyser (2100 Bioanalyzer; Agilent Technologies, CA, USA) using RNA 6000 Pico Kit (Agilent Technologies) following the producer’s protocol.

Dr Rupert Öllinger from the Experimental Cancer Genetics Laboratory, led by Prof. Dr Roland Rad (Technical University of Munich), processed the RNA samples similar to those published before [99]. Briefly, 20µL at 5 ng/µL of RNA for each piece was retro-transcribed using oligo-dT primer containing barcodes, unique molecular identifiers (UMIs) and an adaptor. Then, 5’ ends of the cDNAs were extended by a template switch oligo (TSO) and after pooling of all samples, full-length cDNA was purified with DNA Clean & Concentrator™ (Zymo Research, CA, USA) according to the manufacturer’s protocol. Purified cDNA was amplified with primers binding to the TSO site and the adaptor. Then, 0,8 ng of cDNA was fragmented with the

Nextera XT kit (Illumina, CA, USA), and 50-70 bp of 3' end-fragments were finally amplified using primers with Illumina P5 and P7 overhangs. The library was pair-end sequenced on a MiSeq Illumina Sequencer (Illumina) with 16 barcodes and UMIs and 50 cycles for the cDNA. Data were processed by Dr Thomas Engleitner using the published Drop-seq pipeline (v1.0)[100] to generate sample- and gene-wise UMI tables. Reference genome (GRCm38) was used for alignment. Transcript and gene definitions were used according to the ENSEMBL annotation release 106. Further analyses were performed with R version 4.2.1.

Infra-red UV-crosslinked IP (irCLIP)

The irCLIP analysis was performed with Dr Twm Mitchell at the laboratory of Prof. Dr Martin Turner in The Babraham Institute (Cambridge, UK) following a previously published protocol [101]. In detail, a total of $2{,}5x10^7$ of scd-A20 3xFLAG-STAU1, STAU2-3xFLAG or control cells were crosslinked at 150 mJ/cm^2 with 245 [nm] radiation in a Stratalinker 2400, and cell pellets in Protein LoBind® tubes were snap frozen on dry ice until use. Cell pellets were then lysed with protease inhibitors-supplemented buffer (1 mL; 50 mM Tris-HCl, 100 mM NaCl, 1% IGEPAL CA-630, 0,1% SDS and 0,5% Sodium Deoxycholate; pH=7,4) and sonicated three times during 15 seconds at 20% intensity. Later, the protein extracts were pre-cleared with two sub-sequential incubations with Protein A/G dynabeads (Invitrogen™; 10µL beads/mL sample) for 1 hour and 30 minutes, respectively. After, the protein concentration of the pre-cleared extracts was determined, and between 2-4 mg were treated with RNase I (Ambion; 0.006 U/ml) and Turbo DNase (Ambion; 2 U/ml) at 37°C for 3 minutes at 1100 rpm. BSA-blocked M2 beads were incubated with lysates under rotation overnight at 4°C. The next day, 3xFlagged-proteins-RNA complexes were magnetically separated, and RNA was de-phosphorylated using FastAP Alkaline phosphatase (Invitrogen EF0651) for 40 minutes at 37°C 1100 rpm. IRDye-linked pre-adenylated adaptors were ligated to RNA using T4 RNA ligase I (New England Biolabs; NEB; MA, USA, M0437M) in the presence of 11,25% PEG8000, at room temperature for 75 min. Non-ligated adaptors were removed using RecJF 5′-3′ exonuclease (NEB; M0264S) for 1 hour at 30°C at 1100 rpm, and RNA was de-adenylated using NEB deadenylase (M0331S) for 30 minutes at 37 °C at 1100 rpm.

3xFlagged-proteins-RNA complexes were removed from magnetic beads by re-suspending in DTT-supplemented (100 mM) LDS buffer (Invitrogen™) and heating to 70°C for 1 minute at 1100 rpm. The supernatant was loaded onto pre-cast 4-12% Bis-Tris gel (NuPage; Invitrogen™) and resolved by running for 65 minutes at 180 V with 0,5L MOPS buffer. Complexes were transferred to nitrocellulose membrane using the iBlot™ 2 system (Invitrogen™) for 7 minutes with a mixed range voltage programme. Nitrocellulose membranes

were scanned using Licor Odyssey, and 3xFlagged-proteins-RNA complexes were excised from membranes by cutting 35–55 kDa above the expected running weight of the Stau proteins (55 kDa). Proteins were digested by incubating the membranes at 50°C for 1 hour with proteinase K (Merck) diluted in PK-SDS buffer (10 mM Tris-HCl, 100 mM NaCl, 1 mM EDTA, 0,2% SDS, pH=7,4). The supernatant was mixed with phenol:chloroform:isoamyl alcohol, transferred to a 2 mL phase-lock gel tube, and spun for 5 minutes at 17,000g at room temperature. Chloroform was added to the top phase, and samples were centrifuged for 5 minutes at 17000g at 4°C. The aqueous phase was isolated, and RNA precipitated overnight at −20°C with 100% Ethanol, 1 M NaCl and Glycoblue (0,1% v/v) [Ambion™ AM9515].

Reverse transcription was conducted using Superscript IV (Invitrogen™ 18090010) and 1 pmol/µL irCLIP_ddRT primers featuring 5 nt UMI. cDNA was purified using AMPure XP beads (Beckman Coulter A63881) and circularised in the presence of Beatine (1 M) using CircLigase II (Lucigen CL9021K). PCR amplification was conducted using P5 and P3 solexa primers (Illumina) and Phusion HF master mix (NEB M0536S). PCR products were run on 6% TBE gel and DNA in the 180-300 nt range isolated using standard methodology. The quality and concentrations of iCLIP libraries were checked by the KAPA Library Quantification Kit (Roche) and Bioanalyzer. Finally, the libraries were multiplexed and sequenced using HiSeq2500-RapidRun (200 bp Single End).

Staufen irCLIP mapping

Multiplexed sequencing files from irCLIP data were loaded onto iMaps (https://imaps.genialis.com/iclip). There, the sequences were mapped to the GRCm38 mouse genome using bowtie2, and the reads from different clones were identified and de-multiplexed by the sequence of barcoded adaptors. Later, the libraries for each Stau paralog were merged, and the significant targets were identified using the pipeline from https://github.com/LouiseMatheson/Process_CLIP_data.

RESULTS

Staufen 2 is dispensable for spontaneous germinal centre B-cell differentiation

My proteomic and expression analyses and preliminary experiments in the GCB cell-like A20 B cell line (see below) suggested roles for Stau2, specifically in GCB cells. To investigate the role of Stau2 in these cells, I set out to generate and analyse mice with B cell-specific Stau2 deficiency.

Stau2 possess one TBD and five dsRBDs, forming two tandems able to bind RNA: the tandem dsRBD1-dsRBD2 and the dsRBD3-dsRBD4 [102]. Embryos carrying the promotor-driven "knockout-first" reporter tagged allele [87], called Tm1a, in the neighbourhood of the exon 4, which encodes the majority of dsRBD1 and its link with dsRBD2, in the Stau2 locus (C57BL/6N-A^{tm1Brd} Stau$^{tm1a(EUCOMM)Wtsi}$/^{WtsiH}) were generated by the Wellcome Trust Sanger Institute Mouse Genetics Project. Adult mice with one Tm1a allele were obtained from the European Mouse Mutant Archive partner MRC Harwell Institute and then crossed with mice expressing an optimised Flp recombinase [88] (B6N(B6J)-$^{Tg(CAG-Flpo)1Afst}$; MGI: 4453967) to obtain the LoxP-flanked exon 4 allele (Tm1c) in the offspring. Homozygous Stau2 Tm1c mice (hereafter as Stau2$^{F/F}$) were crossed with hemizygous mice for the hCre-recombinase driven by the immunoglobulin-associated alpha (CD79A or Mb1) locus [103] (Cd79a$^{tm1(cre)Reth}$/Cd79a^{+}; MGI:3687451; hereafter as Mb1$^{cre/+}$) to generate B cell-specific Stau2-deficient mice as shown in the diagram of Figure 7.

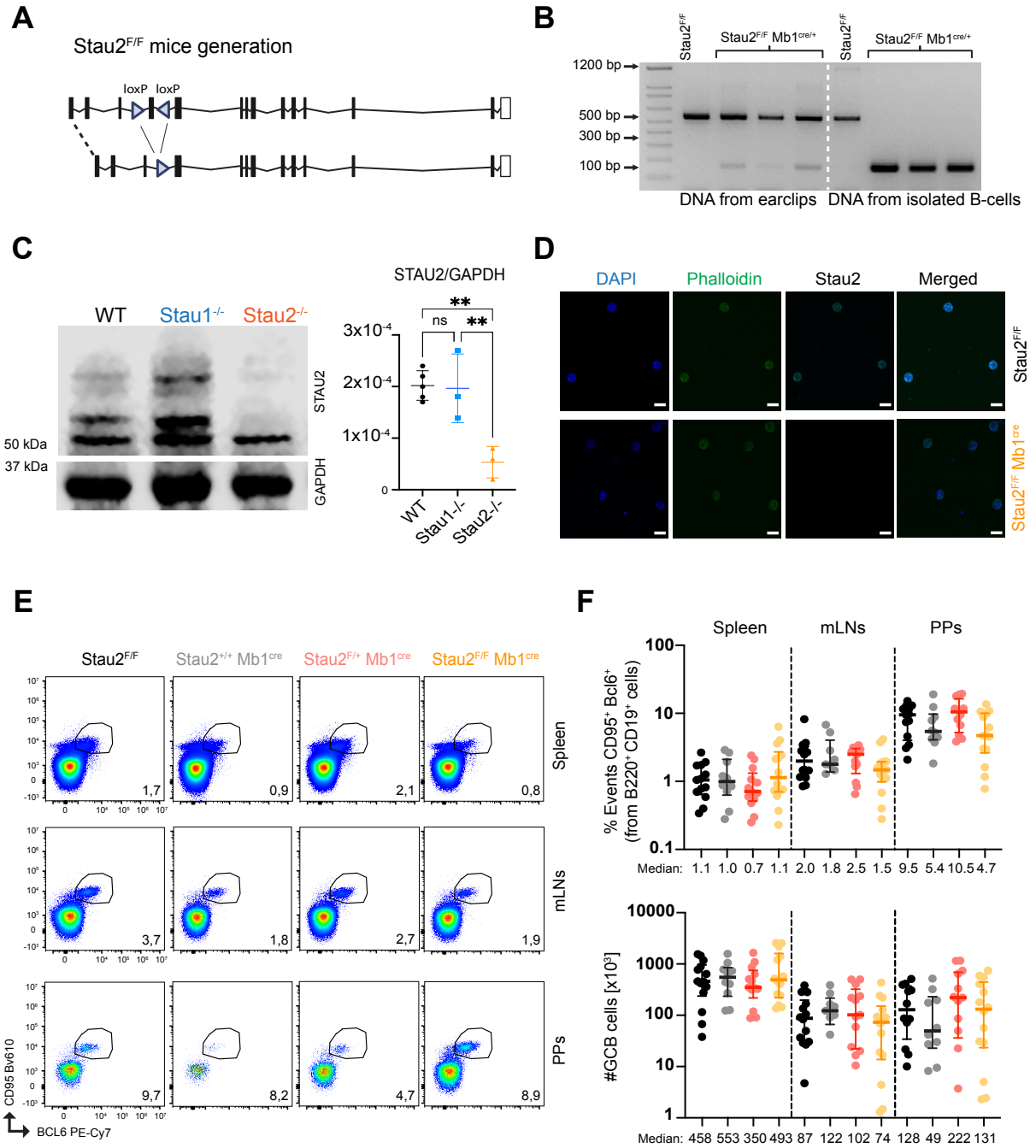

Figure 7: Stau2 is dispensable for spontaneous germinal centre B-cells generation. **A**. Diagram representing the deletion of the exon 4 of Stau2 upon Cre-recombination in B-cells. **B**. Agarose gel showing PCR bands generated from amplifying the neighbourhood of the exon 4 of Stau2 using as template DNA of the ear clips and B-cells. **C**. Western blot nitrocellulose membrane (left) and quantification (right) of STAU2 in proteins extraction from the cerebellum of WT and whole-body Stau1 and Stau2 Knockout mice, respectively. **D**. Immunofluorescence of STAU2 in primary GCB cells obtained from vavP-Bcl2 mice sufficient (upper row) or deficient (bottom row) for Stau2 in B-cells. **E**. Pseudocolour dot plots showing GCB cells ($CD95^+BCL6^+$) in the spleen (top), mesenteric lymph nodes (mLN; middle) and Peyer´s patches (PPs; bottom) in mice sufficient (black and grey columns), haploinsufficient (red column) and insufficient for Stau2 (orange column). **F**. Proportion (top) and number (bottom) of GCB cells in the different analysed tissues and genotypes. In F, the data from 3-4 independent experiments are shown

together, finding no statistical differences in any measurements using a one-way ANOVA t-test with Dunnett´s multiple comparisons test between the mean of each genotype with the control. In C and F, every dot represents the data from one mouse. In C, ** represents *p*-value < 0,01 obtained using ANOVA t-test comparing the mean of each column against all others.

The deletion of the exon 4 of Stau2 by Cre-mediated recombination in B-cells was assessed by electrophoresis, comparing the PCR product sizes obtained using DNA from ear clips and isolated splenic B-cells from the same mice (Figure 7B). As expected, in the samples from mice carrying Cre-recombinase and Tm1c Stau2 alleles (Mb1Cre Stau2$^{F/F}$), complete recombination of the loxP-flanked DNA sequences was observed in DNA isolated from B-cells, but almost no recombination in the DNA from ear clips, which yielded the same PCR product as obtained from both ear clip and B-cells of control mice (Stau2$^{F/F}$).

Due to the early activity of the Mb1 locus in germ cells [104], our breeding strategy also generated whole-body recombination of exon 4 of Stau2 in ~7% of the offspring. Stau2 knockout (Stau2$^{-/-}$) mice were subsequently bred and analysed compared to their WT littermates. Protein extract from their cerebellum was used to corroborate that the lack of exon 4 is sufficient to reduce Stau2 expression by Western blot. In the Stau2$^{-/-}$ cerebellum, an almost complete absence of the Stau2 isoforms 52, 59, and 62 kDa was observed, which were present in WT and Stau1$^{-/-}$ (described further below in this thesis) samples (Figure 7C). The Western blot signals corresponding to Stau2^{52} were quantified and normalised to GAPDH. This revealed no difference between cerebellum protein extracts from WT and Stau1$^{-/-}$ mice but a clear reduction in samples obtained from Stau2$^{-/-}$ mice.

To corroborate the expression of Stau2 in GCB cells detected in the proteome of primary cells (Figure 3), B cell-specific Stau2-deficient mice were crossed with transgenic mice expressing the human Bcl2 gene under the panhematopoietic Vav promotor (C57BL/6$^{Tg(Vav-BCL2)1Jad}$; vavP-Bcl2^{Tg}), which have splenomegaly, an expanded GC compartment and develop either autoimmunity (15-25% of the mice between 40-72 weeks) or follicular lymphoma (~50% of the mice after 72 weeks) later in life [105]. Mice were analysed between 16 and 18 weeks old when splenomegaly and GC expansion were expected, without showing autoimmune or follicular lymphoma-related phenotypes. Using magnetic separation, GCB cells were purified, and the Stau2 expression was assessed by immunofluorescence observing signals in the control cells but none in the Stau2-deficient vavP-Bcl2^{Tg} GCB cells (Figure 7D).

Together, these experiments confirm that by removing exon 4 of Stau2, I could generate a functional Stau2 knockout.

As the next step, spontaneous GCB cells ($BCL6^{+}CD95^{+}$) were evaluated by flow cytometry in different tissues (Figure 7E). I did not observe statistically significant differences in the proportion of GCB cells within the overall B-cell population or in their absolute cell numbers (Figure 7F) among the genotypes. The Mb1cre control mice were also included in these analyses to control for potential effects of Cre enzyme expression in B cells [106]. No significant differences were observed between $Stau2^{F/F}$ and $Stau2^{+/+}$ $Mb1^{cre}$ mice.

Stau2 deficiency restricted to Mb1-expressing cells does not affect bone marrow B-cell development

Considering a previous publication demonstrating that mice lacking Stau2 expression in all tissues contained decreased cell numbers in the femur bone marrow [83], this tissue's cellularity and the B-cell developmental stages were analysed in the B cell-specific Stau2 knockout mice. The results are shown in Figure 8.

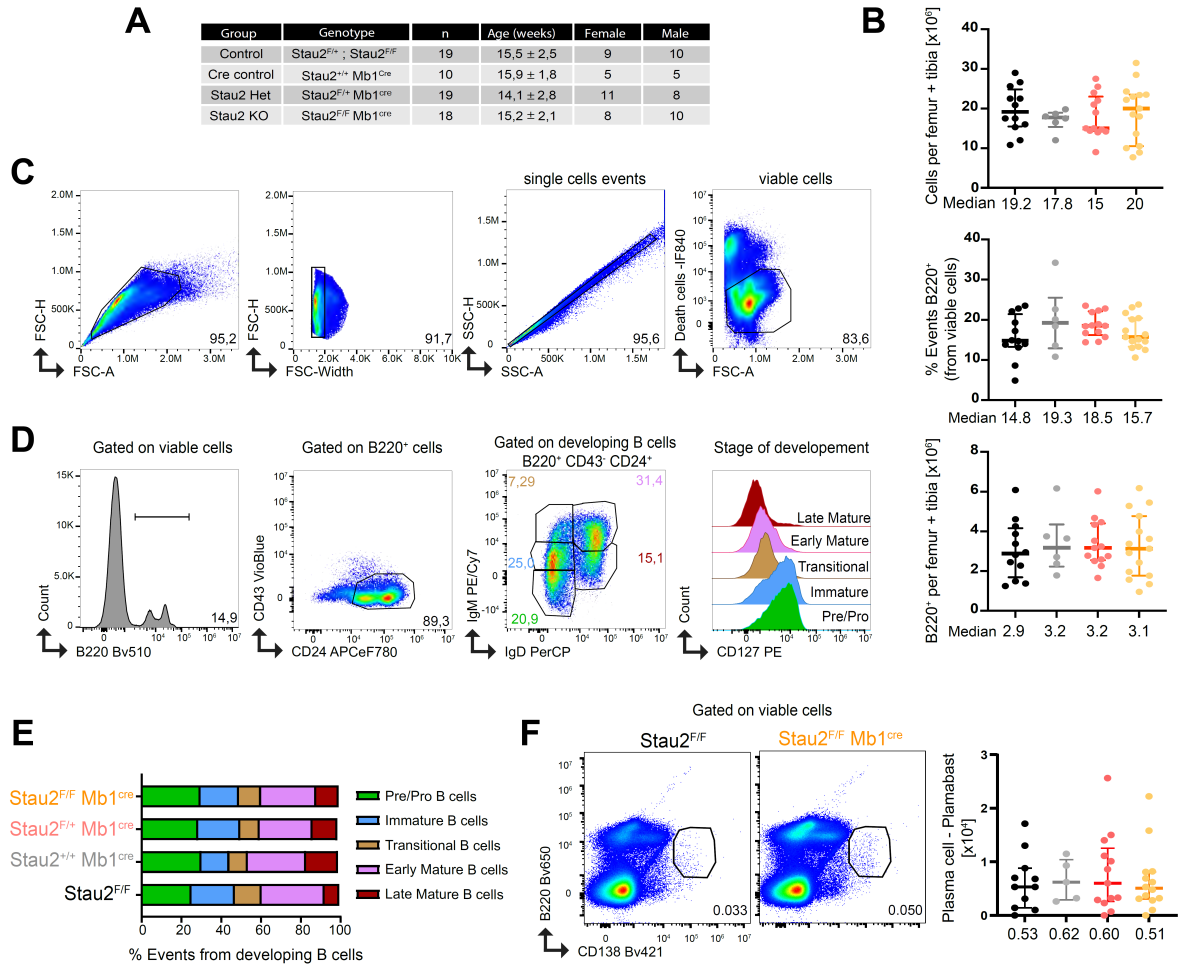

Figure 8: Stau2 expression is not required for B-cell development. **A**. table detailing the age and sex of the mice analysed for each genotype. **B**. Bone marrow cells number from femur and tibia (top), percentage (middle) and number (bottom) of $B220^+$ cells in bone marrow for each genotype. **C**. The gating strategy is used in all flow cytometry analyses to obtain viable single cells. **D**. Representative gating strategy to determine developmental stages of B-cells. From left to right: total $B220^+$ cells; developing B-cells gating ($CD43^-CD24^+$); stage of development of B-cells depending on the expression of IgD and IgM; and differences in the expression of the chain of the receptor for IL-7 (CD127). **E**. Grouped plot showing the mean of the different B-cells in all the genotypes. **F**. Plasma cell/plasmablast ($B220^{+/-}$ $CD138^+$) gating strategy (left) and number (right) in the analysed genotypes. In B and F, the data from 3-4 independent experiments are shown together, finding no statistical differences in any measurements using a one-way ANOVA t-test with Dunnett´s multi-comparison between the mean of each genotype and the control. Every dot represents the data from one mouse.

Mice containing B cell-specific heterozygous or homozygous Stau2 knockout have similar cellularity in the bone marrow of the femur and tibia, a similar percentage of $B220^+$ cells and a similar number of B-cells compared to control mice (Figure 8B). Moreover, all analysed genotypes have an equal developmental B-cell distribution (Figure 8E) and plasma cells/plasmablast numbers. These results suggest that the expression of Stau2 in other bone

marrow-related cells is responsible for the phenotype observed in whole-body Stau2 knockout mice reported previously [83].

Stau2 expression is dispensable for mature B-cell populations in the spleen

In addition to evaluating the roles for Stau2 expression in spontaneous GCB cell generation, B1 and B2 (including follicular and marginal zone B cells) B-cells were analysed in the spleen and shown in Figure 9, observing Stau2 does not influence the proportion nor number of any of the studied B-cell populations.

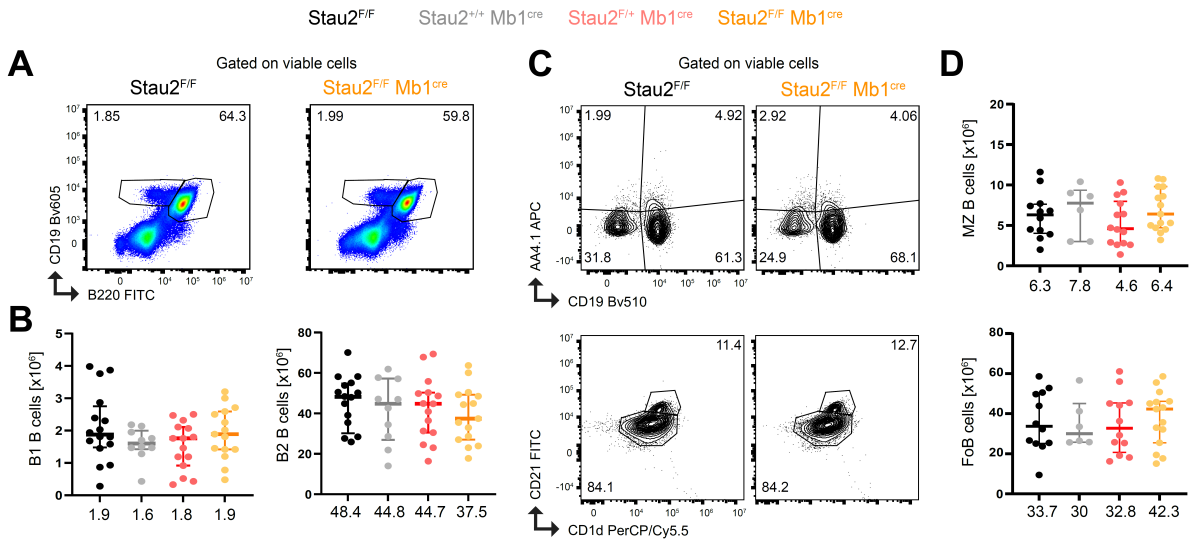

Figure 9: Stau2 deficiency does not alter the proportion of B1 and B2 B-cells. **A**. Representative pseudocolour dot plot showing the gating for B1 ($CD19^+B220^-$) and B2 ($CD19^+CD19^+$) B-cells for control (left) and Stau2 deficient (right) mice. **B**. Scatter plot showing the median ± interquartile range cell number of B1 (left) and B2 (right) B-cells for all genotypes. **C**. Representative contour plots showing the gating of mature B-cells ($CD19^+$ $AA4.1^-$; top), follicular (FoB) and marginal zone (MZ) B-cells (bottom) for control (left) and B-cell specific Stau2-insufficient (right) mice. **D**. Scatter plot showing the median ± interquartile range cell number of FoB (top) and MZ (bottom) B-cells for all genotypes. In B and D, the data from 3-4 independent experiments are shown together, finding no statistical differences in any measurements using a one-way ANOVA t-test with Dunnett´s multicomparison test between the mean of each genotype and the control. Every dot represents the data from one mouse.

Stau1 deficiency does not affect the spontaneous germinal centre B-cells

Stau1 is the ubiquitously expressed paralog of Stau2. To investigate the roles of Stau1 in B-cells and to discover potential redundant functions shared by both Staufen paralogs, we wanted to assess loss-of-function mouse models for Stau1.

Stau1 contain one TBD and four dsRBDs numbered 2 to 5. However, it binds RNA using only its tandem dsRBD3-dsRBD4 [102], present in the two Stau1 isoforms (63 and 55 kDa). Viable and fertile mice containing a *β-Geo* gene trapped in the region encoding dsRBD3 were reported, which produce a truncated Stau1 protein. Truncated Stau1-expressing mice revealed no apparent consequences for brain morphology, learning and memory [47]. To avoid potential complications arising from the expression of a truncated Stau1 protein, we decided to generate our own Stau1 knock-out (Stau1$^{-/-}$) mice, which could not produce any Stau1 protein. To obtain a clean Stau1 knockout model, mouse embryos were electroporated with Cas9-bearing sgRNA RNPs, simultaneously targeting exon 2 and 10 of the Stau1 locus. This procedure generated embryos with a ~14 kb deletion, which were checked by the PCR strategy detailed in the methods section. Then, those embryos were implanted into pseudo-pregnant females, and later, the offspring were genotyped and back-crossed to identify specimens with the mutation in the germline. Later, heterozygous mice (Stau1$^{+/-}$) were intercrossed, obtaining all the possible alleles in the offspring in a Mendelian ratio. Then, the expression of Stau1 was analysed, as shown in Figure 10.

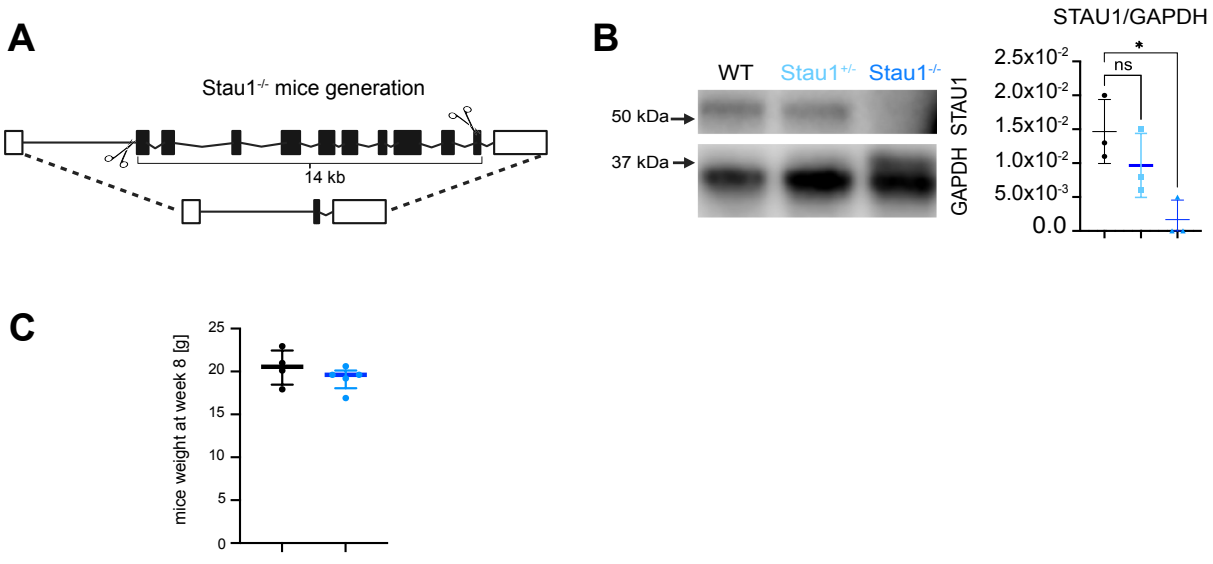

Figure 10: Whole-body Stau1 deficient mice develop normally. **A**. Diagram showing the strategy to knockout Stau1 in newly generated mouse strain. **B**. Western blot nitrocellulose membrane (left) and quantification (right) of STAU1 in protein extracts from the cerebellum of WT, haploinsufficient (Stau1$^{+/-}$) and insufficient Stau1 (Stau1$^{-/-}$) mice. **C**. Scatter plot showing the mean ± SD weight of WT (black) and Stau1$^{-/-}$ (blue) mice at eight weeks old. In B and C, every dot represents the data from one mouse. In B, * mean *p*-value < 0,05 measured by one-way ANOVA with Dunnett´s multicomparison test between the mean of each genotype with the control. In C, no statistical differences were found.

The expression of Stau1 was assessed by Western blot (Figure 10B) in protein extracts obtained from the cerebellum from WT, Stau1$^{+/-}$ and Stau1 KO (Stau1$^{-/-}$) mice, observing the target band at ~50 kDa present only in WT and Stau1$^{+/-}$ samples. After quantifying the Stau1 signal and normalising it with the GAPDH expression in all samples, we identified no significant difference in Stau1 expression between WT and Stau1+/- mice but a dramatic reduction in it in Stau1$^{-/-}$ mice.

Deletion of nearly the entire Stau1 genomic locus does not affect the general development of the mice since Stau1-deficient animals reach adulthood with a similar weight as WT mice (Figure 10C). These findings suggest that the lack of Stau1 is not lethal in mice. To elucidate whether this RBP is relevant in the immune system, I decided to analyse lymphocyte development since it was not studied by the authors who published the above-mentioned mouse line expressing the truncated Stau1 protein.

Staufen 1 expression is not required for lymphocyte development

The in-house generated Stau1-deficient mouse line was analysed to study T and B-cell development in the thymus and bone marrow. The results are shown in Figure 11.

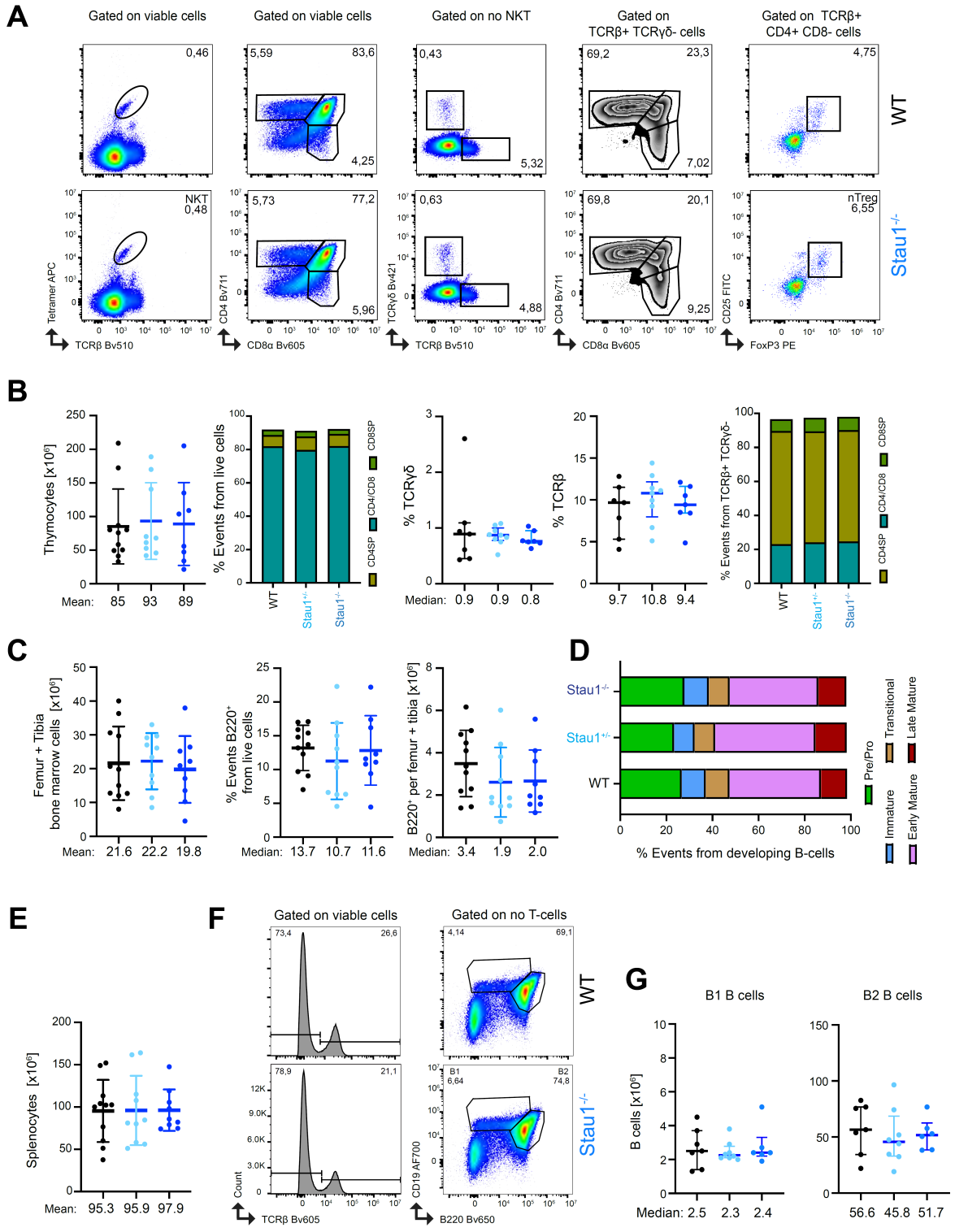

Figure 11: Stau1 does not control T or B-cell development. **A**. Representative gating strategy to identify the major immune populations in the thymus and the T-cell development. From left to right: gating to identify NKT cells; CD4 and CD8 single and double positive total cells; γδT and αβT lymphocytes; mature $CD4^+$ or $CD8^+$ αβ T lymphocytes; and nTreg cells. **B**. Scatter and grouped plots representing the different T-lymphocyte populations in the thymus. From left to right: mean ± SD thymocyte number; mean distribution of CD4 and CD8 single

and double positive in immature lymphocytes; median ± interquartile range proportion of γδT from live cells; median ± interquartile range proportion of αβ T from live cells; mean distribution of CD4 and CD8 single and double positive in mature Tαβ lymphocytes. **C**. Scatter plots showing the mean ± SD bone marrow cell number (left), median ± interquartile range proportion of $B220^+$ cells from live cells (middle) and median ± interquartile range number of $B220^+$ in the bone marrow. **D**. Grouped plot showing the mean distribution of developmental stages of B-cells. **E**. Scatter plot showing mean ± SD splenocytes cell number. **F**. representative histogram showing T-cell identification in the spleen (left) and pseudocolour plot showing B1 and B2 gating (right) in WT (upper) and $Stau1^{-/-}$ (bottom) mice. **G**. Scatter plot showing median ± interquartile range number of B1 (left) and B2 (right) B-cells. In B, C, E and G, every dot represents the data from one mouse, and the plots include the overall data from 3-4 independent experiments. In all scatter and grouped plots, a one-way ANOVA t-test with Dunnett´s multicomparison test was performed between the mean of each genotype and the control, finding no statistical differences.

The data collected suggest that the absence of Stau1 in all tissues does not alter thymus biology since there are no significant differences in the thymocyte cell number, the αβT cell and γδT cell proportion between Stau1 knockout and control mice. Stau1 deficiency did not alter ratios of immature double-negative, double-positive or mature CD4, CD8 single-positive thymocytes (Figure 11B). Similarly, in the bone marrow of the femur and tibia, I found no impact of Stau1 deficiency on the total cell number nor the B-cell numbers and proportions (Figure 11C). The different developmental stages, gated as shown in Figure 8, are very similar among heterozygous and homozygous Stau1 knockout and control mice. Thus, the immunophenotyping in our novel Stau1 knockout mouse line indicates that Stau1 is dispensable for T and B-cell development.

In the periphery, the numbers of B1 cells and B2 B-cell subsets were very similar among the genotypes (Figure 11G), suggesting that Stau1 deficiency does not impact the proportion of splenic B-cells. Therefore, since this doctoral work focuses on the analysis of GCB cells, I studied whether the absence of this paralog affects spontaneous GCB cell generation.

Stau1 deficiency does not affect spontaneous GCB cell generation

Since I observed no differences in the number of splenic B1 and B2 B-cell subsets, I checked other mature B-cell populations in the spleen and peritoneal cavity. The results are shown in Figure 12.

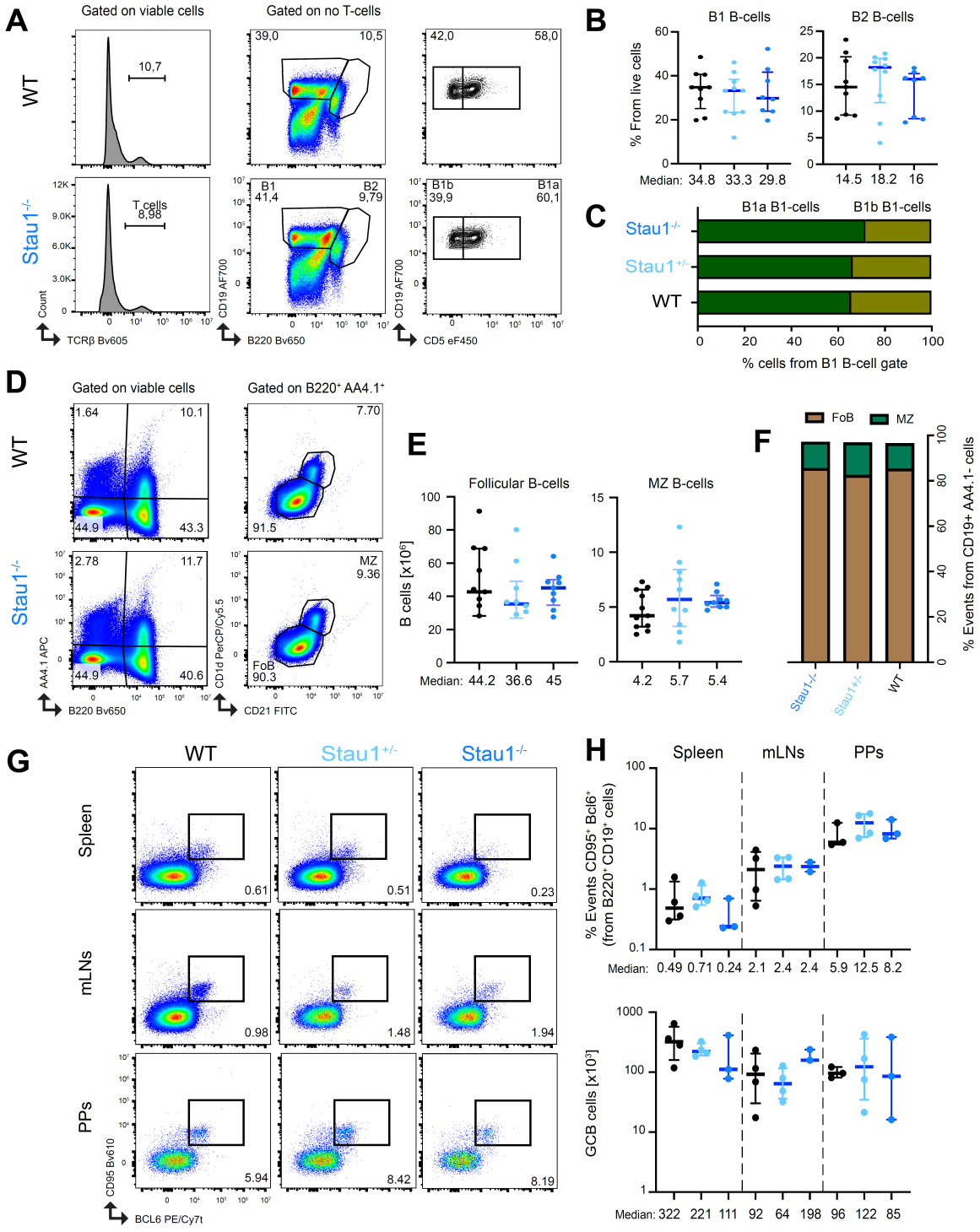

Figure 12: Stau1 is dispensable for GCB cell generation at a steady state. **A**. Representative gating strategy to determine B1 and B2 B-cells in the peritoneal cavity. From left to right: histograms showing T-cell identification; B1 and B2 B-cells gated on no-T-cells; B1a ($CD5^+$) and B1b ($CD5^-$) gating strategy from B1 B-cells. **B**. Scatter plots showing median ± interquartile range proportion of B1 (left) and B2 (right) B-cells in the peritoneal cavity. **C**. Grouped plots showing the mean B1a and B1b distribution in the B1 B-cells from the peritoneal cavity. **D**. Representative pseudocolour dot plots showing the gating strategy to identify FoB and MZ B-cells from mature cells in the spleen. **E**. Scatter plots showing median ± interquartile

range number of FoB (left) and MZ (right) B-cells in the spleen. **F**. Grouped plot showing mean FoB and MZ distribution in splenic mature B-cells. **G**. Representative pseudocolour dot plots showing GCB cells gating in the spleen (top), mLNs (middle) and PPs (bottom) for Stau1 sufficient (left), haploinsufficient (centre) and insufficient (right) mice. **H**. Scatter plots showing median ± interquartile range proportion (upper) and number (bottom) of GCB cells in different tissues. In B, E and H, every dot represents the data from one mouse, and the plots include the overall data from 3-4 independent experiments. In all scatter and grouped plots, a one-way ANOVA t-test with Dunnett´s multicomparison test was performed between the mean of each genotype and the control, finding no statistical differences.

The analysis in the peritoneal cavity indicates that Stau1 is not required for B-cell development and differentiation outside the bone marrow. There was no difference in the proportion of B1 B-cells nor their phenotype in Stau1 knockout mice compared to controls (Figure 12 A-C). Regarding conventional B-cells, similar to what I observed in the B cell-specific Stau2 knockout mice, the absence of Stau1 does not alter the FoB and MZ B-cells distribution or their cell numbers (Figure 12 E-F). More importantly for this doctoral work, the immunophenotyping performed on these mice shows that the deficiency of Stau1 alone does not have any noticeable impact on the spontaneous generation of GCB cells since differences in their proportion or cell numbers were not observed in any of the tested tissues between Stau1 knockout and control mice.

Stau1 is dispensable for the immune composition of the spleen and peritoneal cavity

The performed analysis on the Stau1 knockout mouse revealed no differences in the development of T and B-cells (Figure 11) nor the distribution of classical B1 and B2 B-cell subpopulations in the spleen and peritoneal cavity (Figure 12). Therefore, for the completeness of the immunophenotyping of this novel line, I characterised other classical immune populations in the spleen and peritoneal cavity. The results are shown in Figure 13.

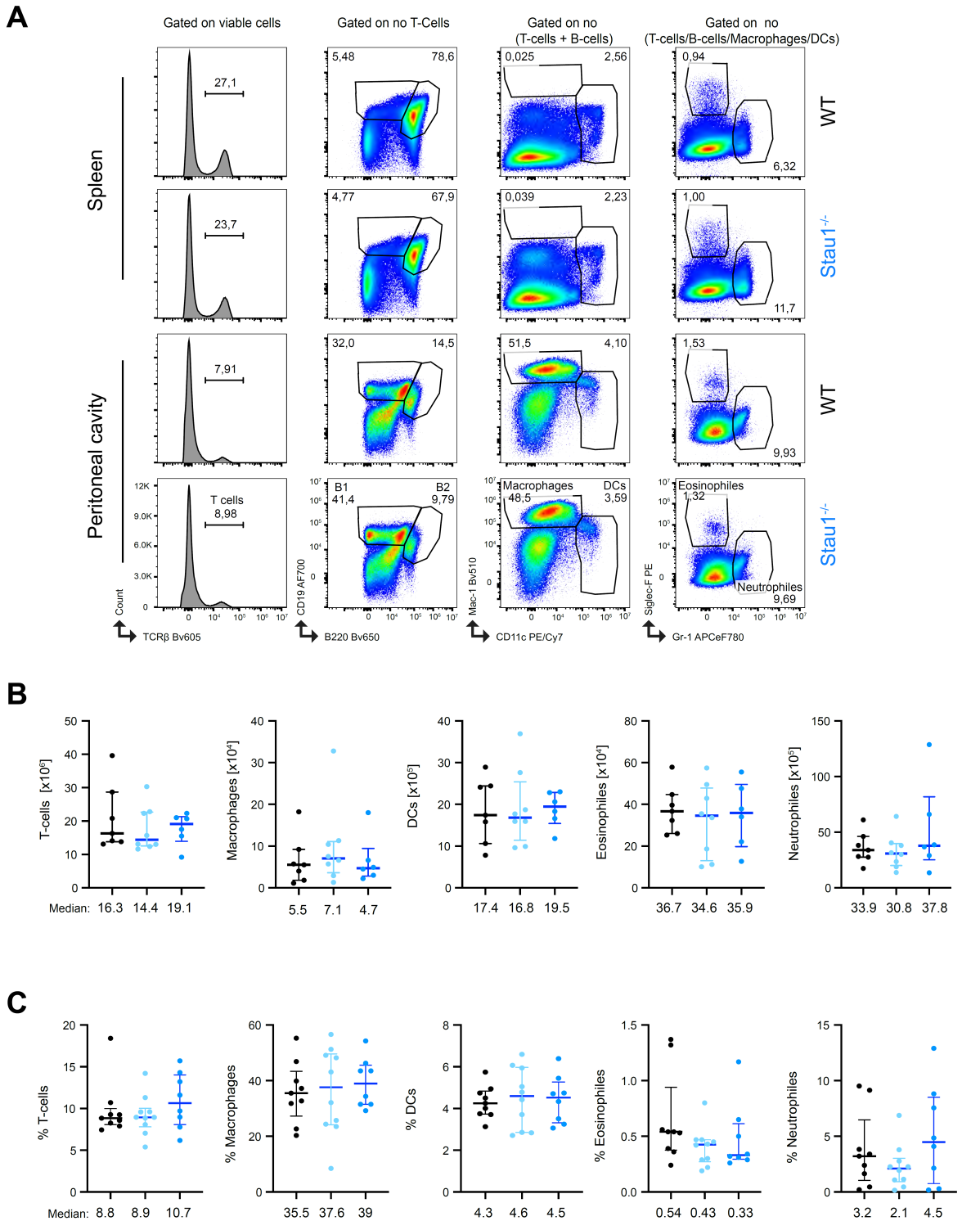

Figure 13: Stau1 expression is not required to develop and maintain splenic immune cell populations. A. Representative histograms and pseudocolour dot plots showing the gating strategy to identify, from left to right: T-cells; B1 and B2 B-cells; Macrophages and Dendritic cells (DCs); and Eosinophils and neutrophils both in spleen and peritoneal cavity. **B.** Scatter plots showing median ± interquartile range number of the analysed populations in the spleen. **C.** Scatter plots showing median ± interquartile range proportion of the analysed populations in the peritoneal cavity. In B and C, every dot represents the data from one mouse, and the plots include the overall data from 3-4 independent experiments. In all scatter and

grouped plots, a one-way ANOVA t-test with Dunnett´s multicomparison test was performed between the mean of each genotype and the control, finding no statistical differences.

The immunophenotyping performed on the spleen and peritoneal cavity of Stau1 deficient mice suggest this paralog is dispensable for splenic immune cell populations since the lack of Stau1 has no consequence for the cell number of the T and B lymphocytes neither in the following myeloid cell-types: macrophages, DCs, neutrophils and eosinophils. This may suggest that any role that Stau1 might have in the homeostasis of the immune cells is redundant with similar functions of Stau2 and/or not essential.

Considering that both Staufen paralogs share some of their targets and both participate in the decay of mRNAs with misplaced introns, I then assessed whether the deficiency of both Staufen paralogs might affect B-cell development and differentiation.

Reduced spleen cell numbers in the absence of both Staufen paralogs

Since it has been reported that Stau1 and Stau2-containing complexes share a fraction of their respective mRNA targets [45], whole-body Stau double knockout ($Stau1^{-/-}/2^{-/-}$) mice were generated by crossing Stau1-deficient with whole-body Stau2 deficient mice. I analysed these $Stau1^{-/-}/2^{-/-}$ mice to study the overall role of the Staufen paralogs in the immune system by uncovering possible overlapping functions between paralogs.

Initially, the development of T and B-cells was analysed, and the results can be observed in Figure 14.

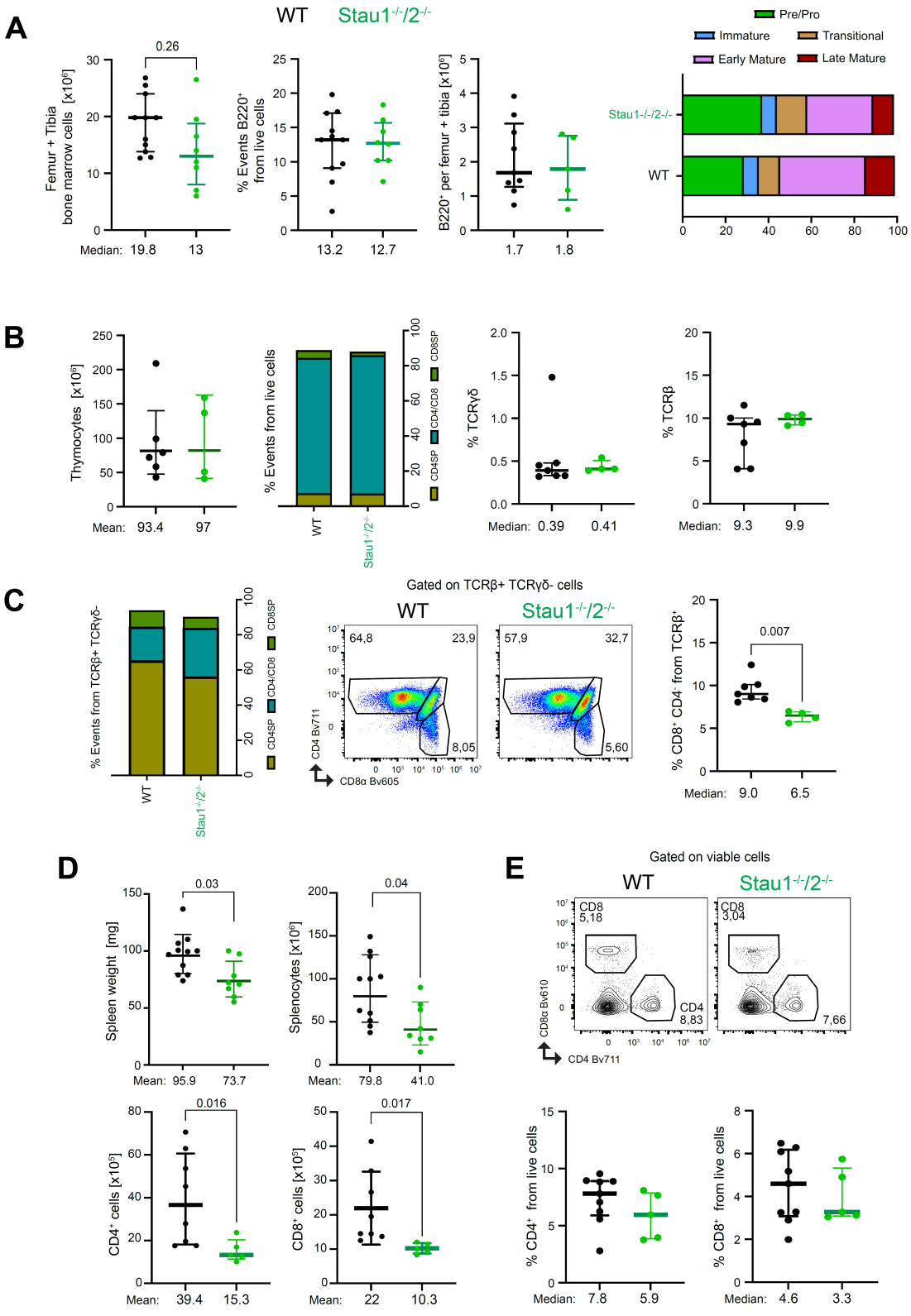

Figure 14: Staufen paralogs promote the spleen's cellularity. **A**. Scatter plots showing median ± interquartile range number of the bone marrow cells, proportion and number of the B220$^+$ cells and mean distribution of the developmental B-cell stages. **B**. From left to right: Scatter plot indicating mean ± SD number of thymocytes; grouped plot showing the mean distribution of CD4 and CD8 single and double positive in immature lymphocytes; median ±

interquartile range proportion of γδT from live cells; median ± interquartile range proportion of αβT from live cells. **C**. From left to right: grouped plot showing the mean distribution of CD4 and CD8 single and double positive in mature αβT lymphocytes; representative pseudocolour plot indicating the gating of CD4 and CD8 single and double positive in mature Tαβ lymphocytes; median ± interquartile range proportion of CD8SP from αβT lymphocytes. **D**. Scatter plots indicating mean ± SD weight of the spleen and number of splenocytes (top), and scatter plots showing mean ± SD number of $CD4^+$ and $CD8^+$ T-cells in the spleen. **E**. Representative contour plots showing the gating to identify $CD4^+$ and $CD8^+$ T-cells in the spleen (Top) and scatter plots indicating median ± interquartile range of proportion of $CD4^+$ and $CD8^+$ T-cells, respectively. In A-E, every dot represents the data from one mouse, and the plots include the data collected from 3-4 independent experiments. In all scatter and grouped plots, a one-way ANOVA t-test with a Dunnett's multiple comparison test comparing the mean of each genotype with the control was performed, finding statistical differences when the *p*-value above the brackets is <0,05.

The most common immune cells and tissues were analysed in naïve adult mice lacking Staufen paralogs. Despite no significant differences in the bone marrow from the femur and tibia, the cell number in Stau1$^{-/-}$/2$^{-/-}$ mice is half compared with the WT control (Figure 14A). However, this does not affect the distribution of the developmental stages of B-cells, which are similar among the genotypes.

I observed no differences in cell numbers in the thymus, neither in CD4 and CD8 single-positive (SP) and double-positive cells in the total live cell numbers nor in the proportion of γδT and αβT cells (Figure 14B). However, the proportion of $CD8^+$ TCR^+ T-cells of all thymic TCR^+ T cells is reduced (Figure 14C). To investigate whether this difference was also present in the periphery, I checked the T-cell population in the spleen. I found no differences in the proportion of $CD4^+$ and $CD8^+$ T-cells (Figure 14E). Still, the cell number of those lymphocytes was reduced, which was not surprising considering the whole cellularity of this organ was diminished by 50% and its weight by ~25% (Figure 14D).

Reduced numbers of splenic B2 B-cells in the absence of the Staufen paralogs

Considering that the whole spleen, but not the thymus nor the bone marrow, was affected in its cellularity in Stau1$^{-/-}$/2$^{-/-}$ mice, I studied how the B-cell populations were affected in the spleen (Figure 15).

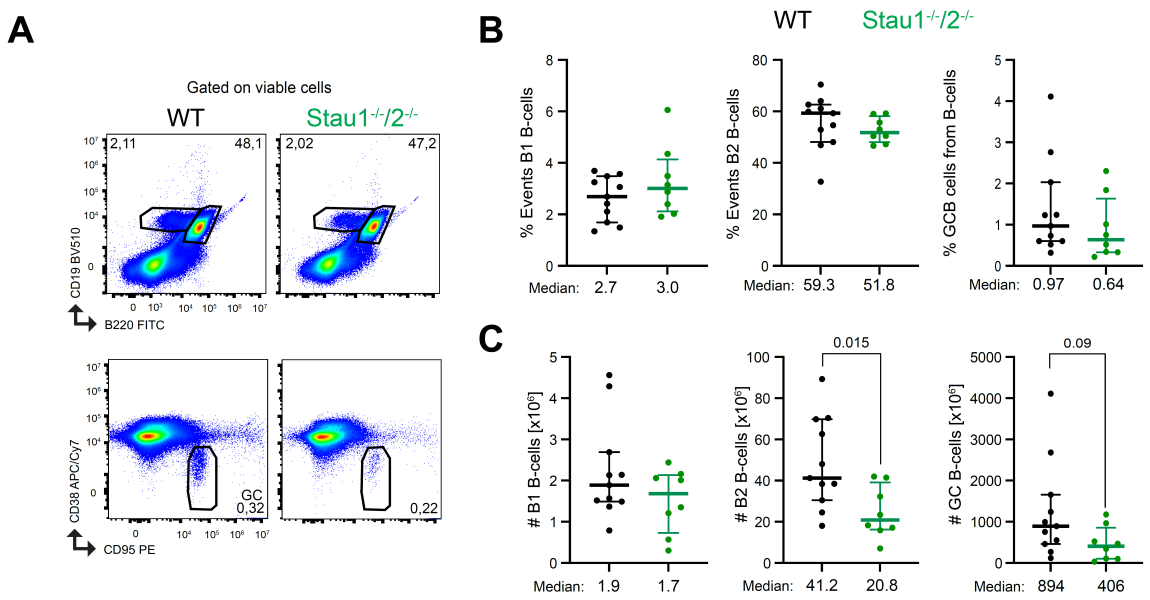

Figure 15: Absence of Staufen paralogs reduces the cell numbers of splenic B2 B-cells. **A**. Representative pseudocolour plot showing B1 and B2 gating strategy (top) and GCB cells ($CD95^+CD38^-$) for WT (left) and $Stau1^{-/-}/2^{-/-}$ (right) mice. **B**. Scatter plot showing median ± interquartile range proportion and number of B1 B-cells (left), B2 B-cells (middle) and GCB cells (right). **C**. Scatter plot showing median ± interquartile range number of B1 B-cells (left), B2 B-cells (middle) and GCB cells (right). In B and C, every dot represents the data from one mouse, and the plots include the data collected from 3-4 independent experiments. In all scatter plots, a one-way ANOVA t-test with a Dunnett's multiple comparison test comparing the mean of each genotype with the control was performed, finding statistical differences when the *p*-value represented above the brackets is <0,05.

As expected, due to the lower cellularity of the spleen of $Stau1^{-/-}/2^{-/-}$ mice, the number of total B2 B-cells in the tissue is also affected; I observed a 50% reduction (Figure 15C). In a similar magnitude, the average GCB cell number is also reduced without statistical power. Despite the decrease in cell numbers, the proportions of B2 and GCB cells are not altered compared to WT mice (Figure 15B), similar to what I observed for T-cells. Interestingly, B1 B-cells are unaffected in cell numbers and proportion.

Overall, the data collected in $Stau1^{-/-}/2^{-/-}$ mice indicate that the Staufen paralogs are relevant for the thymic T-cell maturation and for regulating the size of B and T cell populations in the spleen. The reduced number of splenocytes could be due to the lack of both Staufen paralogs in B-cells since they have an early predominance in the spleen during development [107]. However, reduced spleen size could also be due to ablation of Staufen 1 and 2 in other cell types responsible for the architecture of this tissue; in this case, one could overcome this effect by restricting Stau1/2 double-deficiency to B cells. To this end, I crossed $Stau2^{F/F}$ $Mb1^{cre/+}$ with $Stau1^{-/-}$ mice, generating animals lacking both Stau paralogs only in the B-cells, while other

cells and tissues are Stau1$^{-/-}$, which does not affect the development of B and T-cells as well as the cellularity of several relevant immune populations in the spleen (Figure 11, 12 and 13).

A deficiency of Staufen paralogs restricted to B-cells shows a trend towards reduced spleen cell numbers

The cellularity of different tissues was analysed in Mb1^{cre} Stau2$^{F/F}$ Stau1$^{-/-}$ mice, focusing on T and B-cells. The results are shown in Figure 16.

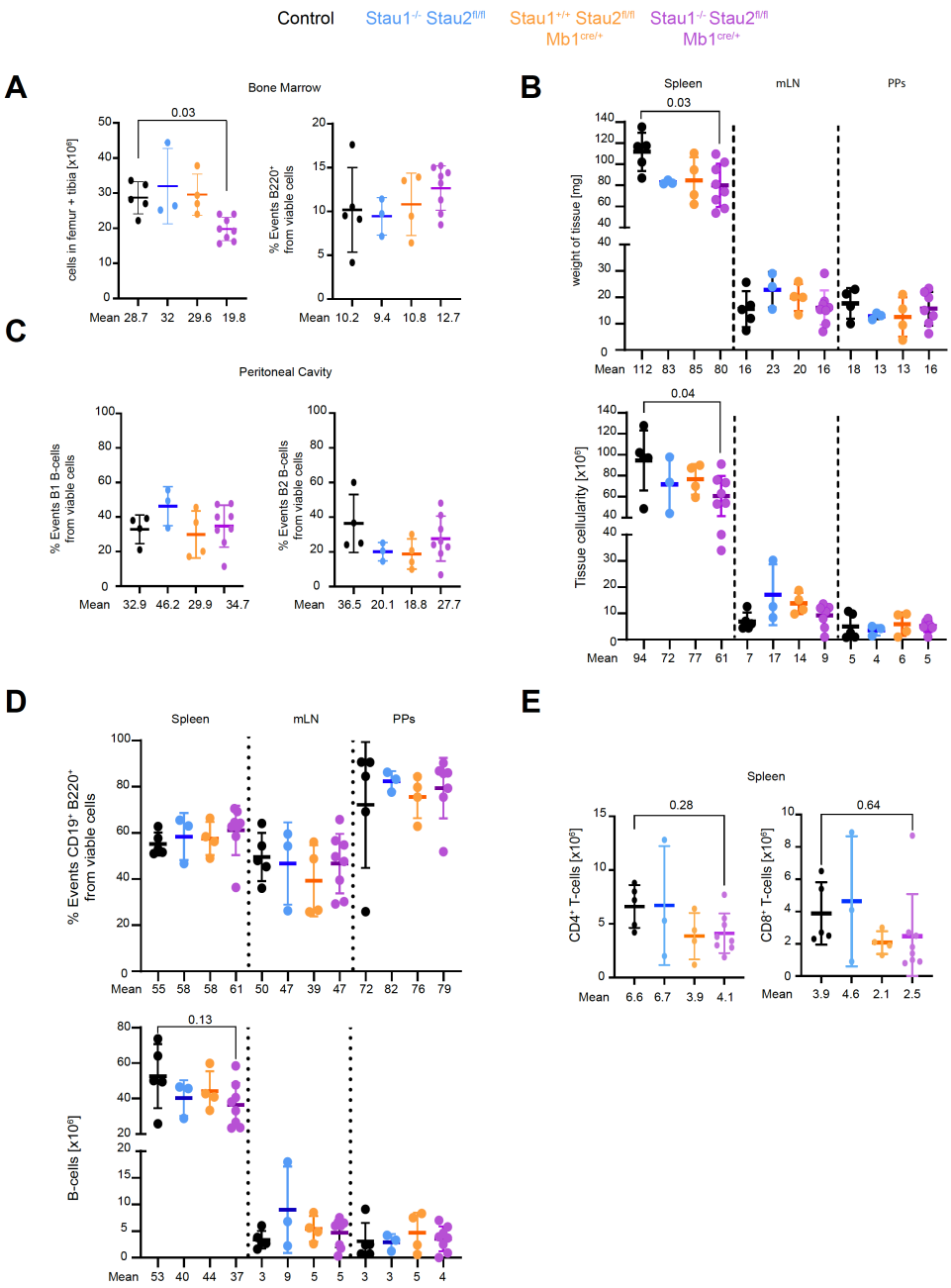

Figure 16: Staufen paralog double deficiency restricted to B-cells affects bone marrow and spleen cellularity. **A**. Scatter plot showing mean ± SD number of bone marrow cells in femur and tibia (left) and proportion of $B220^+$ (right). **B**. Scatter plot showing mean ± SD weight (top) and cellularity (bottom) of the spleen, mLN and PPs. **C**. Scatter plot showing mean ± SD proportion of B1 (left) and B2 (right) B-cells in the peritoneal cavity. **D**. Scatter plot showing mean ± SD proportion (top) and number (bottom) of B-cells in the spleen, mLN and PPs. **E**. Scatter plot showing mean ± SD number of $CD4^+$ (left) and $CD8^+$ (right) T-cells in the spleen. In all graphs, every dot represents the data from one mouse, and the plots include the data collected from 3-4 independent experiments. Moreover, in all scatter plots, a one-way ANOVA t-test with a Dunnett's multiple comparison test comparing the mean of each genotype with the control was performed, finding statistical differences when the *p*-value represented above the brackets is <0,05.

Accentuated to the observed in $Stau1^{-/-}/2^{-/-}$ mice, the lack of both Staufen proteins only in B-cells reduces the total cellularity in the bone marrow from the femur and tibia without affecting the proportion or number of $B220^+$ positive cells in this tissue (Figure 16A). In the periphery, Staufen paralogs expressed in B-cells control the spleen weight and cellularity (Figure 16B); the average spleen weight of $Mb1^{cre}$ $Stau2^{F/F}$ $Stau1^{-/-}$ mice is reduced by 29% compared with their controls (control vs $Mb1^{cre}$ $Stau2^{F/F}$ $Stau1^{-/-}$: 112±18 vs 80±21; *p*-value=0.03). There are 36% fewer cells (94.4±29 vs 61±19; *p*-value=0.04) without affecting the B-cell proportion in this tissue (Figure 16D top). Moreover, similarly to $Stau1^{-/-}/2^{-/-}$, the lower splenic cellularity in $Mb1^{cre}$ $Stau2^{F/F}$ $Stau1^{-/-}$ mice seems to affect both B-cells and T-cells (Figure 16D-bottom, E). However, those cell numbers have no significant statistical differences compared to control mice.

The reduced cellularity that I observed in the bone marrow and spleen in the $Mb1^{cre}$ $Stau2^{F/F}$ $Stau1^{-/-}$ mice is not replicated either in the mLN or in PPs, where the weight and cellularity and both proportion and number of B-cells (Figure 16B) are similar to control mice. Thus, these results suggest the contribution of other Mb1-expressing cells in this phenotype.

Considering that $Stau1^{-/-}/2^{-/-}$ mice have, on average, half of spontaneous GCB cells in the spleen compared with WT mice, I investigated whether this is replicated in the $Mb1^{cre}$ $Stau2^{F/F}$ $Stau1^{-/-}$ mice since these animals also have a trend towards smaller spleens.

$Mb1^{cre}$ $Stau2^{F/F}$ $Stau1^{-/-}$ mice have normal spontaneous GCB cell generation

Considering that the cellularity of both spleen and bone marrow is somewhat reduced in mice lacking both Staufen paralogs only in B-cells, I studied the spontaneous GCB cell generation

in different tissues in a similar fashion to the previous mouse lines to determine whether this population is also affected in these mice. The results are shown in Figure 17.

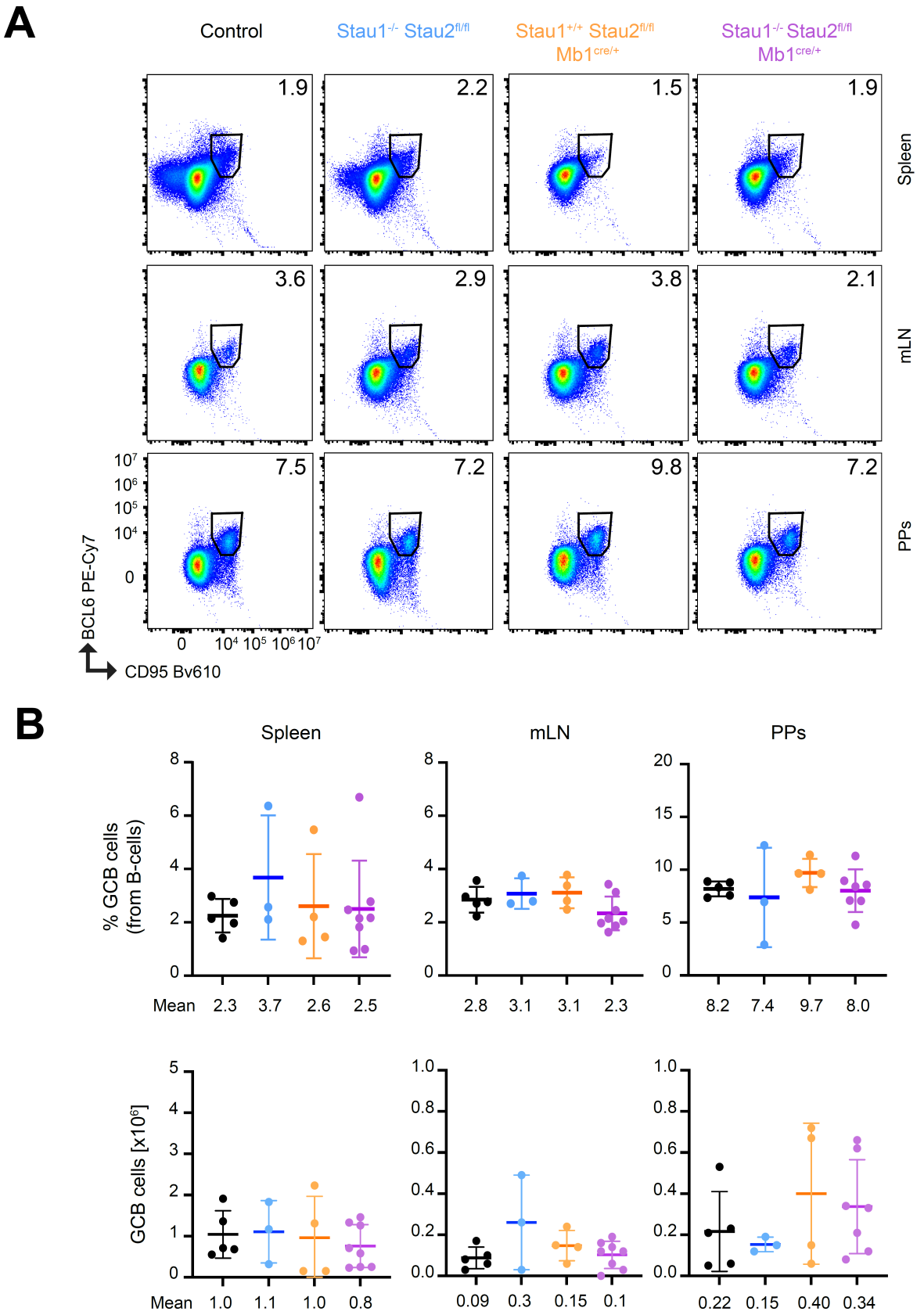

Figure 17: Ablation of both Staufen paralogs restricted to B-cells does not affect the spontaneous generation of GCB cells. A. Representative pseudocolour plots showing GCB cells ($CD95^+BCL6^+$) in the spleen (top), mLN (middle) and PPs (bottom) for mice bearing B-cells sufficient or single and double deficient Stau paralogs. **B**. Scatter plot showing mean ± SD proportion (top) and number (bottom) of GCB cells in the spleen (left), mLN (centre) and PPs. In B, every dot represents the data from one mouse, and the plots include the data collected from 3 independent experiments. In all scatter plots, a one-way ANOVA t-test with a Dunnett's multiple comparison test comparing the mean of each genotype with the control was performed, finding statistical differences when the *p*-value represented above the brackets is <0,05.

Different to my observations in $Stau1^{-/-}/2^{-/-}$ mice, where the number of GCB cells was reduced by half (Figure 15), as were the overall numbers of T and B-cells (Figures 14 and 15), the total number of GCB cells remained unaffected in spleen and lymph nodes of mice deficient for one or both Staufen paralogs in B-cells (Figure 17B). Similarly, the proportions of GCB cells are equivalent in all analysed tissues for all genotypes.

Staufen1 promotes GCB cell expansion upon immunisation with a T-dependent antigen

To study the immune response against a known antigen which could allow me to track both the cellular and humoral immune responses, I decided to immunise mice with the T-cell-dependent antigen 4-Hydroxy-3-nitrophenylacetyl (NP; see methods) coupled to chicken gamma globulin (-CGG) due to its multiple advantages. The murine immune response against this hapten has been extensively described, and it offers the possibility of determining the specific responder B-cells by flow cytometry. Therefore, ten days after NP immunisation, the spleens from mice containing single and double Staufen knockout in B-cells were analysed, as shown in Figure 18.

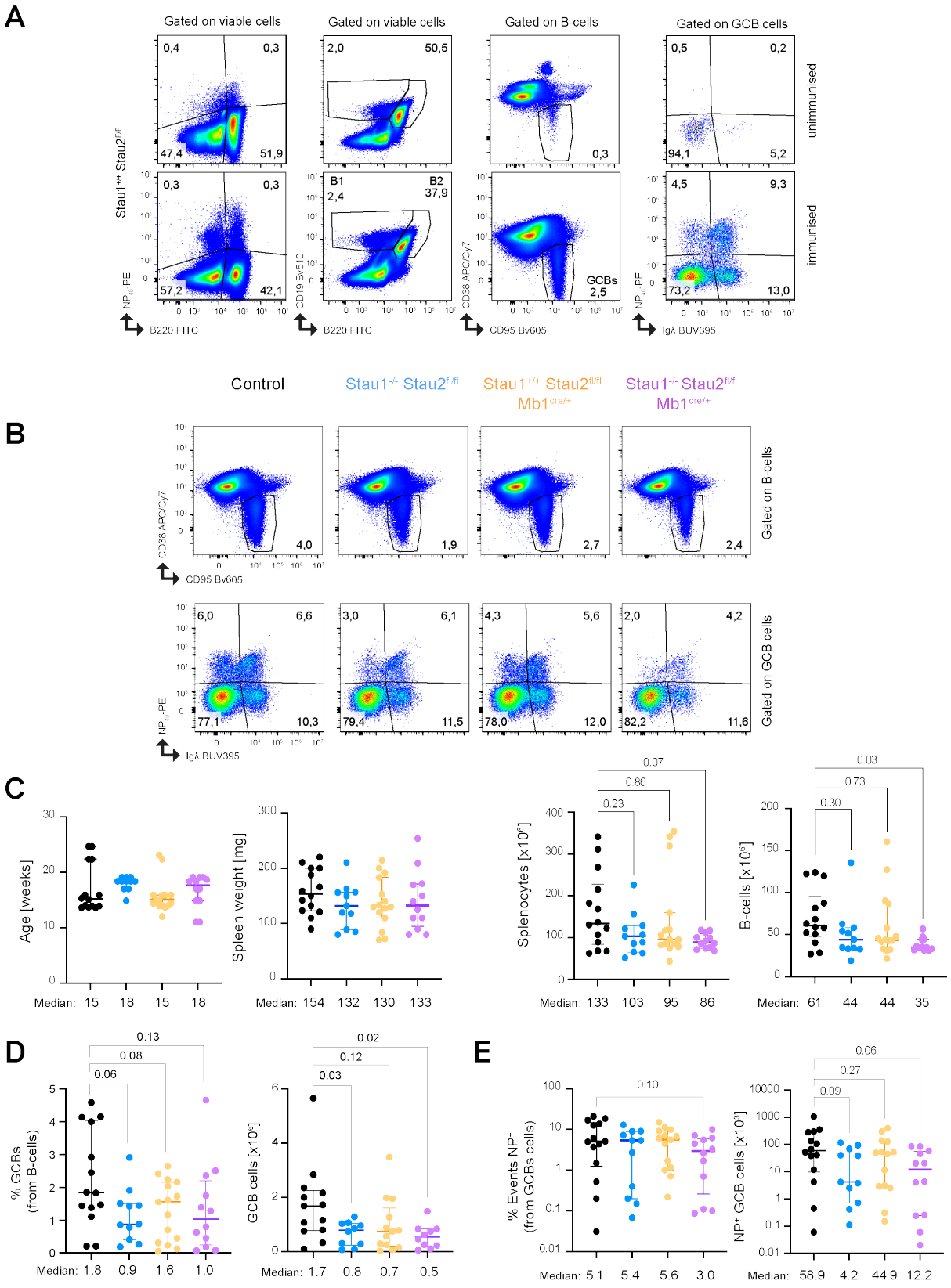

Figure 18: Stau1 promotes GCB cell responses upon immunisation. **A**. Pseudocolour dot plot showing the differences between age-matched control unimmunised (top) and immunised (bottom) mice with the NP hapten. From left to right: total NP^+B220^+ cells; B1 and B2 B-cells; GCB cells; and NP^+ GCB cells. **B**. Pseudocolour dot plots showing the NP-specific GCB B-cells (bottom) in all the genotypes of interest. **C**. From left to right, scatter plot showing median

± interquartile range age of the experimental mice, spleen weight, splenocytes number and B-cell number. **D**. Scatter plot showing median ± interquartile proportion (left) and number (right) of total GCB cells (identified as $CD38^{-}CD95^{+}$ from B2 B-cells). **E**. Scatter plot showing median ± interquartile proportion (left) and number (right) of total NP-responders GCB cells considering both $Ig\lambda^{+}$ and $Ig\lambda^{-}$ cells. In C-E, every dot represents the data from one mouse, and the plots include the data collected from 3 independent experiments. In all scatter plots, a one-way ANOVA t-test with a Dunnett's multiple comparison test comparing the mean of each genotype with the control was performed, finding statistical differences when the *p*-value represented above the brackets is <0,05.

Similar to naïve mice, I observed no differences in the B-cell proportions in immunised mice of the different genotypes. The slight differences in spleen weight and splenocyte numbers previously observed at steady state (Figure 16) were also observed in immunised mice (Figure 18C). The number of splenocytes is expected to increase upon vaccination, as reported before [108]. In my experiments, spleen cell numbers increased by 66% ($9x10^{7}$ vs $1.5x10^{8}$ cells) in control mice but only 43% in $Mb1^{cre}$ $Stau2^{F/F}$ $Stau1^{-/-}$ mice only ($6x10^{7}$ vs $8.6x10^{7}$ cells).

In the GC compartment, I detected that Stau1 promotes the development of GCB cells in response to immunisation since Stau1-deficient mice have a lower proportion and number of these cells among the B-cells. This phenotype is also observed in $Mb1^{cre}$ $Stau2^{F/F}$ $Stau1^{-/-}$ mice with significantly fewer GCB cells upon immunisation than control animals. Interestingly, in mice carrying Stau2-deficient B-cells, the GCB proportion is unaffected. Still, the median number of these cells is quite similar to Stau1-deficient and $Mb1^{cre}$ $Stau2^{F/F}$ $Stau1^{-/-}$ mice, which may also be given for ~30% fewer B-cells in this genotype compared to control animals, reinforcing the suggestion that Stau paralogs may control B-cell expansion upon immunisation.

The PE fluorophore-coupled NP, in combination with Igλ, was used to identify the antigen-specific responder B-cells (Figure 18A). Thanks to this procedure, I identified the GCB cells generated upon the immunisation in all studied genotypes (Figure 18B). I observed that the lack of Staufen paralogs in B cells has no statistically significant impact on the proportion of the number of NP-responder GCB cells ($B220^{+}CD19^{+}CD38^{-}CD95^{+}NP^{+}$; Figure 18E). However, there was a clear trend towards reduction of NP-specific GCB cells in Stau1-deficient and B cell-specific Stau1/2-deficient mice, as their median cell numbers were 14 and 5-fold reduced, respectively.

Altogether, the analysis of the immunised mice showed that Stau paralogs promote the expansion of B-cells and, consequently, GCBs. Moreover, Stau1 promote NP-specific GCB cell expansion and/or maintenance at the peak of a T-cell mediated B-cell response.

Staufen paralogs promote the GCBs cellularity at late stages after immunisation

In the well-characterised NP-immunisation model, it has been described that the germinal centres reach their maximum size by day 12-14 and persist until day 16 post-immunization [109-111]. Simultaneously to decreasing GCB cells in the spleen by day 14, IgG1 and IgM plasma cells ($CD138^{+}B220^{lo}$) slowly start accumulating in the bone marrow [112, 113]. These cells are derived either from GCB cells or the initial expansion of the antibody-forming cells upon immunisation [114]. Therefore, to determine whether the differences observed at day 10 after immunisation (peak in our mouse housing conditions) remain longer, I analysed the mice 28 days after immunisation, and the results are presented in Figure 19.

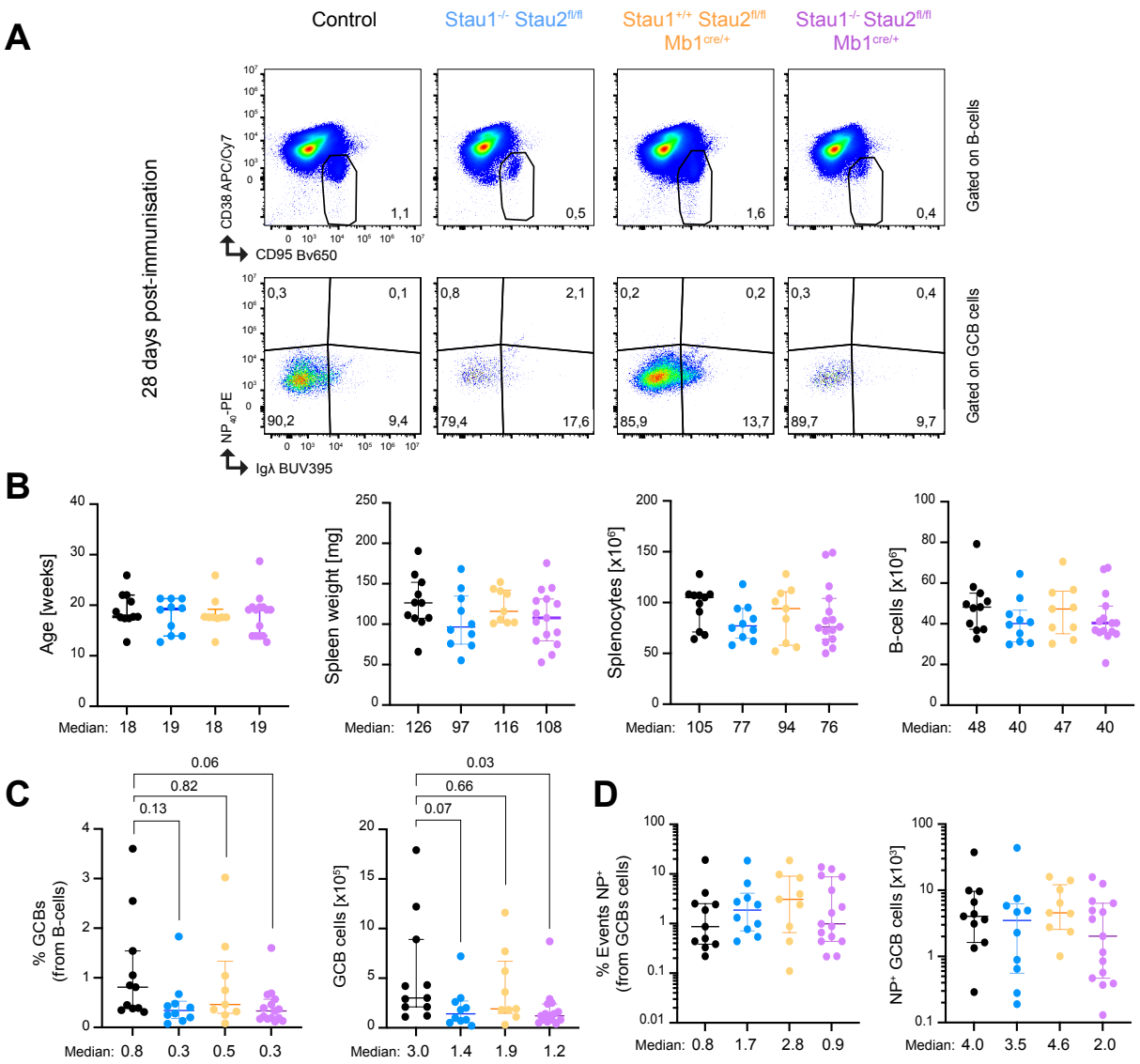

Figure 19: Staufen paralogs promote GCBs cellularity upon immunisation. **A**. Pseudocolour dot plots showing the NP-specific GCB B-cells (bottom) in all the genotypes of interest. **B**. From left to right, scatter plot showing median ± interquartile range age of the experimental mice, spleen weight, splenocytes number, B-cell proportion and number. **C**. Scatter plot showing median ± interquartile proportion (left) and number (right) of total GCB cells (identified as $CD38^{-}CD95^{+}$ from B2 B-cells). **D**. Scatter plot showing median ± interquartile proportion (left) and number (right) of total NP-responders GCB cells. In B-D, every dot represents the data from one mouse, and the graphs include the data from four independent experiments. In all scatter plots, a one-way ANOVA t-test with a Dunnett's multiple comparison test comparing the mean of each genotype with the control was performed, finding statistical differences between the genotypes when the number above the bars is <0,05.

Unlike the situation on day 10 after immunisation, I observed no differences in the spleen weight and number of splenocytes, neither in proportion nor in the number of B-cells at 28 days post-immunisation. In other words, the B-cell expansion at the peak of the immune

response seems to be deficient in Stau1$^{-/-}$ and Mb1^{cre} Stau2$^{F/F}$ Stau1$^{-/-}$ mice, while at later time-points there was no difference between the genotypes.

Four weeks after immunisation, I observed slight differences in the GCB cell compartment. Mice lacking Stau1 have a reduced proportion (2,6x) and number (2,1x) of GCB cells compared with the control mice. However, none of these differences reached statistical significance (Figure 19C). This differs from the case of mice bearing Stau1/2-deficient B-cells, whose number of GCB cells remains statistically significantly lower than control mice, similar to the situation at day 10 post-immunisation. Analysing the specific NP response, I observed that it is generally contracted in the spleen compared to ten days after immunisation, as previously reported [112, 113]. Moreover, I observed no significant differences in the frequency or number of NP-GCB cells among the genotypes (Figure 19D), although Mb1^{cre} Stau2$^{F/F}$ Stau1$^{-/-}$ mice have almost half of these cells.

Staufen paralogs modulate key aspects of the antigen-specific humoral response

To evaluate the impact of Stau paralog deficiency on antibody production and affinity maturation, I evaluated the humoral immune response in mice of the different genotypes by ELISA. The results are presented in Figures 20 and 21.

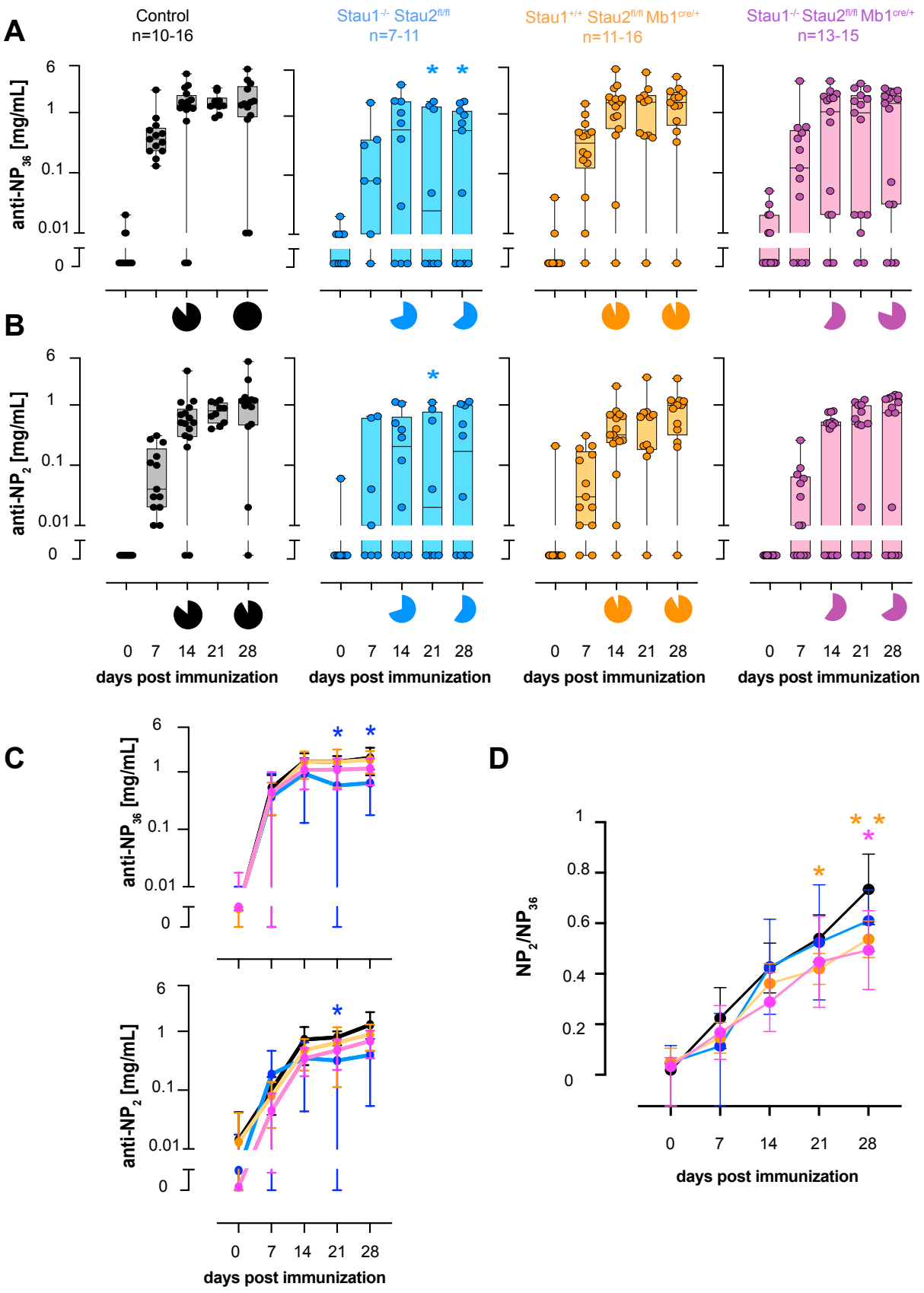
A
Control
n=10-16
Stau1-/- Stau2fl/fl
n=7-11
Stau1+/+ Stau2fl/fl Mb1cre/+
n=11-16
Stau1-/- Stau2fl/fl Mb1cre/+
n=13-15
anti-NP36 [mg/mL]
B
anti-NP2 [mg/mL]
0 7 14 21 28
days post immunization
C
anti-NP36 [mg/mL]
anti-NP2 [mg/mL]
D
NP2/NP36

Figure 20: Staufen paralogs play a different role in the humoral response against NP. **A-B**. Box and whiskers plots showing the blood serum titer of total (top) and high-affinity (bottom) IgG1 antibodies against NP antigen in a logarithmic scale. Every day contains the accumulated data of 7-16 mice per genotype, as specified at the top of the figure. **C**. Summary line plots in logarithmic scale depicting the mean titer with 95% CI for total (top) and high-affinity (bottom) anti-NP IgG1 antibodies. **D**. Summary line graph plotting the mean NP_2/NP_{36} ratio (reflecting immunoglobulin affinity to NP) with 95% CI on every measured day, considering mice with anti-NP IgG1 titer > 0,01 mg/mL. A and B included a pie chart on days 14 and 28, showing the proportion of mice with an IgG1 titer > 0,01 mg/mL. In A, B, and C, for graphical purposes, the values equal to 0 were plotted as 10^{-7}, and Y=0 was added to the plots. In every time point, a one-way ANOVA t-test with Dunnett's multiple comparison tests comparing the mean of each genotype with the control was performed, finding statistical differences with * *p*-value <0,05 and ** *p*-value < 0,01.

Despite generally reduced GCB cell numbers upon immunisation, $Mb1^{cre}$ $Stau2^{F/F}$ $Stau1^{-/-}$ mice develop a similar humoral response against NP as the control mice (Figure 20). The total (NP_{36}) and the high affinity (NP_2) IgG1 antibodies titer in the blood are similar between the control and the B cell-specific Stau1/2-deficient mice in all measurements, observing a gradually increasing affinity maturation over time in both genotypes. However, the anti-NP affinity is, on average, lower from day 14 post-immunisation onwards, being statistically lower at day 28 post-immunisation (0,7 vs 0,4; *p*-value=0,02).

Regarding Stau2, consistent with $Mb1^{cre}$ $Stau2^{F/F}$ mice containing similar numbers and proportions of NP-specific GCBs on day 10 and 28 post-immunisation as control mice, they produce similar anti-NP IgG1 during the time course of the immunisation, suggesting that Stau2-deficiency is dispensable for humoral responses to NP. Regarding affinity maturation, mice bearing Stau2-deficient B-cells have a lower ratio of NP_2/NP_{36} for IgG1 from day 14 post-immunisation onwards, reaching statistical significance at day 21 (0,5 vs 0,4; *p*-value=0,02) and 28 (0,7 vs 0,5; *p*-value=0,009) post-immunisation.

On the other hand, $Stau1^{-/-}$ mice, which also showed a reduced GC compartment at day 10 and 28 after immunisation like $Mb1^{cre}$ $Stau2^{F/F}$ $Stau1^{-/-}$ mice, have reduced NP-specific IgG1 titers both in total and high-affinity anti-NP IgG1 antibodies compared with the control mice, starting at day 21 after immunisation until the end of the experiment. At day 21 post-immunisation, control mice have an anti-NP_2 IgG1 titer of 0,8 mg/mL, while Stau1-deficient mice have 0,3 mg/mL of anti-NP_2 IgG1 (*p*-value=0,02). This is correlated with total anti-NP IgG1, whose titer in control animals amounts to 1,5 mg/mL, while in $Stau1^{-/-}$ mice, it is 0,6 mg/mL (*p*-value=0,01). On day 28 after immunisation, the titer of high-affinity IgG1 against NP is 1,3 mg/mL in control animals, while in Stau1-deficient mice, it is 0,4 mg/mL (*p*-value=0,06).

That difference is also mirrored in the total titer of IgG1 against NP, which is 1,8 mg/mL in control and 0,6 mg/mL in Stau1$^{-/-}$ mice (*p*-value=0,04). Overall, at day 28 post-immunisation, total and high-affinity antibodies in Stau1$^{-/-}$ mice are ~3-fold reduced. Of note, there might be a contribution of the lower percentage of mice with a detectable antigen-specific immunoglobulin titer in Stau1$^{-/-}$ compared to control animals, which, on day 28 post-immunisation, is 64 and 100%, respectively. Interestingly, among the responder animals, meaning those with a detectable NP-specific IgG1 titer, the affinity maturation does not seem to be impacted by the loss of Stau1 since the ratio between NP_2/NP_{36} is similar among the genotypes. These results suggest that Stau1 might promote the specific humoral response by PC differentiation or viability.

Altogether, my results suggest that the Staufen paralogs do not play prominent critical roles in the development or differentiation of B cells at the steady state. However, upon immunisation, Stau2 might promote affinity maturation since mice carrying Stau2-deficient B-cell (sufficient or deficient for Stau1) have a lower NP_2/NP_{36} ratio. On the other hand, Stau1 promotes the expansion of the overall GCB cell compartment. Since Stau1-deficient mice have a reduced GCB cell population and a lower IgG1 antibody titer against the delivered antigen. Interestingly, the coordination between both Staufen paralogs might have a role in the expansion or maintenance of both total and NP-specific GCBs upon immunisation since Mb1^{cre} Stau2$^{F/F}$ Stau1$^{-/-}$ mice have a significantly lower number of those cells at day 10 and 28 post-immunisation. Counterintuitively, these differences are not mirrored in the blood titer of NP-specific IgG1 or IgM, which are similar to control animals. These results suggest an intricate regulation between both paralogs in B-cells.

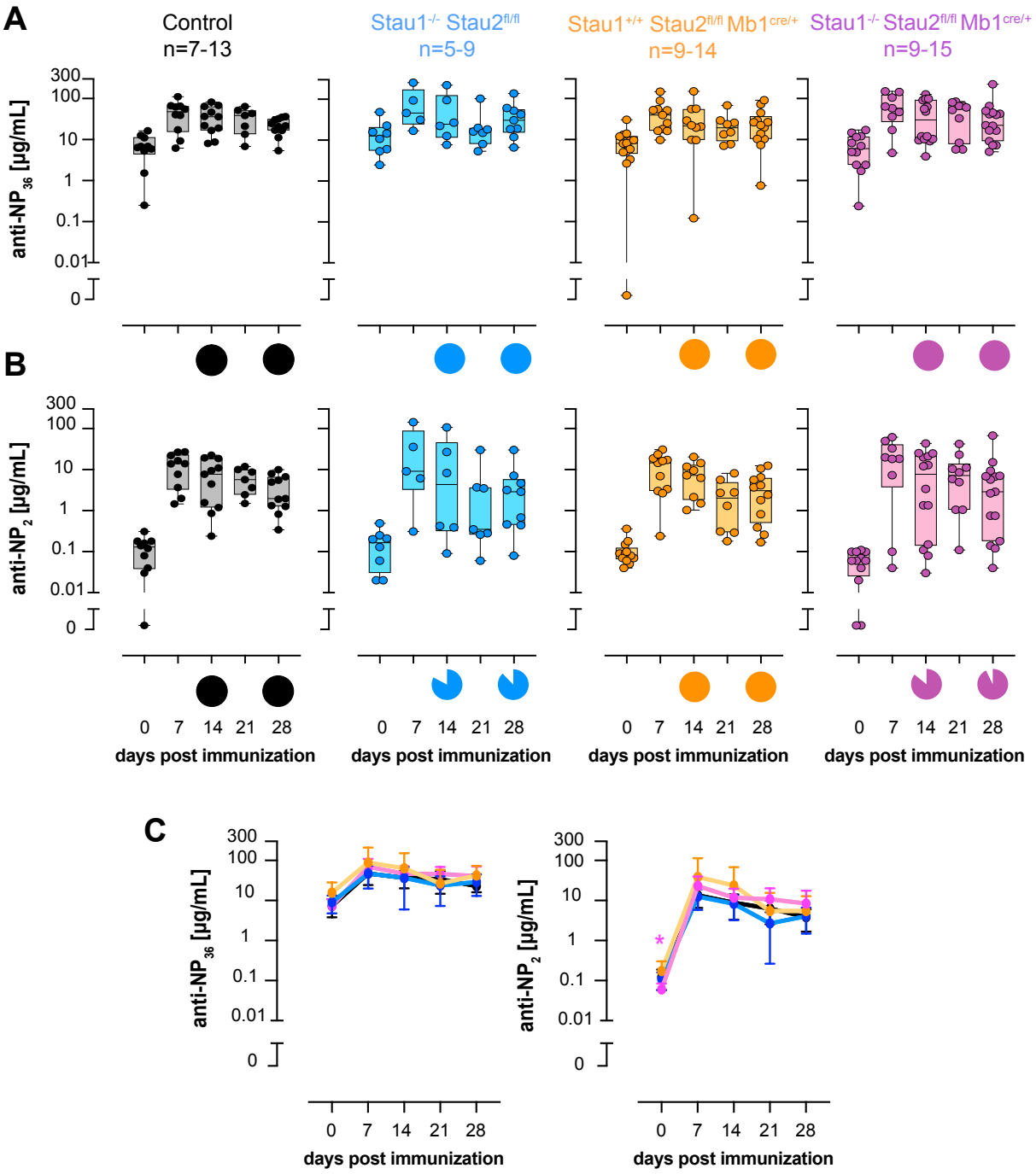

Figure 21: Staufen paralogs are not required for antigen-specific IgM humoral responses. **A-B**. Box and whiskers plots showing the blood serum titers of total (top) and high-affinity (bottom) IgM antibodies against NP antigen in a logarithmic scale. Every day contains the accumulated data of 7-15 mice per genotype, as specified at the top of the figure. **C**. Summary line plots in logarithmic scale depicting the mean titers with 95% CI for total (left) and high-affinity (right) anti-NP IgG1 antibodies. A and B included a pie chart on days 14 and 28, showing the proportion of mice with an IgM titer > 0,1 µg/mL. In A, B, and C, for graphical purposes, the values equal to 0 were plotted as 10^{-7}, and Y=0 was added to the plots. In every time point, a one-way ANOVA t-test with Dunnett's multiple comparison tests comparing the mean of each genotype with the control was performed, finding statistical differences with * *p*-value <0,05.

Unlike the IgG1 titer, which peaked at day 28 post-immunisation, the concentration of anti-NP IgM had the highest value at day 7 post-immunisation in all of the genotypes, which slowly decreased over time. However, no differences were found between the total and high-affinity anti-NP IgM antibodies or the ratio between them when comparing the target genotypes. This suggests that Staufen paralogs are irrelevant in the humoral IgM response.

To investigate the molecular functions of the Staufen paralogs in B cells and explain the phenotypes observed in knockout mice, I performed simultaneous analyses in the A20 cell line, which recapitulates some of the features of GCB cells. In this cell line, I could use several molecular techniques to determine a set of Stau-targeted mRNAs hinting at the roles of Stau1 and Stau2 in GCB cells. All the work performed in this cell line model is presented in the next section of the results.

The A20 cell line reflects aspects of germinal centre B-cells

Twelve previously described or generated B cell lines from us and others were cultured (see materials and methods) for bulk RNA sequencing to analyse their transcriptomes (Figure 22).

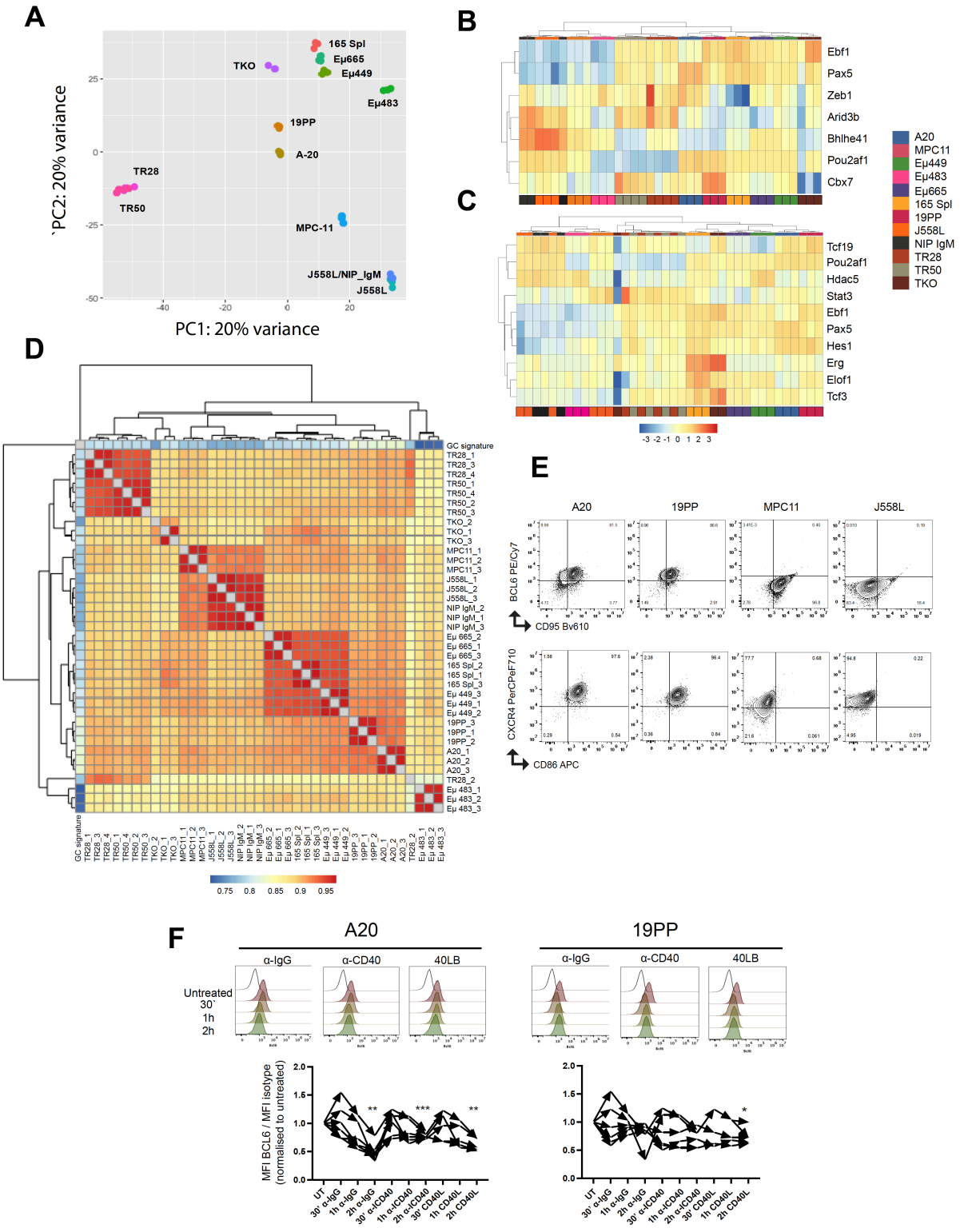

Figure 22: The A20 cell line recapitulates classical features of GCB cells. **A**. Principal component analysis (PCA) plot, generated using each cell line's top 2000 transcribed genes. **B**. Heatmap showing the z-score (row-wise) of the transcription of seven genes related to the B1 B-cells signature. **C**. Heatmap showing the z-score (row-wise) of the transcription of ten genes related to the pre/pro-B-cells signature. **D**. Heatmap showing the Pearson coefficient between the matched genes of primary GCB cells and the cell lines. **E**. Representative contour plot analysing classical markers of GCB cells in several cell lines. **F**. Representative histograms (top) and arrow plots (bottom) showing the BCL6 expression upon different stimuli in A20 (left) and 19PP (right) cells. The line with no fill shows the isotype staining. In F, the accumulated data from 5-6 experiments are shown together, and the mean expression of BCL6 in all conditions was analysed with paired Mixed-effects analyses with multiple comparisons where * represents *p*-value<0,05, ** p-value<0,01 and *** *p*-value < 0,001.

The transcriptome of all cell lines was analysed using DESEq2 in R. Focussing on the top 2000 transcribed genes in these cell lines; I observed that the plasma cell-like lines MPC11, J558L and its derivative NIP-IgM J558L are grouped close to each other (Figure 22A). Therefore, to decipher whether the other cell lines could be functionally grouped, I took advantage of the genetic signatures of immune populations detailed in immgen [111]. Among the differentially transcribed genes, I detected 7 out of 12 B1 B-cell signature gene regulators [B1 module (immgen.org)] in the whole transcriptome dataset. In particular, 6 out 7 (Ebf1, Pax5, Zeb1, Ari3b, Bhlhe41, Pou2af1 and Cbx7) were highly transcribed in TR28 and/or TR50 (Figure 20B) matching with the constitutively active IKK2ca expressing B1 cell origin of the lines (unpublished data). Similarly, 10 out of 11 pre/pro-B-cells regulators [Pre-B-cells (immgen.org)] were found among the differentially transcribed genes and were highly transcribed in 165 Spl, TKO, Eμ665 and Eμ449 (Figure 22C), which grouped when using these genes to War.D2 clustering, indicating a more immature phenotype of these cell lines.

To determine the transcriptional proximity of the cell lines with GCB cells, I cross-referenced the matched genes between the transcriptome of primary GCBs [115] and our dataset, finding 13282 transcripts. Then, those genes were compared between primary GCB cells and cell lines and the Pearson coefficient was calculated. The Pearson coefficient was generally elevated between GCB cells and all cell lines (Figure 22D), presumably due to the high proliferation of both GCB cells and cell lines. However, the highest Pearson coefficient (>0.8) was observed in A20 and 19 PP cells, suggesting a similarity between them and GCB cells. Since it was previously reported that A20 cells express the classical GCB cell markers BCL6 and CD95 [116], I checked those also in 19PPs, observing a similar phenotype between A20 and 19PP (Figure 22E). In agreement with their plasma cell-like phenotype, those markers were not expressed in MPC11 nor J558L lines, which also express CXCR4, which is typical for plasma cells.

Regarding the distinctive transcription factor of GCB cells, the expression of BCL6 was assessed upon anti-IgG or CD40-stimulation treatment since it has been suggested that BCR activation and CD40 signalling downregulate BCL6 both in primary GCB cells and GCB-like cell lines [117, 118]. As reported previously [116], I observed that after 2 hours of treatment with either α-IgG, α-CD40 or with other cell lines expressing the ligand of CD40 (40LB), the expression of BCL6 was reduced by half in A20 cells, while in 19PPs, this was only observed co-culturing the cells with 40LB cells (Figure 22F). Therefore, despite the genetic signatures of 19PP cells to GCB cells, I focussed on the following experiments studying the Staufen paralogs in GCB-like cells on the A20 cell line.

Staufen 2 deficiency affects the transcriptome of A20 cells

I generated between 4-9 single-cell-derived WT, single and double Staufen knockout A20 clones by electroporation with sgRNA/Cas9 RNPs (as described in materials and methods) and validated them by Western blot. To identify Stau1 and Stau2-regulated mRNAs in A20 cells, the transcriptomes of these cell clones were determined by bulk RNA sequencing, and the results are shown in Figure 23.

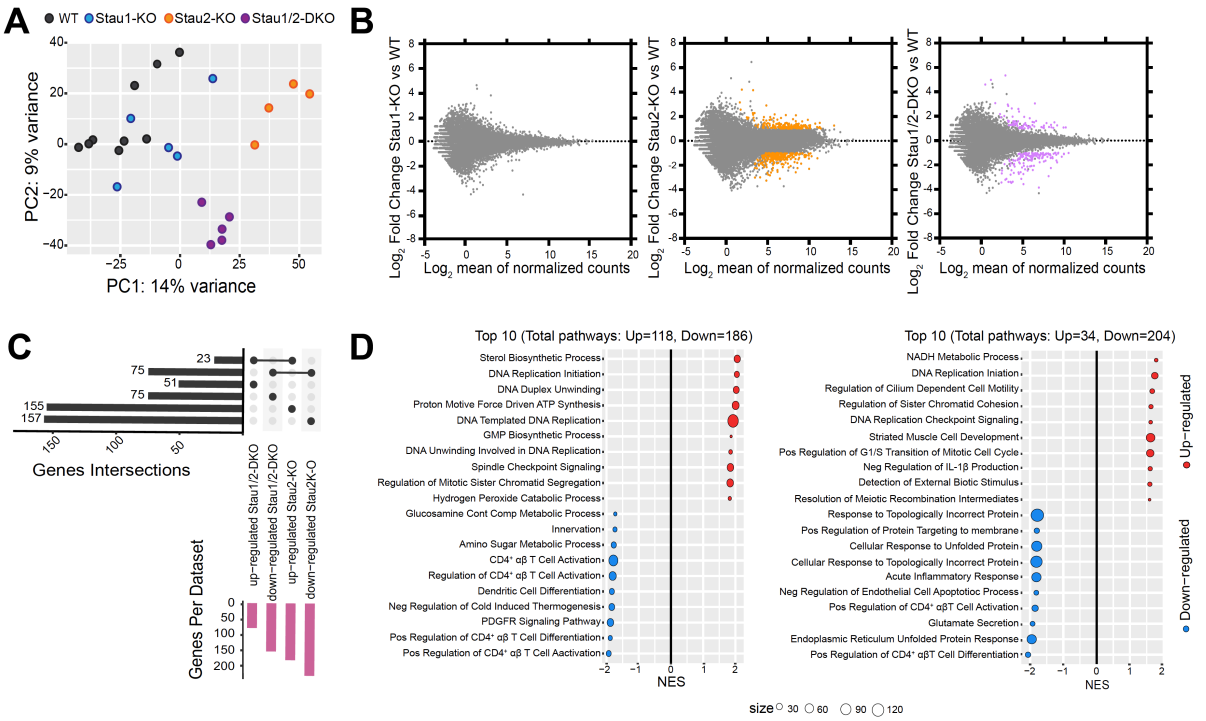

Figure 23: Stau2 regulates the transcriptome of A20 cells. **A**. A PCA plot was generated analysing all the detected transcripts in the RNAseq of WT and Stau single and double KO A20 cells. **B**. MA plots showing all detected transcripts (grey) and the differentially expressed genes (DEG; in colour) comparing the transcriptome of WT with Stau1-KO (left), Stau2-KO (centre) and Stau1/2-DKO (right) A20 cells. **C**. Up-set plot showing the intersections of differentially expressed genes (DEG) between Stau2-KO and Stau1/2-DKO A20 cells. **D**. Enrichment analysis of the DEG for Stau2-KO (left) and Stau1/2-DKO (right) A20 cells.

The PCA plot from the transcriptomes of all genotypes shows a close relationship between WT and Stau1 knockout A20 clones diverging from the Stau2-KO and Stau1/2-DKO clones (Figure 23A). This might be due to the similarity of the Stau1-KO and WT A20 cell transcriptomes, given the absence of differentially expressed genes (with *p*-value <0,01 and |Log2FC| >1) between those genotypes, as shown in the MA plots (Figure 23B). A different picture emerges for the Stau2-KO and Stau1/2-DKO A20 cells, which have 410 and 224 differentially expressed genes (DEG) compared with WT cells, respectively. Interestingly, I identified only 98 common DEG between Stau2-KO and Stau1/2-DKO clones (Figure 23C).

I determined the biological processes that are affected by Stau2 and Staufen1/2 deficiency in A20 cells by genes set enrichment analysis using the "*fast gene set enrichment analysis"* package in R. As is shown with the normalised enrichment score (NES), genes related to the DNA damage control and cell cycle were upregulated both in Stau2-KO and Stau1/2-DKO cells. They suggest a control of Stau2 over these processes, as mentioned in the introduction. In contrast, genes related to cell activation and metabolism are downregulated (Figure 23D). To validate, substantiate and extend our observed effects of Staufen protein deficiency on mRNA expression in A20 cells, I quantified the proteomes of these clones by mass spectrometry.

Staufen paralogs regulate the translation of relevant GC-related genes

Considering that RBPs can control translation and thereby affect protein levels without affecting the respective RNA amounts, I quantified the proteomes of the single and double Stau-deficient A20 cells by mass spectrometry-based proteomics (Figure 24).

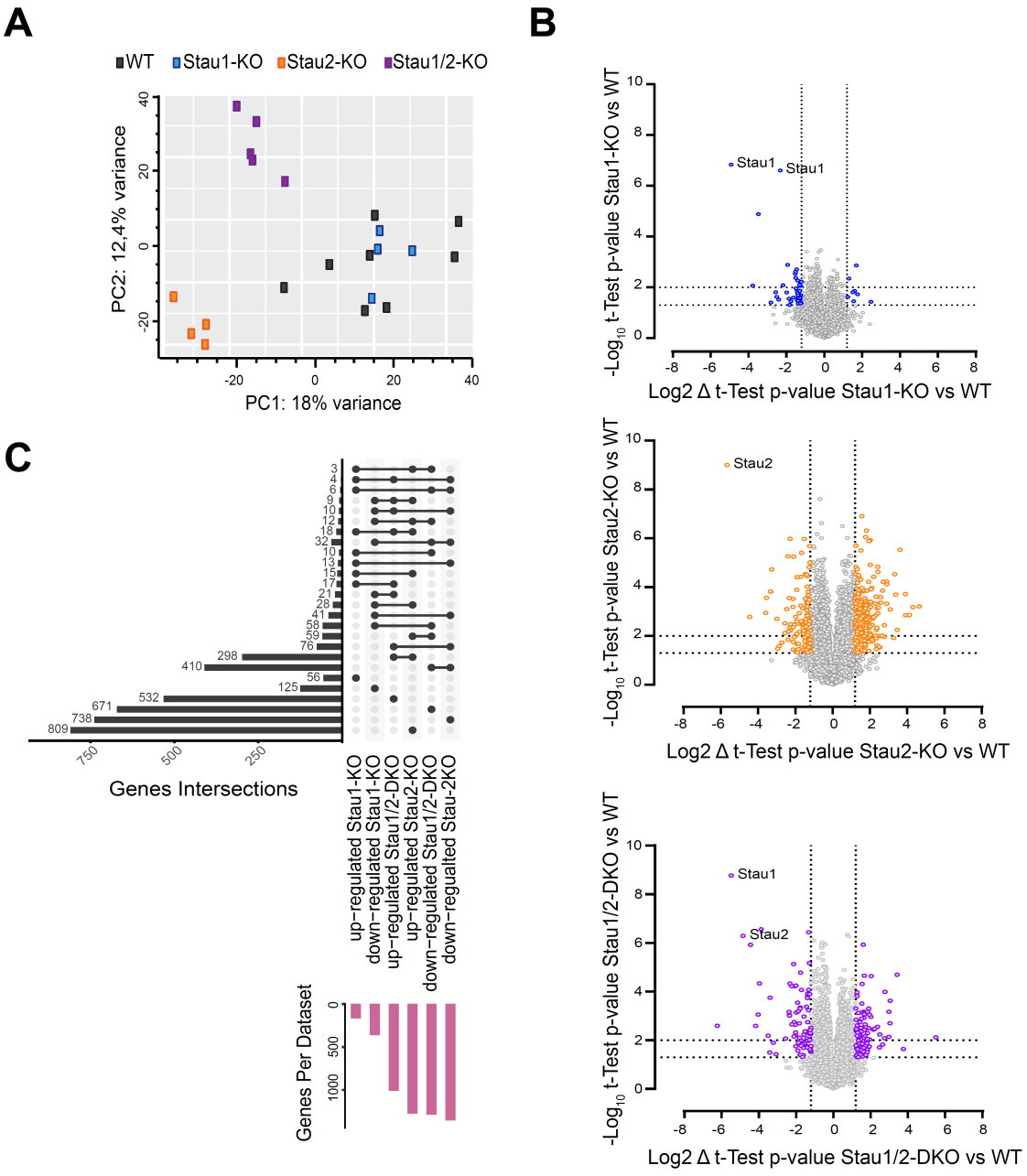

Figure 24: Staufen paralogs regulate the proteome of A20 cells. **A**. A PCA plot was generated analysing all the detected proteins in the proteome of WT and Stau single and double KO A20 cells. **B**. Volcano plots showing all detected proteins (grey) and the differentially expressed proteins (DEP; in colour) comparing the proteome of WT with Stau1-KO (top), Stau2-KO (middle) and Stau1/2-DKO (bottom) A20 cells. The first dotted line at y=1.3 represents a *p*-value of 0.05, while the dotted line at y=2 represents a *p*-value of 0.01. **C**. Up-set plot showing the intersections of DEP between Stau1-KO, Stau2-KO and Stau1/2-DKO A20 cells.

In the proteome analysis, as in the transcriptome, Stau1-KO and WT A20 cells grouped closely in the PCA plot, diverging from Stau2-KO and Stau1/2-DKO cells (Figure 24A). I found 54 highly differentially expressed proteins (hDEP; *p*-value<0,05 and |FC| >2,4) between Stau1-KO and WT cells. 343 hDEP were identified in Stau2-KO clones and 180 in Stau1/2-DKO A20s compared with the WT clones (Figure 24B). Unexpectedly, considering all the DEP among all the genotypes by the *p*-value (y > 1,3 in plots) I detected only 18 up-regulated and 32 down-regulated proteins common to all genotypes (Figure 24C), which represent 8,5% of DEG in Stau1-KO, 1,9% in Stau2-KO and 2,5% in Stau1/2-DKO A20 cells, suggesting the lack of either or both paralogs affects differently the A20 cells.

As the most relevant effects regarding B cell biology were found in Stau1-deficient mice, I focused on determining which proteins related to GC biology could be regulated by Stau1. To this end, I first compiled a GCB cell proteome signature, selecting the genes with an FC > 2,4 and *p*-value< 0,001 among the DEP between GCB cells and mantle zone B cells from Figure 3. I then cross-referenced this list with the proteome of the A20 cell lines (Figure 24D), finding that relevant proteins are being directly or indirectly controlled by one or both Staufen proteins, as shown in Figure 25.

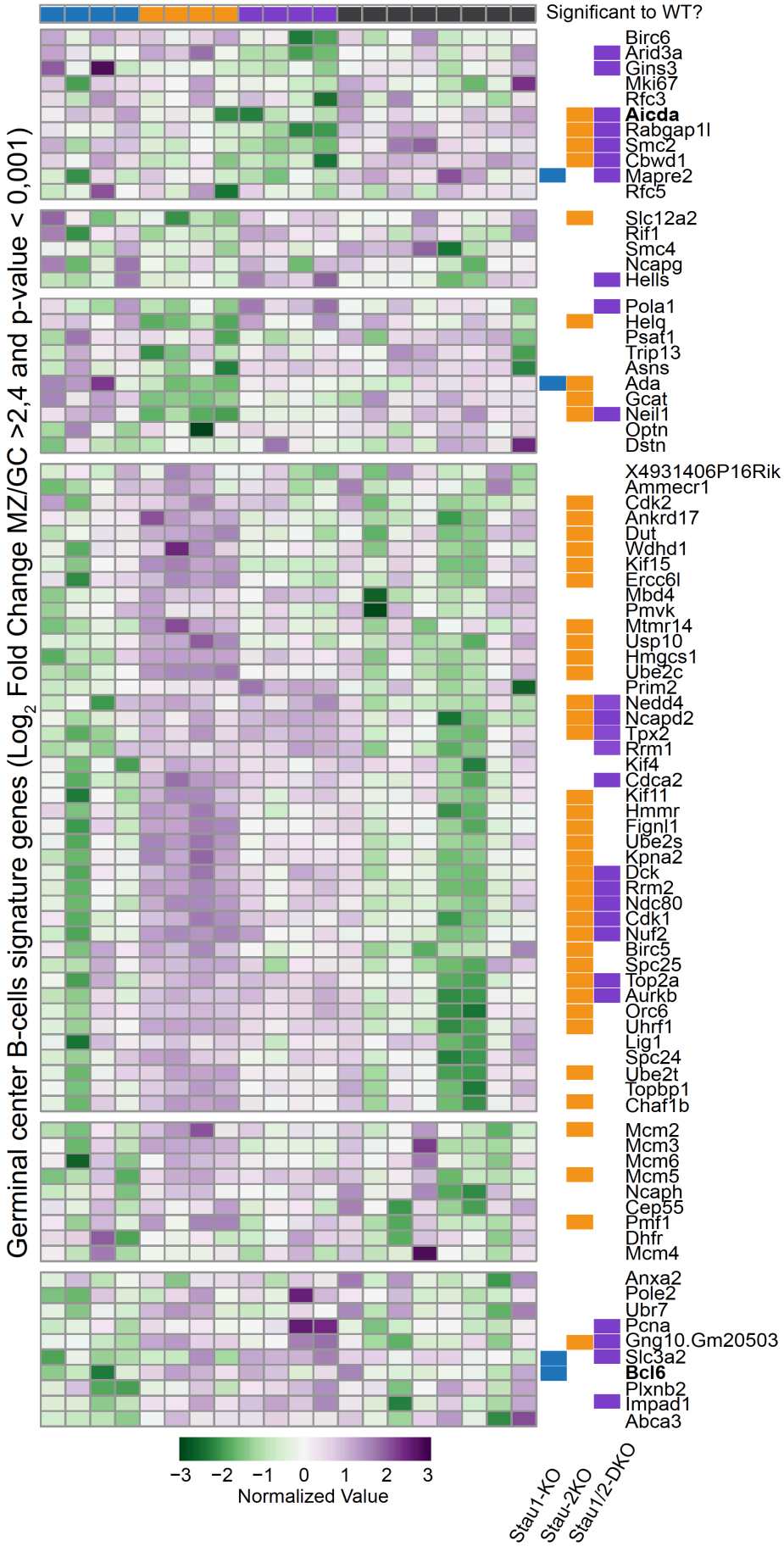
Significant to WT?
Germinal center B-cells signature genes (Log2 Fold Change MZ/GC >2,4 and p-value < 0,001)
Birc6
Arid3a
Gins3
Mki67
Rfc3
Aicda
Rabgap1l
Smc2
Cbwd1
Mapre2
Rfc5
Slc12a2
Rif1
Smc4
Ncapg
Hells
Pola1
Helq
Psat1
Trip13
Asns
Ada
Gcat
Neil1
Optn
Dstn
X4931406P16Rik
Ammecr1
Cdk2
Ankrd17
Dut
Wdhd1
Kif15
Ercc6l
Mbd4
Pmvk
Mtmr14
Usp10
Hmgcs1
Ube2c
Prim2
Nedd4
Ncapd2
Tpx2
Rrm1
Kif4
Cdca2
Kif11
Hmmr
Fignl1
Ube2s
Kpna2
Dck
Rrm2
Ndc80
Cdk1
Nuf2
Birc5
Spc25
Top2a
Aurkb
Orc6
Uhrf1
Lig1
Spc24
Ube2t
Topbp1
Chaf1b
Mcm2
Mcm3
Mcm6
Mcm5
Ncaph
Cep55
Pmf1
Dhfr
Mcm4
Anxa2
Pole2
Ubr7
Pcna
Gng10.Gm20503
Slc3a2
Bcl6
Plxnb2
Impad1
Abca3
−3 −2 −1 0 1 2 3
Normalized Value
Stau1-KO
Stau-2KO
Stau1/2-DKO

Figure 25: Staufen RBP deficiency affects proteins relevant to GC biology. Heat plot showing the z-score of normalised proteome LFQ values of a specific gene setlist. Every square represents the value of a different A20 cell clone WT (black), Stau1-KO (blue), Stau2-KO (orange) and Stau1/2-DKO (purple). When a gene was found statistically significantly different in any of the genotypes of A20 cells compared to the WT, a coloured rectangle was drawn with the respective colours.

However, due to the low impact in the proteome of A20 cells, only a few GC-related proteins were found to be regulated by Stau1. In detail, Mapre2, Slc3a2 and Bcl6 are downregulated, while Ada is upregulated in Stau1-KO A20 cells. On the other hand, the previously mentioned GCB cell-relevant proteins Aicda, Helq and Neil1, which are relevant for GCB cell generation upon immunisation [119], are down-regulated in Stau2-KO A20s. Furthermore, the cell cycle-related proteins Cdk1 and Cdk2 are amongst many other up-regulated proteins. Aicda is also downregulated in Stau1/2-DKO A20s, while Hells and the cell cycle-related Cdk1 and Cdca2 are up-regulated (Figure 25).

Regarding the DEP mentioned above, the downregulation of Bcl6 could contribute to the restricted GC expansion of Stau1-deficient mice upon immunisation since this transcriptional modulator is essential for maintaining the GCB cells. Upon immunisation, the lower affinity of NP-specific IgG antibodies in Stau2-deficient mice might relate to the downregulation of AID, which is essential for somatic hypermutation. However, these hypotheses must be validated by various independent approaches in cell lines and primary cells. My results suggest, considering the differences in the proteome of Stau1-KO and Stau2-KO lines and the GC-related DEP, that Stau1 and Stau2 could regulate the stability and translation of largely separate target mRNAs and might act in different protein complexes in A20 cells. To address that question, I analysed the interactors of both Staufen paralogs.

Staufen paralogs interact with RNA maturation-related proteins

Considering that the Stau paralogs might form part of distinct RNP complexes targeting different mRNAs, I studied the interactors of both proteins by IP coupled to mass spectrometry, and the results are shown in Figure 26.

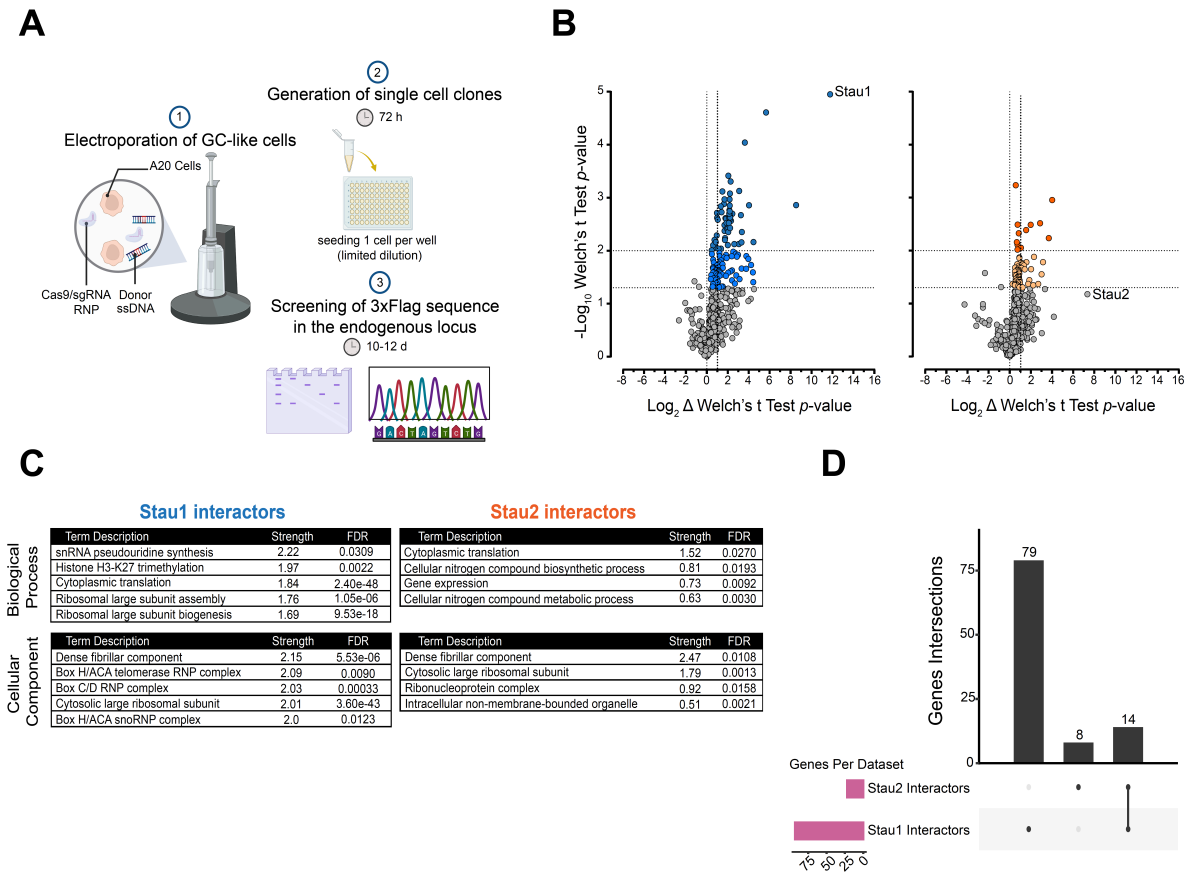

Figure 26: Staufen paralogs have different interactors. **A**. Diagram explaining the generation of endogenous Stau1 and Stau2-3xFLAG knock-in A20 clones. **B**. Volcano plots showing all detected proteins (grey) and the differentially expressed proteins (DEP; in colour) comparing the IP proteins of "non-flagged" A20 cells with 3x-FLAG-Stau1 (left) and Stau2-3xFLAG (right). The first dotted line at y=1.3 represents a *p*-value of 0.05, while the dotted line at y=2 represents a *p*-value of 0.01. **C**. Gene set enrichment analysis of the interactors of Stau1 (left) and Stau2 (right) in the biological processes (top) and cellular component (bottom) term. **D**. The up-set plot shows the intersections between the Stau paralogs.

Considering that the Stau2 antibody used in the previously shown Western blot is not commercially available and it detects other proteins below the MW < 50 kDa, I decided to generate Flag epitope knock-in (3xFLAG-Stau1 and Stau2-3xFLAG) A20 cell lines to use in pull-down assays. Upon successful generation and validation of these cell lines (see material and methods, Figure 26A), I pulled down either 3xFLAG-Stau1 or Stau2-3xFLAG from 3-4 single-cell-derived A20 clones with and without RNAse I treatment to identify mRNA-dependent and -independent Staufen interactors. Mass spectrometry-based proteomics was then performed to detect the co-immunoprecipitated proteins.

In the samples treated with RNAse, used to identify the RNA-independent interactors (possibly protein-protein interactions), I observed that Stau1 precipitated together with many more proteins compared to Stau2, considering a *p*-value<0,05 and FC>2 (Figure 26B) between FLAG-tagged vs non-FLAG-tagged cells. Specifically, 92 proteins were enriched by Stau1 pulldown and 23 by Stau2 pulldown. Reminiscent of the previous transcriptomic and proteomic experiments, the overlap between the two Staufen paralog interactors is just 15% of the Stau1 interacting proteins (Figure 26D). The Stau2 interactors, which are very few, overlap 64% with the Stau1-immunoprecipitated proteins. Next, I tried to establish a relationship among the interactors using the web app STRING STRING: functional protein association networks (string-db.org), where I obtained the enriched biological processes and cellular components related to the pulldowns. This analysis suggested that both paralogs might participate in the cytoplasmic translation and regulate gene expression. The analysis also indicated, as published before [120], that these RBPs might be located in the nucleus in A20 cells, particularly in the nucleoli, as depicted by the enriched “dense fibrillary component” term. Moreover, Stau1 might participate in the post-transcriptional modifications of RNA as it interacts with components of the Box H/ACA telomerase and Box C/D RNP complex.

I then analysed the RNA-dependent interactors, finding very few for both Staufen paralogs: 8 interactors for STAU1 and 6 for STAU2 (*p*-value<0,01). This may suggest that at steady state, the Stau paralogs are either not associated with other proteins or not conforming to convoluted RNPs depending on mRNA interactions but rather protein-protein interaction. However, among the identified interactors, for both Staufen, the pre-mRNA-processing-splicing factor 8 (Prpf8) and the regulator of nonsense transcript 1 (Upf1) were found, the latter a key element in Staufen-mediated decay (see introduction).

These results indicate that Staufen paralogs interact with other proteins related to RNA's maturation, translation and post-transcriptional modification in GCB-like cells. Stau1 is potentially involved in more processes than Stau2, considering the number of interactors and the associated cellular compartments. Next, I wanted to determine which mRNAs are directly targeted by the Staufen proteins and for that, I again took technical advantage of the FLAG epitope-tagged Staufen clones.

Infra-red UV-Crosslinked immune-precipitation (irCLIP) of the Staufen paralogs

To identify direct mRNA targets of the Staufen paralogs in A20 cells, I collaborated with Prof. Dr. Martin Turner (Babraham Institute), whose laboratory I visited to learn the necessary techniques. With the help of Dr. Twm Mitchell, I performed irCLIP on cell pellets of the FLAG-tagged clones previously exposed to UV-C radiation, as described in the materials and methods section and summarised in Figure 27.

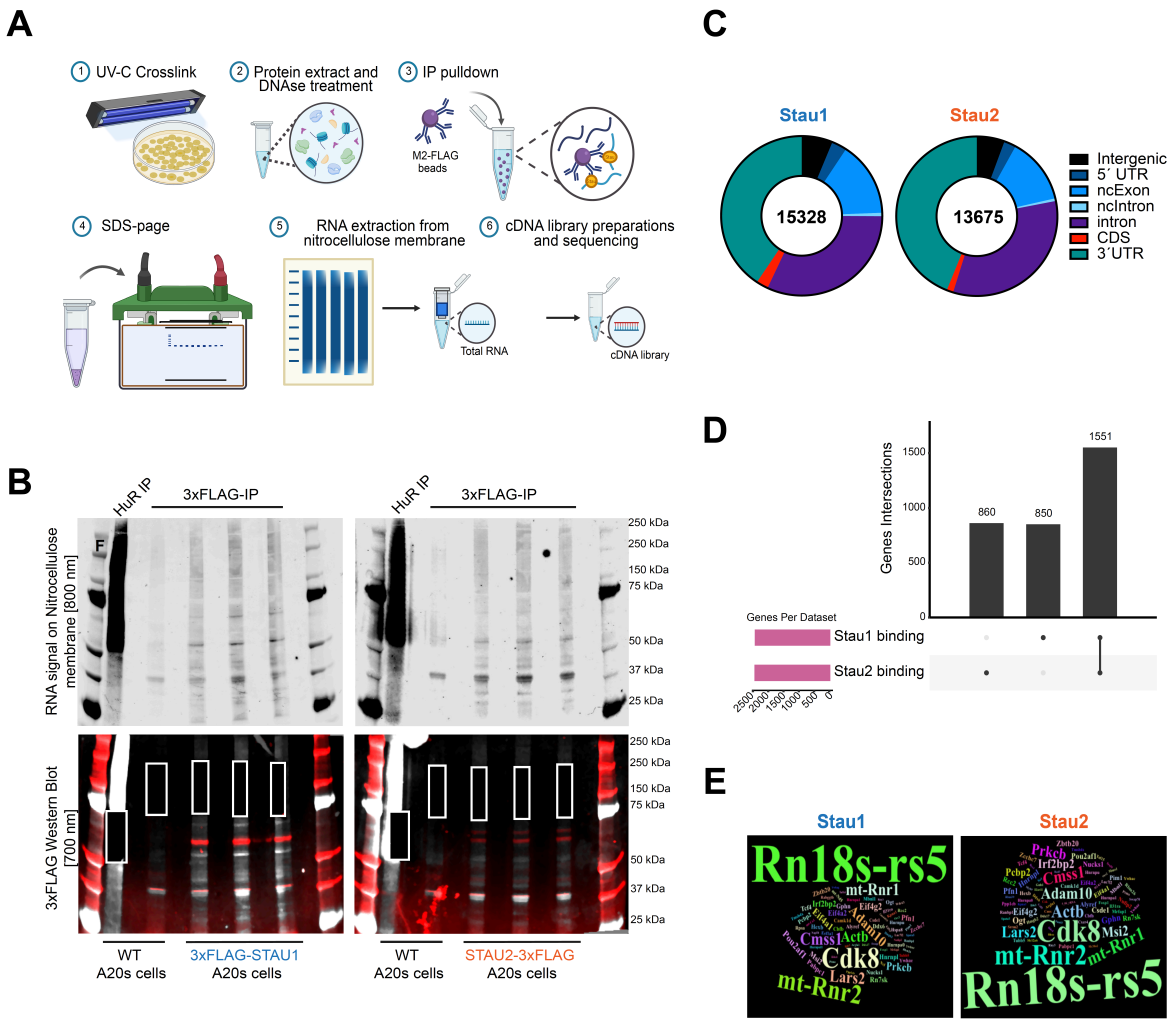

Figure 27: Staufen paralogs share two-thirds of their target's mRNAs. **A**. Diagram of the irCLIP protocol stating the major steps to determine the RNA targets. **B**. Nitrocellulose membranes showing the transferred RNA/HuR and RNA/Stau complexes (top) from SDS-page gels and the confirmation of the Stau IP by western blot (bottom) indicated by red bands. **C**. Pie charts showing the proportion of genetic features bound by the Stau paralogs and the total amount of bound sequences. **D**. Up-set plots showing the intersection of target genes by the Stau paralogs. **E**. Word cloud showing the top 40 RNA targets for each paralog.

After immunoprecipitating the Stau paralogs bound to their RNA targets using magnetic beads coupled to α-FLAG antibodies, I added fluorescent RNA adaptors to identify the RNA smears using an 800 [nm] fluorescent detector (Figure 27B). Compared with the RBP HuR (used here as positive control), the RNA intensity in the Stau pulldowns was weaker but visible. Thus, I cut the nitrocellulose membranes ~ 30 kDa above the typical migration pattern, expecting to obtain RNA-bound-Stau RNPs, as indicated by the white rectangles (Figure 27B, bottom). After purifying and retro-transcribing the bound RNA from three clones, I generated cDNA libraries and sequenced and mapped them using the virtual tool iMaps. To determine which genes are differentially bound and in which genomic feature, I ran a modified protocol from Louise Matheson (github.com/Process_CLIP_data). I considered mRNAs bound in two out of three libraries as valid target candidates. This analysis was also performed in the immunoprecipitated RNA from non-FLAG-tagged clones, where only one out of two samples gave detectable cDNA reads.

After performing the bioinformatic analysis, I observed that both paralogs bind genetic features similarly in A20 cells, with the 3'UTR being the most prominently bound feature. The intronic region was observed to be the second preferred RNA feature of the Stau paralogs, and the non-coding exons were the third (Figure 27C). Moreover, both paralogs had similar reads (although 1653 more in Stau1 irCLIP) comprising an equal number of bound mRNAs: 2401 for Stau1 and 2411 for Stau2 (Figure 27D). In line with previous knowledge detailed in the Introduction, I observed that in A20 cells, both Staufen paralogs share around 2/3 of the total Staufen-bound mRNAs. However, the Stau paralogs also have non-overlapping potential target mRNAs, suggesting they could regulate different mRNAs.

Among the most targeted mRNAs by the paralogs, there are many cell-cycle and housekeeping-related mRNAs, but also mitochondrial ribosomal RNA and ribosome-structural components, as shown in the word cloud (Figure 27E).

Despite being a powerful tool for determining RNA-protein interaction and the consistency of my results to previous studies comparing RNAs bound by both Staufen paralogs, irCLIP is not free of technical difficulties that can affect the validity of the results. One significant technical problem associated with UV crosslinking is the potential for non-specific crosslinking, which can lead to background noise in the data. Non-specific interactions can complicate the interpretation of results, as they may obscure the true binding partners of the RBPs being studied. For instance, while UV-crosslinking can enrich transient protein-RNA complexes, it

can also inadvertently crosslink proteins not functionally relevant to the RNA of interest, complicating downstream analyses such as sequencing and data interpretation [121, 122]. Moreover, UV-crosslinking efficiency can vary depending on the specific conditions used, such as the wavelength of light and the duration of exposure, which can further contribute to variability in results [123]. To get a first impression of the validity of my results, I investigated Bcl6 as a target of Staufen paralogs due to its fundamental relevance in GCB cells.

BCL6: a potential novel target of Staufen paralogs in A20 cells

The proteome analysis revealed that Bcl6 is downregulated in Stau1-KO A20 cells; thus, considering the high relevance of this transcriptional modulator for GCB cells, I decided to check whether the Staufen paralogs are targeting the Bcl6 RNA since it was also a hit in the irCLIP data.

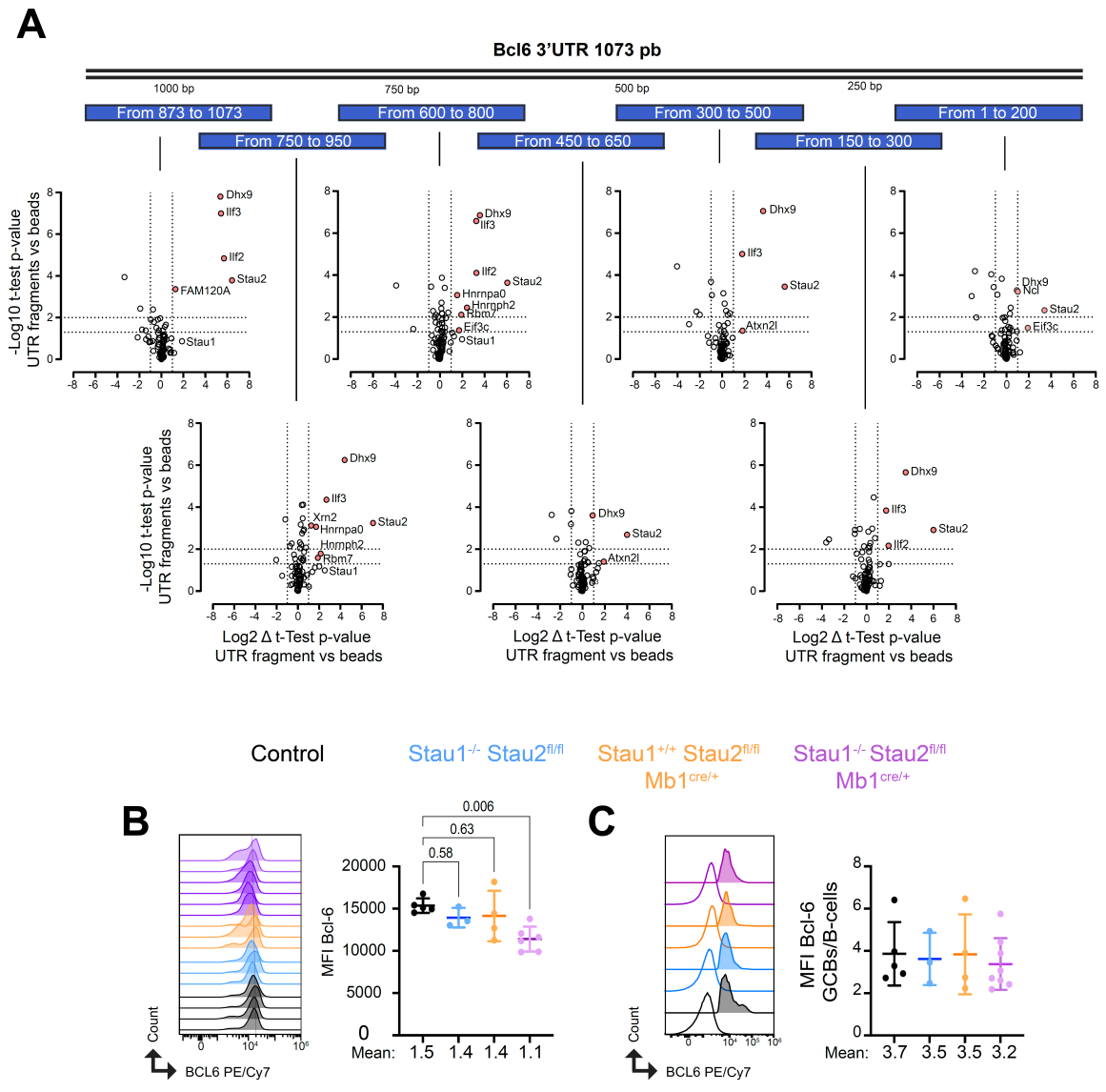

Figure 28: Staufen paralogs bind Bcl6 3'UTR in A20 cells. **A**. Hawaii plot showing the pulled-down enriched proteins obtained with beads coupled or not to a Bcl6-3'UTR fragment. **B**. Histograms (left) and scatter plot (right) show the mean ± SD MFI BCL6 in sufficient single and double Stau-deficient A20 cells. **C**. Histograms (left) and scatter plot (right) showing the normalised mean ± SD MFI BCL6 measured in spontaneous primary GCB cells. The MFI of BCL6 was normalised by the value obtained from total B-cells. In B, the data of one experiment is plotted, while in C, the data from 2-3 independent experiments. In all scatter plots, a one-way ANOVA t-test with a Dunnett's multiple comparison test comparing the mean of each genotype with the control was performed, finding statistical differences when the *p*-value (about the brackets) is <0,05.

In the irCLIP data, I observed that the 3'UTR of Bcl6 mRNA is targeted by Stau1, suggesting it could be a target of Stau1 since that protein was observed differentially expressed between Stau1-deficient and WT A20 cells. In parallel to my efforts, Dr. Fatemeh Mohagheghi identified proteins binding to the 3'UTR of the Bcl6 mRNA by using mRNA interaction proteomics in A20 cells: she generated magnetic beads coupled to 200 bp of RNA-fragments of the Bcl6-3'UTR (each fragment had a 50 bp overlap with the prior and following fragment), which were mixed with protein extracts of A20 cells. Then, the "proteins pray" were identified by LC-Mass spectrometry. These experiments showed that 12 different proteins bind the Bcl6-3'UTR, the most frequent being the RBPs Ilf3, Dhx9, and Stau2. The last two were identified in all the segments, which could represent a technical artefact of pulling down proteins with RNA fragments from cell lysates since both RBPs bind dsRNA. Regarding Stau1, this paralog was highly enriched (Log2FC ~ 2), specifically in the region between 600-1073 bp, correlating with the irCLIP results.

After checking the expression of Bcl6 by intracellular flow cytometry, I observed that the median fluorescent intensity (MFI) average of Bcl6 is similar between Stau1-KO and WT A20 clones, which generates a discrepancy to the observed in the proteome. On the other hand, Stau1/2-DKO A20 cells have a small but significant decrease in the protein levels of Bcl6 (Figure 28D), which was not detected in the proteome analysis.

To investigate whether the BCL6 reduction also occurs in primary GCB cells, I compared the ratio of BCL6 MFI between GCB and B-cells in single and double conditional Staufen KO B-cells from naïve mice. I observed no differences between the genotypes (Figure 28E).

Potentially relevant Staufen target mRNAs in GCB cell-like A20 cells

Considering the variability among the irCLIP, the proteome, and the flow cytometry data on measurement of Bcl6, I focussed on the most differentially expressed proteins (FC>4) in the Staufen paralog knockout A20 cell lines to determine the potential Stau-regulated genes with consistent measurements among different experiments (Figure 29). By choosing those genes, I was expecting consistency between the clones or genotypes, which could preliminary validate the proteome.

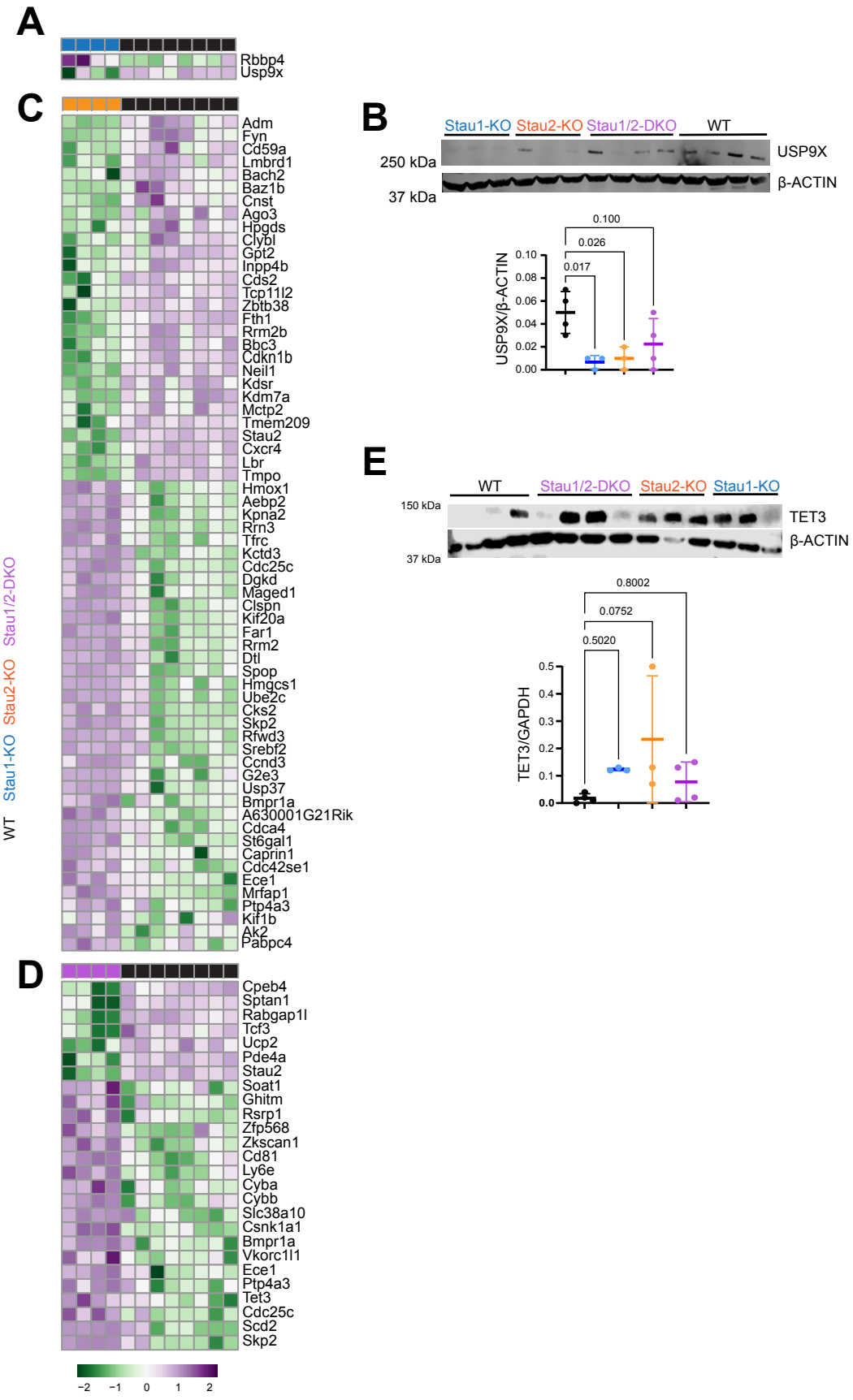
A
Rbbp4
Usp9x
C
WT
Stau1-KO
Stau2-KO
Stau1/2-DKO
Adm
Fyn
Cd59a
Lmbrd1
Bach2
Baz1b
Cnst
Ago3
Hpgds
Clybl
Gpt2
Inpp4b
Cds2
Tcp11l2
Zbtb38
Fth1
Rrm2b
Bbc3
Cdkn1b
Neil1
Kdsr
Kdm7a
Mctp2
Tmem209
Stau2
Cxcr4
Lbr
Tmpo
Hmox1
Aebp2
Kpna2
Rrn3
Tfrc
Kctd3
Cdc25c
Dgkd
Maged1
Clspn
Kif20a
Far1
Rrm2
Dtl
Spop
Hmgcs1
Ube2c
Cks2
Skp2
Rfwd3
Srebf2
Ccnd3
G2e3
Usp37
Bmpr1a
A630001G21Rik
Cdca4
St6gal1
Caprin1
Cdc42se1
Ece1
Mrfap1
Ptp4a3
Kif1b
Ak2
Pabpc4
D
Cpeb4
Sptan1
Rabgap1l
Tcf3
Ucp2
Pde4a
Stau2
Soat1
Ghitm
Rsrp1
Zfp568
Zkscan1
Cd81
Ly6e
Cyba
Cybb
Slc38a10
Csnk1a1
Bmpr1a
Vkorc1l1
Ece1
Ptp4a3
Tet3
Cdc25c
Scd2
Skp2
−2 −1 0 1 2
B
Stau1-KO Stau2-KO Stau1/2-DKO WT
250 kDa
37 kDa
USP9X
β-ACTIN
0.100
0.026
0.017
USP9X/β-ACTIN
0.10
0.08
0.06
0.04
0.02
0.00
E
WT Stau1/2-DKO Stau2-KO Stau1-KO
150 kDa
37 kDa
TET3
β-ACTIN
0.8002
0.0752
0.5020
TET3/GAPDH
0.5
0.4
0.3
0.2
0.1
0.0

Figure 29: Usp9x as a potential Stau-regulated gene. **A**. High DEP between Stau1-KO and WT cells whose encoding mRNAs are targeted by the Stau paralogs. **B**. Western blot showing the expression USP9X in different A20 cell clones WT, single and double Stau-deficient cells (top), and scatter plot showing the mean ± SD normalised expression of Usp9x to β-ACTIN. **C**. High DEP between Stau2-KO and WT cells whose encoding mRNAs are targeted by the Stau paralogs. **D**. Highly DEP between Stau1/2-DKO and WT cells whose encoding mRNAs are targeted by the Stau paralogs. **E**. Western blot showing the expression TET3 in different A20 cell clones WT, single and double Stau-deficient cells (top), and scatter plot showing the mean ± SD normalised expression of TET3 to GAPDH. In all scatter plots, a one-way ANOVA t-test with a Dunnett's multiple comparison test comparing the mean of each genotype with the control was performed, finding statistical differences when the *p*-value (about the brackets) is <0,05.

Among the high DEP between Stau1-KO and WT, I cross-referenced the Stau-targeted mRNAs determined by irCLIP, finding two potential direct Stau1 targets mRNAs (Figure 29A): the *histone-binding protein RBBP4* (Rbbp4) is up-regulated in Stau1-KO A20 cells and both Staufen paralogs target its encoding RNA; the *probable ubiquitin carboxyl-terminal hydrolase FAF-X* (Usp9x), which is down-regulated in Stau1-KO A20 cells and whose mRNA is bound by Stau1. Since mice deficient in Usp9x have a reduced activation in vitro upon IgM and CD40 stimulation [124], which is related to the signal required for GCB cell differentiation, I performed a Western blot to corroborate the findings of the proteomic analyses. I confirmed that Usp9x protein levels are downregulated in Stau1-KO cells, although there was substantial clone-to-clone variability (Figure 29B). Usp9x protein reduction was also observed in Stau2-KO cells by Western blot (although not in the proteome). Moreover, Stau2 has several crosslink sites in the Usp9x mRNA, indicating direct binding, identified in both replicates used in the irCLIP pipeline.

Similar to the situation with Stau2-KO A20 clones, I found several high DEPs between Stau1/2-DKO and WT cells whose encoding mRNA is bound by the Staufen paralogs (Figure 27D). Of potential interest, I found the *Methylcytosine dioxygenase* TET3 to be upregulated in Stau1/2-DKO A20 clones, which, together with its paralog TET2, regulates SHM, CSR and the expansion of GCB cells [125]. Next, to validate this target, I performed a Western blot for this protein in the cell lines, observing that its expression is, on average, higher in single and double Stau deficient A20 cells. However, none of these differences reached statistical significance due to the high variability between the A20 clones, which needs investigation.

Altogether, the integration of my proteomic (and transcriptomic) datasets with the irCLIP data focussing on highly DEP allowed me to identify candidates Staufen-regulated mRNAs with published roles in GCB cell biology as well as several other candidate mRNAs with no known

functions in GCB cells, but who are implicated in relevant cellular processes. However, the incongruences between the single-cell derived clones among the genotypes are concerning, and the western blot results did not fully validate the proteome data. In the case of Usp9x (Figure 29B), the difference between WT and Stau1KO A20 clones is solid and consistent between the proteome and its western blot validation. However, Stau2KO A20 clones also have an average lower expression of USP9X measured by western blot, showing clonal variability since only one out of three clones have a clear band for the target protein. This difference was not detected in the proteome data. This could have been due to the low frequency of peptides of that protein in the sample preparation during LC-MS. Similarly, I could not obtain consistent bands while measuring TET3 by western blot among the clones of the different genotypes.

The pre-filtered list of candidate Stau-regulated mRNAs presented in Figure 29 could be used in follow-up experiments to determine their relevance in GCB cell biology and further validation in primary cells.

DISCUSSION

GC-related RBPome

The starting point of this thesis was a quantitative comparison of the proteomes of GCB cells and mantle zone B cells. Many known GC regulators, including AID, BCL6, and EFB1, were identified as highly expressed in this analysis, confirming the robustness of our dataset. Then, considering their critical roles in post-transcriptional regulation, I assessed differential RBP protein levels between GCB and mantle zone B cells. The rationale for this approach was that the activities of RBPs, which exert their functions through direct mRNA binding, should correlate to a large degree with their protein level in the cells. I observed that Staufen 2 is specifically expressed in the GCB cells, which has yet to be deeply investigated in the adaptative immune system. Thus, I generated mice with B cell-specific Stau2 deficiency via the LoxP/Cre technology.

Staufen 2 is dispensable for GCB cell differentiation but might modulate affinity maturation

Considering that Stau2 has a role in mitosis both in cell lines and in pluripotent stem cells and that this RBP is specifically expressed in GCB cells, which undergo massive proliferation in their differentiation process, I postulated that Stau2 has a significant role in GCB cells.

During the results collected in this thesis, I observed that mice bearing Stau2 haploinsufficient or knockout in B-cells display similar spontaneous generation of GCB cells at a steady state in the spleen and secondary lymph nodes compared to control mice. I observed no differences in the number of cells in all analysed tissues, neither in the proportion nor number of B1 or B2 B-cells. The GC compartment was also unaffected. In immunised mice, similar to naïve animals, I noted no significant differences in the spleen weight, cellularity and proportion nor the number of B-cells and GCB cells between B cell-specific Stau2 knockout and control mice. However, the median number of total GCBs is 2,4 and 1,6 times lower than that of control animals on days 10 and 28 post-immunisation, respectively. Regarding NP-specific GCBs, mice bearing Stau2-deficient B-cells have a similar number of cells than control mice. Suggesting that the Stau2 RBP is not significantly implicated in the differentiation or the expansion of antigen-specific GCB cells.

Later, I analysed the humoral response upon immunisation, observing that B cell-specific Stau2 knockout mice have similar antigen-specific IgG1 and IgM titers as control mice. Similarly, the affinity maturation depicted for the ratio between high-affinity antibodies and total antibodies against the antigen is similar between mice bearing Stau2-sufficient and insufficient B-cells for IgM. However, it is significantly altered in the NP-specific IgG1 response. At days 21 and 28 post-immunisation, mice with Stau2-deficient B-cells have a lower NP_2/NP_{36} ratio. This may indicate that this paralog modulates mechanisms involved in affinity maturations, including the SHM process, at the molecular level. However, at the cellular level, there were no significant differences in the proportion of dark zone GCB cells, which are the cells facing that process.

Other experimental approaches must be performed to study the role of Stau2 in affinity maturation. For instance, almost all the antibodies generated against NP bear a heavy chain subclass γ1 encoded by the V_H186.2 segment, the D_H element DF116.1 and J_H2, and a λ1 light chain [93, 126, 127], thus sequencing the complementary-determining region (CDR) 3 of that VDJ re-arrangement in the GCB cells will indicate the level of the mutations. Differences in the mutation patterns should be analysed, including coding versus non-coding and their localisation. A convenient readout consists of assessing high-affinity related mutations, such as the replacement of W with L in the codon 33 of the VH186.2 segment, which increases the affinity for NP 10-fold [128] between control and B cell-specific Stau2-deficient mice could address this question.

Although I did not directly address SHM in this thesis, I tried to determine molecular targets of Stau2 that could be related to this and other processes relevant to GC biology using the A20

cell line model, which I and others demonstrated to reflect gene expression and certain properties of GCB cells. The A20 cell line has an impairment in the expression of AID upon Stau2 deficiency. Since mice deficient in AID accumulate fewer mutations in the V_H186.2 segment [129], a lower expression of this enzyme in immunised B cell-specific Stau2 knockout mice might explain the potential lower affinity maturation observed for IgM antibodies. Similarly, Stau2-deficient A20 cells also have lower expression of Neil1, an oxidised damage-specific glycosylase abundant in GCB cells. Mice deficient in Neil1 have a reduced GC response upon NP-immunisation with a lower titer of antigen-specific IgG1 and less mutation frequency in the J_H4 intronic region, depicting less SHM [119]. Therefore, this is also a potential molecular mechanism contributing to the trend for lower affinity maturation in B cell-specific Stau2 knockout mice. In the same line, I found that Stau2-deficient A20 cells downregulate the transcription factor Bach2, which is also relevant for the SHM since mice deficient in this gene have less accumulation of mutations in the V_H186.2 segment [130].

From the three genes mentioned above that are important for SHM, the Staufen RBPs do not bind the mRNA encoding AID. In contrast, Neil1 and Bach2 were by either paralog according to the irCLIP data I generated. Moreover, the Bach2 mRNA is downregulated in the transcriptome of Stau2-KO A20 cells, while Aicda and Neil1 are at similar levels to WT cells. Therefore, these results suggest that Stau2 may regulate the expression of Bach2 and Neil1. On the other hand, Aicda may be controlled by the Staufen proteins through an indirect mechanism.

Notwithstanding these possibilities, further validation must determine whether Staufen proteins regulate the mRNAs for Bach2 and Neil1 in primary cells. An experimental approach could include immunising mice carrying Stau2 deficient and control B-cells containing a BCR knock-in recognising NP [131]. In this mouse model, many responder B-cells are generated and suitable for orthogonal omics experiments upon immunisation. The transcriptomic and proteomic analysis could validate the previous observations in A20 cells, and omics integration with ribosome profiling, as detailed for B-cells [132], could address the mRNA-localisation role of Stau2.

Stau1 is important for the GCB expansion and the humoral response upon immunisation

During the analysis of the role of Stau2 in spontaneous GCB cell differentiation, a redundant role of Stau1 could underlie the lack of differences between control and B cell-specific Stau2 knockout mice. This notion is supported by reports stating that the paralogs might share target

mRNAs and that both Staufen have similar transcription patterns in human GCB cells. However, when I analysed Stau1-deficient mice, I observed no difference in the cell numbers or proportion of total B1 cells, B2 B-cell subsets or spontaneous GCB cell populations compared to WT animals. Upon immunisation, Stau1-deficient mice have reduced GCB cells with a reduced GCB cell number at the peak of the immune response and a reduced titer of antigen-specific IgG1 from 21 days post-immunisation. The NP-specific IgG1 response in Stau1 knockout mice displayed a similar affinity maturation as control animals, suggesting an issue with generating optimal amounts of NP-specific IgG1 antibodies but not with their affinity.

T follicular helper cells (T_{FH}) and follicular dendritic cells (FDCs), which are essential for the GCB cell generation, providing antigen, co-stimulatory molecules, and survival signals [133-135], are also Stau1-deficient in the mouse model used during this thesis. The role of Stau1 in these cell populations has yet to be studied. Thus, the possibility that the results of this research are related to an impairment in the function of FDCs or T_{FH} cannot be ruled out. Therefore, to validate my observations in B cells, one should restrict the Stau1-deficiency to this population and study their specific responses to immunisation.

During this thesis, I studied the development of T-cells by frequency of populations in the thymus and periphery, finding no differences between Stau1 knockout and WT mice. Similarly, I found that Stau1 does not affect the proportion of Treg cells nor effector/memory-like $CD8^+$ or $CD4^+$ T-cells in the spleen and secondary lymph nodes. However, T-cell activation and differentiation of T_{FH} were not assessed during this work. One way to evaluate the possible effects of Stau1 deficiency in non-B-cell populations is the generation of mixed bone marrow chimaeras. This would involve mixing Stau1-knockout and control (B-cell-deficient $Mb1^{-/-}$ or similar) hematopoietic stem cell and progenitor cells followed by transferring into B-cell-deficient myeloablative irradiated recipient mice (similarly to [136]). The non-B-cells will also be Stau1-sufficient with this experimental approach, while all B-cells will be Stau1-deficient. Alternatively, similar to the model I generated for the Stau2 experimental approach, conditional knockout mice could be generated by breeding $Stau1^{F/F}$ mice, recently commercially available at Stau1-flox|Strain NO.T019627, with AID^{cre} mice [137] to specifically study the role of Stau1 in GCB cells.

To address a possible Stau1-regulation mechanism in GCB cells, I compared the proteome of Stau1 knockout and WT A20 cells, and I found Bcl6 downregulated in cells lacking Stau1 expression. A lower expression of this transcriptional repressor could have explained the reduction of GCB cells upon immunisation since Bcl6 is essential for GCB cell differentiation, promoting the survival of cells after the DNA breaks generated in the CSR, among other

functions. Moreover, the Bcl6 3'UTR has a Stau1 binding motif (Motif: AGGGGAG [77]) and can be bound by Stau1, as determined by two independent experimental approaches shown in the results section. However, spontaneous Stau1-knockout GCB cells have a similar Bcl6 expression as control GCB cells. This does not necessarily completely rule out a minor role for Stau1 in regulating Bcl6 protein levels. This could be addressed in analyses of Bcl6 expression in antigen-specific responder B-cells at early time points where high and low-affinity activated B-cells, with heterogeneity in expression of Bcl6, depicted, for instance, by variable CD80 expression [138], are competing for survival signals given by T-cells.

Another Staufen target that might explain a reduction of GCB cells in Stau1-deficient mice is Usp9x. B cells deficient in this deubiquitinase have a reduced activation upon BCR activation, affecting their in vitro proliferation and viability [124]. Stau1-deficient A20 cells have a decreased expression of Usp9x, and its encoding mRNA is targeted by Stau1, suggesting this RBP might control the Usp9x expression in GCB cells. Considering there was no DEG between Stau1-KO and WT A20 cells in the transcriptomic analysis performed in this thesis, this regulation might occur at the translational level since, similar to Stau2, Stau1-interactors are involved in cytoplasmatic translation. Thus, further experimental setup to assay these findings could be analysing the Usp9x expression in resting and activated B-cells WT and Stau1-KO, which was not performed during the timeframe of this thesis.

Staufen1/2 double-deficiency in B-cell does not affect the humoral response, but the affinity maturation

Reports have stated that the Staufen paralogs might share some of their targets. To study whether that could be the case in B-cells, I analysed the targets of both paralogs in A20 cells by irCLIP, finding they share around two-thirds of their bound mRNAs. This may indicate that Staufen paralogs have redundant functions in B cells. That could explain why I observed almost no differences in single Stau1 or conditional Stau2-deficient mice compared to control animals when I studied spontaneous GCB cell responses.

Therefore, during this doctoral work, I generated mice lacking both Stau paralogs in B-cells. Of note, the mice were entirely deficient for Stau1, which did not dramatically impact the major immune populations, as proved by the extensive immune phenotyping of the naïve mice described in the result section, but still might have influenced the context of B-cell help as discussed before. Similar to mice containing Stau1 and Stau2 single knockout B-cells, there were no differences at steady state compared to control mice in the proportion nor number of total B-cell subsets and spontaneous GCB cells in the B cell-specific Stau2 deficient Stau1$^{-/-}$

mice. However, at the peak of the immune response against NP, the GCB cell number was reduced, similar to what I observed in Stau1-deficient mice.

According to the proteomic data, Stau1/2 double knockout A20 cells have reduced levels of AID and Neil1, which might explain the reduced GCB cell number upon immunisation in mice lacking both Staufen paralogs in B-cells. However, after analysing the differentially expressed proteins in the mass spectrometry analyses whose encoding transcripts are bound by the Staufen paralogs in A20 cells, I observed that the E2A transcription factor, encoded by Tcf3 and targeted by both Staufen paralogs, was downregulated. This could be another candidate molecular mechanism to explain the reduction in GCB cells upon antigen delivery. EA2 has been extensively studied in pre and pro-B-cells [139]. EA2 is differentially expressed in follicular B cells and GCB cells, and mice bearing EA2-deficient B-cells have an impairment in the expansion of GCB cells upon NP-coupled proteins and sheep red blood cell immunisation [140]. Therefore, considering that changes in Tcf3 mRNA levels were not detected in the transcriptome data in any of the Staufen-deficient A20 clones, I speculate that Staufen paralogs might cooperatively potentiate the translation of EA2.

Interestingly, E2A binds four Aicda enhancer sequences, promoting its transcription after two days of α-CD40/IL-4 treatment [140]. Since AID is downregulated in Stau2-deficient and Stau1/2 double knockout A20 cells, this could be the molecular mechanism affecting the affinity maturation in those genotypes. However, the Staufen paralogs do not target Aicda RNA so that E2A might be the molecular link in these observations in the Stau1/2-deficient B-cells. In Stau2 knockout A20 cells, E2A is not differentially expressed; thus, other molecular mechanisms could also regulate the AID expression.

Strikingly, B cell-specific Stau2 deficient Stau1$^{-/-}$ mice do not show the antigen-specific IgG1 titer impairment I observed in the Stau1 knockout mice. The differentiation of antigen-specific plasma cells (PC) must be assessed to address this issue. In the hypothetical case that Stau1$^{-/-}$ but not Stau2 deficient Stau1$^{-/-}$ mice are defective in generating PCs, Stau2 could act by repressing PC-related features in the absence of Stau1. These features could include differentiation, unsuccessful up-regulation of the immunoglobulin heavy chain locus essential for the switch of membrane-bound to secreting-IgG1 [141], or overall class-switch recombination capacity. Then, after ablation of both Stau paralogs, the Stau2-mediated repression of PC-biology is released, leading to similar antigen-specific IgG1 titers to that of control mice. To address this speculation, the expression of genes whose mRNAs are targeted by both Stau paralogs must be studied in primary single and double Staufen paralog deficient GCB cells.

Stau paralogs control the spleen's cellularity

Stau1/2 double-deficient mice have significantly reduced spleen weight, with fewer splenocytes without affecting the proportions of T and B-cells. This suggests impaired processes regulating spleen size and cell numbers. Considering that complete Stau1 deficiency does not impact the spleen weight and cellularity, I initially thought that both Stau paralogs expressed simultaneously in other cell types relevant for the spleen morphology were producing that phenotype. Surprisingly, in B-cell Stau2 deficient Stau1$^{-/-}$ mice, I also observed a trend towards a similar difference in the spleen and bone marrow from the femur and tibia without significantly affecting the number or proportion of B220^{+} cells in the mentioned tissues. Since mLN and PPs were unaffected in their cellularity or weight, I initially thought that B-cell migration through the blood may be affected since the population of the spleen is mainly determined by the bloodstream [107]. However, other factors could underline this phenotype.

Histological analysis of the microstructure of the spleen could bring hints of the origin of the cellularity differences. Regarding that, transcriptional data from immgen indicate that Mb1 is also expressed in lymphatic endothelial populations as CD45^{-} CD131^{-} PDPN^{-} ITGA7^{+}, suggesting these cells might also be Staufen-deficient in the used mouse model. As the role of Staufen paralogs in endothelial populations has yet to be addressed, the possible outcome is unknown. To avoid B-cell extrinsic Staufen regulation in future experiments, bone marrow chimaeras can be generated as commented before, or mice with Cre-expression can be used under the regulation of other genes. Fcer2a (encoding CD23), which is expressed mainly in FoB and is around 4-fold less transcribed in endothelial cells than Mb1, could be an option, or mice expressing Cre under the regulation of Aicda, which is principally expressed in GCB cells and it is transcribed about 29-fold less than Mb1 in endothelial cells could be another.

Regarding B-cell biology, the data collected during this doctoral work suggest that Stau paralogs may be involved in the B-cell expansion upon immunisation. At the peak of the immune response against NP, B cell-specific Stau2-deficient Stau1$^{-/-}$ mice have statistically significantly fewer splenocytes and B-cells than control mice. Considering that differences were not observed in immunised Stau1$^{-/-}$ mice, this phenotype may be mediated by both Staufen paralogs. Curiously, this difference is not observed 28 days after immunisation when the number of B-cells is somewhat similar among all genotypes, making the changes in B-cell numbers challenging to interpret.

In the GCBs compartment, Stau1$^{-/-}$, B cell-specific Stau2-deficient and B cell-specific Stau2-deficient Stau1$^{-/-}$ mice have a median cell number between 2 to 3-fold lower than control mice,

which might indicate that both paralogs are relevant in generating optimal numbers of GCBs, although only in Stau1$^{-/-}$ and Mb1^{cre} Stau1$^{-/-}$ Stau2$^{F/F}$ mice this difference is statistically significant. Consistently, 28 days post-immunisation, all genotypes have fewer GCBs, although this difference is significant only in B cell-specific Stau2-deficient Stau1$^{-/-}$ mice. Altogether, this might indicate Stau paralogs play a role in the differentiation or expansion of GCBs upon immunisation, which requires further validation. In vitro proliferation assays in response to different stimuli could help addressing this possibility, as well as immunisation of mice with T-independent antigens, which should show a similar result in GCB number as observed in NP administration.

irCLIP variability between replicates

While analysing the irCLIP data, I realised that the resolution, meaning the nucleic sequence where the Stau proteins bind, between the replicates needed to be revised. After the pipeline analysis identified a significant hit in a gene, for example, Bcl6, there were differences in the region where the Stau paralogs bound the nucleotides, and very often, the binding regions were displaced several nucleotides between the replicates. In some other cases, the distribution of the peaks (number of times the Stau proteins bind a region) was displaced within a gene region between the replicates; in others, the peaks were in only one replicate. Therefore, some technical problems may need clarification between replicates.

As commented on the result section, the noise generated by unspecific binders is a negative side of the UV-crosslink. In my case, the crosslink conditions applied were fine-tuned for an RBP binding RNA Poly-U tails in T-cells (specified in methods), which are not necessarily the best conditions for studying dsRBP in B-cells. Thus, deep optimisation could be beneficial in which either the UV features or other crosslinker reagents could be tested, such as dithiol (bis-) succinimidyl propionate, since it offers reversible binding between close peptides potentially valuable for identifying also Stau-containing RNPs [142]. Moreover, using other crosslinkers could avoid the RNA degradation generated by the UV, which results in the loss of critical information about the RNA's structure and function, particularly in cases where the RNA is already present in low abundance [121, 143]. Therefore, other CLIP methodologies need to be performed, and the readouts cross-referenced with those shown in this thesis to validate my preliminary results.

Clonal variability and protein target validation

As commented in the result section, one aspect that might influence the variability of the western blot results performed to validate the proteome preliminary is the variability between A20 cell clones. For instance, it has been demonstrated that single-cell subcloning of CHO (Chinese hamster ovary) cell lines resulted in a broad spectrum of expression and product quality heterogeneity. This variability was attributed to the high plasticity of the CHO genome, which can undergo continuous genetic changes and drifts during culture [144]. In my data, all clones within a genotype have overall similar transcriptomes and proteomes, as shown in the PCA analysis plot. However, the karyotype composition and genetic drift were not assessed, and there might be diversity between the clones. In addition, as commented previously in the literature, clonal derivation does not guarantee homogeneity within a cell bank, which can lead to variations in (bio)product quality and consistency [145]. Thus, repeating the omics analysis with bulk A20 cells could be an alternative to obtaining more reproducible results. Even better, a mechanism to get enough material from primary GCB cells could be ideal for determining whether Stau paralogs influence the proteome of this cell population.

CONCLUDING REMARKS

In this thesis, a comprehensive investigation into the regulatory roles of Staufen 1 and Staufen 2 in GCB cells sheds light on their involvement in various facets of adaptive immune responses. Initially, the focus was identifying differentially expressed RNA-binding proteins (RBPs) between GCB cells and mantle zone B cells, revealing Stau2's specific expression in GCB cells. Despite Stau2's dispensability for GCB differentiation, its potential role in modulating affinity maturation emerged from observations of slightly altered antibody affinity in Stau2-deficient mice post-immunization. Further exploration uncovered possible molecular mechanisms involving Stau2 in somatic hypermutation (SHM), implicating factors such as Bach2 and Neil1. Similarly, investigations into Stau1 revealed its importance in GCB expansion and humoral responses, potentially promoting B-cell activation, class switch recombination (CSR), and GCB differentiation where Usp9x might be involved. Examining Staufen1/2 double-deficient mice underscored redundant functions shared by Stau1 and Stau2, with implications for GCB expansion where E2A might be affected. Together, these findings contribute to elucidating the intricate regulatory networks governed by the Staufen paralogs in orchestrating critical processes within the adaptive immune system, providing a foundation for future research to decipher their precise molecular mechanisms and implications.

REFERENCES

1. Bonilla, F.A. and H.C. Oettgen, *Adaptive immunity.* J Allergy Clin Immunol, 2010. **125**(2 Suppl 2): p. S33-40.
2. Roco, J.A., et al., *Class-Switch Recombination Occurs Infrequently in Germinal Centers.* Immunity, 2019. **51**(2): p. 337-350 e7.
3. Victora, G.D. and M.C. Nussenzweig, *Germinal Centers.* Annu Rev Immunol, 2022. **40**: p. 413-442.
4. De Silva, N.S. and U. Klein, *Dynamics of B cells in germinal centres.* Nat Rev Immunol, 2015. **15**(3): p. 137-48.
5. Basso, K. and R. Dalla-Favera, *Germinal centres and B cell lymphomagenesis.* Nat Rev Immunol, 2015. **15**(3): p. 172-84.
6. Diaz-Munoz, M.D. and I.C. Osma-Garcia, *The RNA regulatory programs that govern lymphocyte development and function.* Wiley Interdiscip Rev RNA, 2022. **13**(1): p. e1683.
7. Keene, J.D., *RNA regulons: coordination of post-transcriptional events.* Nat Rev Genet, 2007. **8**(7): p. 533-43.
8. Wong, R. and D. Bhattacharya, *Basics of memory B-cell responses: lessons from and for the real world.* Immunology, 2019. **156**(2): p. 120-129.
9. Moir, S. and A.S. Fauci, *B cells in HIV infection and disease.* Nat Rev Immunol, 2009. **9**(4): p. 235-45.
10. Fuertes, T., I. Salgado, and V.G. de Yebenes, *microRNA Fine-Tuning of the Germinal Center Response.* Front Immunol, 2021. **12**: p. 660450.
11. Xu, S., et al., *The RNase III enzyme Dicer is essential for germinal center B-cell formation.* Blood, 2012. **119**(3): p. 767-76.
12. Tan, L.P., et al., *miRNA profiling of B-cell subsets: specific miRNA profile for germinal center B cells with variation between centroblasts and centrocytes.* Lab Invest, 2009. **89**(6): p. 708-16.
13. Ivanovska, I., et al., *MicroRNAs in the miR-106b family regulate p21/CDKN1A and promote cell cycle progression.* Mol Cell Biol, 2008. **28**(7): p. 2167-74.
14. Schneider, C., et al., *MicroRNA 28 controls cell proliferation and is down-regulated in B-cell lymphomas.* Proc Natl Acad Sci U S A, 2014. **111**(22): p. 8185-90.
15. Teng, G., et al., *MicroRNA-155 is a negative regulator of activation-induced cytidine deaminase.* Immunity, 2008. **28**(5): p. 621-9.
16. Leucci, E., et al., *B-cell differentiation in EBV-positive Burkitt lymphoma is impaired at posttranscriptional level by miRNA-altered expression.* Int J Cancer, 2010. **126**(6): p. 1316-26.
17. Porstner, M., et al., *miR-148a promotes plasma cell differentiation and targets the germinal center transcription factors Mitf and Bach2.* Eur J Immunol, 2015. **45**(4): p. 1206-15.
18. Huang, C., et al., *Cooperative transcriptional repression by BCL6 and BACH2 in germinal center B-cell differentiation.* Blood, 2014. **123**(7): p. 1012-20.
19. Hu, Q., et al., *Bach2 regulates B cell survival to maintain germinal centers and promote B cell memory.* Biochem Biophys Res Commun, 2022. **618**: p. 86-92.
20. Tan, H., et al., *Integrative Proteomics and Phosphoproteomics Profiling Reveals Dynamic Signaling Networks and Bioenergetics Pathways Underlying T Cell Activation.* Immunity, 2017. **46**(3): p. 488-503.
21. Allman, D., et al., *BCL-6 expression during B-cell activation.* Blood, 1996. **87**(12): p. 5257-68.
22. Li, X., et al., *Cbl Ubiquitin Ligases Control B Cell Exit from the Germinal-Center Reaction.* Immunity, 2018. **48**(3): p. 530-541 e6.

23. Gerstberger, S., M. Hafner, and T. Tuschl, *A census of human RNA-binding proteins.* Nat Rev Genet, 2014. **15**(12): p. 829-45.
24. Hentze, M.W., et al., *A brave new world of RNA-binding proteins.* Nat Rev Mol Cell Biol, 2018. **19**(5): p. 327-341.
25. Grenov, A., et al., *YTHDF2 suppresses the plasmablast genetic program and promotes germinal center formation.* Cell Rep, 2022. **39**(5): p. 110778.
26. Huang, H., et al., *Mettl14-Mediated m6A Modification Is Essential for Germinal Center B Cell Response.* J Immunol, 2022. **208**(8): p. 1924-1936.
27. Diaz-Munoz, M.D., et al., *The RNA-binding protein HuR is essential for the B cell antibody response.* Nat Immunol, 2015. **16**(4): p. 415-25.
28. Monzon-Casanova, E., et al., *The RNA-binding protein PTBP1 is necessary for B cell selection in germinal centers.* Nat Immunol, 2018. **19**(3): p. 267-278.
29. Osma-Garcia, I.C., et al., *The RNA binding proteins TIA1 and TIAL1 promote Mcl1 mRNA translation to protect germinal center responses from apoptosis.* Cell Mol Immunol, 2023. **20**(9): p. 1063-1076.
30. Chang, X., B. Li, and A. Rao, *RNA-binding protein hnRNPLL regulates mRNA splicing and stability during B-cell to plasma-cell differentiation.* Proc Natl Acad Sci U S A, 2015. **112**(15): p. E1888-97.
31. Huang, H., et al., *The RNA-binding protein hnRNP F is required for the germinal center B cell response.* Nat Commun, 2023. **14**(1): p. 1731.
32. Lin, S., et al., *Comparison of the transcriptional landscapes between human and mouse tissues.* Proc Natl Acad Sci U S A, 2014. **111**(48): p. 17224-9.
33. Wang, D., et al., *A deep proteome and transcriptome abundance atlas of 29 healthy human tissues.* Mol Syst Biol, 2019. **15**(2): p. e8503.
34. Holmes, A.B., et al., *Single-cell analysis of germinal-center B cells informs on lymphoma cell of origin and outcome.* J Exp Med, 2020. **217**(10).
35. Heraud-Farlow, J.E. and M.A. Kiebler, *The multifunctional Staufen proteins: conserved roles from neurogenesis to synaptic plasticity.* Trends Neurosci, 2014. **37**(9): p. 470-9.
36. Masliah, G., P. Barraud, and F.H. Allain, *RNA recognition by double-stranded RNA binding domains: a matter of shape and sequence.* Cell Mol Life Sci, 2013. **70**(11): p. 1875-95.
37. Ramasamy, S., et al., *Zebrafish Staufen1 and Staufen2 are required for the survival and migration of primordial germ cells.* Dev Biol, 2006. **292**(2): p. 393-406.
38. Bilogan, C.K. and M.E. Horb, *Xenopus staufen2 is required for anterior endodermal organ formation.* Genesis, 2012. **50**(3): p. 251-9.
39. Buchner, G., et al., *Identification of a novel homolog of the Drosophila staufen protein in the chromosome 8q13-q21.1 region.* Genomics, 1999. **62**(1): p. 113-8.
40. Monshausen, M., et al., *Two rat brain staufen isoforms differentially bind RNA.* J Neurochem, 2001. **76**(1): p. 155-65.
41. Duchaine, T.F., et al., *Staufen2 isoforms localize to the somatodendritic domain of neurons and interact with different organelles.* J Cell Sci, 2002. **115**(Pt 16): p. 3285-95.
42. Mallardo, M., et al., *Isolation and characterization of Staufen-containing ribonucleoprotein particles from rat brain.* Proc Natl Acad Sci U S A, 2003. **100**(4): p. 2100-5.
43. Belanger, G., et al., *Localization of the RNA-binding proteins Staufen1 and Staufen2 at the mammalian neuromuscular junction.* J Neurochem, 2003. **86**(3): p. 669-77.
44. Thomas, M.G., et al., *Staufen recruitment into stress granules does not affect early mRNA transport in oligodendrocytes.* Mol Biol Cell, 2005. **16**(1): p. 405-20.
45. Furic, L., M. Maher-Laporte, and L. DesGroseillers, *A genome-wide approach identifies distinct but overlapping subsets of cellular mRNAs associated with Staufen1- and Staufen2-containing ribonucleoprotein complexes.* RNA, 2008. **14**(2): p. 324-35.
46. Goetze, B., et al., *The brain-specific double-stranded RNA-binding protein Staufen2 is required for dendritic spine morphogenesis.* J Cell Biol, 2006. **172**(2): p. 221-31.

47. Vessey, J.P., et al., *A loss of function allele for murine Staufen1 leads to impairment of dendritic Staufen1-RNP delivery and dendritic spine morphogenesis.* Proc Natl Acad Sci U S A, 2008. **105**(42): p. 16374-9.
48. Kim, Y.K., et al., *Staufen1 regulates diverse classes of mammalian transcripts.* EMBO J, 2007. **26**(11): p. 2670-81.
49. Gowravaram, M., et al., *Insights into the assembly and architecture of a Staufen-mediated mRNA decay (SMD)-competent mRNP.* Nat Commun, 2019. **10**(1): p. 5054.
50. Kim, Y.K., et al., *Mammalian Staufen1 recruits Upf1 to specific mRNA 3'UTRs so as to elicit mRNA decay.* Cell, 2005. **120**(2): p. 195-208.
51. Park, E., M.L. Gleghorn, and L.E. Maquat, *Staufen2 functions in Staufen1-mediated mRNA decay by binding to itself and its paralog and promoting UPF1 helicase but not ATPase activity.* Proc Natl Acad Sci U S A, 2013. **110**(2): p. 405-12.
52. Park, E. and L.E. Maquat, *Staufen-mediated mRNA decay.* Wiley Interdiscip Rev RNA, 2013. **4**(4): p. 423-35.
53. Bonam, S.R., M. Ruff, and S. Muller, *HSPA8/HSC70 in Immune Disorders: A Molecular Rheostat that Adjusts Chaperone-Mediated Autophagy Substrates.* Cells, 2019. **8**(8).
54. Maher-Laporte, M., et al., *Molecular composition of staufen2-containing ribonucleoproteins in embryonic rat brain.* PLoS One, 2010. **5**(6): p. e11350.
55. Macchi, P., et al., *The brain-specific double-stranded RNA-binding protein Staufen2: nucleolar accumulation and isoform-specific exportin-5-dependent export.* J Biol Chem, 2004. **279**(30): p. 31440-4.
56. Miki, T. and Y. Yoneda, *Alternative splicing of Staufen2 creates the nuclear export signal for CRM1 (Exportin 1).* J Biol Chem, 2004. **279**(46): p. 47473-9.
57. Monshausen, M., N.H. Gehring, and K.S. Kosik, *The mammalian RNA-binding protein Staufen2 links nuclear and cytoplasmic RNA processing pathways in neurons.* Neuromolecular Med, 2004. **6**(2-3): p. 127-44.
58. Fritzsche, R., et al., *Interactome of two diverse RNA granules links mRNA localization to translational repression in neurons.* Cell Rep, 2013. **5**(6): p. 1749-62.
59. Sharangdhar, T., et al., *A retained intron in the 3'-UTR of Calm3 mRNA mediates its Staufen2- and activity-dependent localization to neuronal dendrites.* EMBO Rep, 2017. **18**(10): p. 1762-1774.
60. Bartkowska, K., et al., *Roles of the exon junction complex components in the central nervous system: a mini review.* Rev Neurosci, 2018. **29**(8): p. 817-824.
61. Elvira, G., B. Massie, and L. DesGroseillers, *The zinc-finger protein ZFR is critical for Staufen 2 isoform specific nucleocytoplasmic shuttling in neurons.* J Neurochem, 2006. **96**(1): p. 105-17.
62. Katahira, J., *Nuclear export of messenger RNA.* Genes (Basel), 2015. **6**(2): p. 163-84.
63. Krichevsky, A.M. and K.S. Kosik, *Neuronal RNA granules: a link between RNA localization and stimulation-dependent translation.* Neuron, 2001. **32**(4): p. 683-96.
64. Jeong, J.H., et al., *The transport of Staufen2-containing ribonucleoprotein complexes involves kinesin motor protein and is modulated by mitogen-activated protein kinase pathway.* J Neurochem, 2007. **102**(6): p. 2073-2084.
65. Nam, Y.J., et al., *Role of mitogen-activated protein kinase (MAPK) docking sites on Staufen2 protein in dendritic mRNA transport.* Biochem Biophys Res Commun, 2008. **372**(4): p. 525-9.
66. Miki, T., et al., *Cell type-dependent gene regulation by Staufen2 in conjunction with Upf1.* BMC Mol Biol, 2011. **12**: p. 48.
67. Graber, T.E., et al., *UPF1 Governs Synaptic Plasticity through Association with a STAU2 RNA Granule.* J Neurosci, 2017. **37**(38): p. 9116-9131.
68. Lebeau, G., et al., *Staufen 2 regulates mGluR long-term depression and Map1b mRNA distribution in hippocampal neurons.* Learn Mem, 2011. **18**(5): p. 314-26.
69. Kobayashi, H. and Y. Tomari, *RISC assembly: Coordination between small RNAs and Argonaute proteins.* Biochim Biophys Acta, 2016. **1859**(1): p. 71-81.

70. Laver, J.D., et al., *Genome-wide analysis of Staufen-associated mRNAs identifies secondary structures that confer target specificity.* Nucleic Acids Res, 2013. **41**(20): p. 9438-60.
71. Heraud-Farlow, J.E., et al., *Staufen2 regulates neuronal target RNAs.* Cell Rep, 2013. **5**(6): p. 1511-8.
72. Oh, J.Y., et al., *Apolipoprotein E mRNA is transported to dendrites and may have a role in synaptic structural plasticity.* J Neurochem, 2010. **114**(3): p. 685-96.
73. Bauer, K.E., et al., *Live cell imaging reveals 3'-UTR dependent mRNA sorting to synapses.* Nat Commun, 2019. **10**(1): p. 3178.
74. Konig, J., et al., *iCLIP reveals the function of hnRNP particles in splicing at individual nucleotide resolution.* Nat Struct Mol Biol, 2010. **17**(7): p. 909-15.
75. Van Nostrand, E.L., S.C. Huelga, and G.W. Yeo, *Experimental and Computational Considerations in the Study of RNA-Binding Protein-RNA Interactions.* Adv Exp Med Biol, 2016. **907**: p. 1-28.
76. Ortiz, R., et al., *Recruitment of Staufen2 Enhances Dendritic Localization of an Intron-Containing CaMKIIalpha mRNA.* Cell Rep, 2017. **20**(1): p. 13-20.
77. Sugimoto, Y., et al., *hiCLIP reveals the in vivo atlas of mRNA secondary structures recognized by Staufen 1.* Nature, 2015. **519**(7544): p. 491-4.
78. Zhang, X., et al., *The downregulation of the RNA-binding protein Staufen2 in response to DNA damage promotes apoptosis.* Nucleic Acids Res, 2016. **44**(8): p. 3695-712.
79. Maher-Laporte, M. and L. DesGroseillers, *Genome wide identification of Staufen2-bound mRNAs in embryonic rat brains.* BMB Rep, 2010. **43**(5): p. 344-8.
80. Beaujois, R., et al., *The M-phase specific hyperphosphorylation of Staufen2 involved the cyclin-dependent kinase CDK1.* BMC Cell Biol, 2017. **18**(1): p. 25.
81. Vessey, J.P., et al., *An asymmetrically localized Staufen2-dependent RNA complex regulates maintenance of mammalian neural stem cells.* Cell Stem Cell, 2012. **11**(4): p. 517-28.
82. Cockburn, D.M., et al., *The double-stranded RNA-binding protein Staufen 2 regulates eye size.* Mol Cell Neurosci, 2012. **51**(3-4): p. 101-11.
83. Bajaj, J., et al., *An in vivo genome-wide CRISPR screen identifies the RNA-binding protein Staufen2 as a key regulator of myeloid leukemia.* Nature Cancer, 2020. **1**(4): p. 410-422.
84. Almasi, S., et al., *Differential regulation of autophagy by STAU1 in alveolar rhabdomyosarcoma and non-transformed skeletal muscle cells.* Cell Oncol (Dordr), 2021. **44**(4): p. 851-870.
85. Petryszak, R., et al., *Expression Atlas update--an integrated database of gene and protein expression in humans, animals and plants.* Nucleic Acids Res, 2016. **44**(D1): p. D746-52.
86. Hennrich, M.L., et al., *Cell-specific proteome analyses of human bone marrow reveal molecular features of age-dependent functional decline.* Nat Commun, 2018. **9**(1): p. 4004.
87. White, J.K., et al., *Genome-wide generation and systematic phenotyping of knockout mice reveals new roles for many genes.* Cell, 2013. **154**(2): p. 452-64.
88. Kranz, A., et al., *An improved Flp deleter mouse in C57Bl/6 based on Flpo recombinase.* Genesis, 2010. **48**(8): p. 512-20.
89. Kim, K.J., et al., *Establishment and characterization of BALB/c lymphoma lines with B cell properties.* J Immunol, 1979. **122**(2): p. 549-54.
90. Laskov, R. and M.D. Scharff, *Synthesis, assembly, and secretion of gamma globulin by mouse myeloma cells. I. Adaptation of the Merwin plasma cell tumor-11 to culture, cloning, and characterization of gamma globulin subunits.* J Exp Med, 1970. **131**(3): p. 515-41.
91. Oi, V.T., et al., *Immunoglobulin gene expression in transformed lymphoid cells.* Proc Natl Acad Sci U S A, 1983. **80**(3): p. 825-9.
92. Meixlsperger, S., et al., *Conventional light chains inhibit the autonomous signaling capacity of the B cell receptor.* Immunity, 2007. **26**(3): p. 323-33.

93. Jack, R.S., T. Imanishi-Kari, and K. Rajewsky, *Idiotypic analysis of the response of C57BL/6 mice to the (4-hydroxy-3-nitrophenyl)acetyl group.* Eur J Immunol, 1977. **7**(8): p. 559-65.
94. Imanishi-Kari, T., et al., *Lymphocyte Hybridomas, Second Workshop on "Functional Properties of Tumors of T and B Lymphocytes".* Current topics in microbiology and immunology, 1979. **81**: p. 20-26.
95. Heise, N. and U. Klein, *Germinal Centers, Methods and Protocols.* Methods in Molecular Biology, 2017. **1623**: p. 191-208.
96. Doench, J.G., et al., *Optimized sgRNA design to maximize activity and minimize off-target effects of CRISPR-Cas9.* Nat Biotechnol, 2016. **34**(2): p. 184-191.
97. Tzelepis, K., et al., *A CRISPR Dropout Screen Identifies Genetic Vulnerabilities and Therapeutic Targets in Acute Myeloid Leukemia.* Cell Rep, 2016. **17**(4): p. 1193-1205.
98. Gross, A., et al., *Technologies for Single-Cell Isolation.* Int J Mol Sci, 2015. **16**(8): p. 16897-919.
99. Mueller, S., et al., *Evolutionary routes and KRAS dosage define pancreatic cancer phenotypes.* Nature, 2018. **554**(7690): p. 62-68.
100. Macosko, E.Z., et al., *Highly Parallel Genome-wide Expression Profiling of Individual Cells Using Nanoliter Droplets.* Cell, 2015. **161**(5): p. 1202-1214.
101. Petkau, G., et al., *The timing of differentiation and potency of CD8 effector function is set by RNA binding proteins.* Nat Commun, 2022. **13**(1): p. 2274.
102. Heber, S., et al., *Staufen2-mediated RNA recognition and localization requires combinatorial action of multiple domains.* Nat Commun, 2019. **10**(1): p. 1659.
103. Hobeika, E., et al., *Testing gene function early in the B cell lineage in mb1-cre mice.* Proc Natl Acad Sci U S A, 2006. **103**(37): p. 13789-94.
104. Schmidt-Supprian, M. and K. Rajewsky, *Vagaries of conditional gene targeting.* Nat Immunol, 2007. **8**(7): p. 665-8.
105. Egle, A., et al., *VavP-Bcl2 transgenic mice develop follicular lymphoma preceded by germinal center hyperplasia.* Blood, 2004. **103**(6): p. 2276-83.
106. Rashbrook, V.S., J.T. Brash, and C. Ruhrberg, *Cre toxicity in mouse models of cardiovascular physiology and disease.* Nat Cardiovasc Res, 2022. **1**: p. 806-816.
107. Crane, G.M., Y.C. Liu, and A. Chadburn, *Spleen: Development, anatomy and reactive lymphoid proliferations.* Semin Diagn Pathol, 2021. **38**(2): p. 112-124.
108. San Gil, F., et al., *Flow cytometric analysis of cellular changes in mice after intradermal inoculation with a liposome-iscom adjuvanted vaccine.* Scand J Immunol, 1998. **47**(3): p. 243-53.
109. Jacob, J., et al., *In situ studies of the primary immune response to (4-hydroxy-3-nitrophenyl)acetyl. III. The kinetics of V region mutation and selection in germinal center B cells.* J Exp Med, 1993. **178**(4): p. 1293-307.
110. Jacob, J., R. Kassir, and G. Kelsoe, *In situ studies of the primary immune response to (4-hydroxy-3-nitrophenyl)acetyl. I. The architecture and dynamics of responding cell populations.* J Exp Med, 1991. **173**(5): p. 1165-75.
111. Jacob, J. and G. Kelsoe, *In situ studies of the primary immune response to (4-hydroxy-3-nitrophenyl)acetyl. II. A common clonal origin for periarteriolar lymphoid sheath-associated foci and germinal centers.* J Exp Med, 1992. **176**(3): p. 679-87.
112. Takahashi, Y., et al., *In situ studies of the primary immune response to (4-hydroxy-3-nitrophenyl)acetyl. V. Affinity maturation develops in two stages of clonal selection.* J Exp Med, 1998. **187**(6): p. 885-95.
113. Smith, K.G., et al., *The phenotype and fate of the antibody-forming cells of the splenic foci.* Eur J Immunol, 1996. **26**(2): p. 444-8.
114. Kaji, T., et al., *Distinct cellular pathways select germline-encoded and somatically mutated antibodies into immunological memory.* J Exp Med, 2012. **209**(11): p. 2079-97.
115. Kober-Hasslacher, M., et al., *c-Rel gain in B cells drives germinal center reactions and autoantibody production.* J Clin Invest, 2020. **130**(6): p. 3270-3286.

116. Feng, J., et al., *External signals regulate germinal center fate-determining transcription factors in the A20 lymphoma cell line.* Mol Immunol, 2018. **93**: p. 79-86.
117. Saito, M., et al., *A signaling pathway mediating downregulation of BCL6 in germinal center B cells is blocked by BCL6 gene alterations in B cell lymphoma.* Cancer Cell, 2007. **12**(3): p. 280-92.
118. Niu, H., B.H. Ye, and R. Dalla-Favera, *Antigen receptor signaling induces MAP kinase-mediated phosphorylation and degradation of the BCL-6 transcription factor.* Genes Dev, 1998. **12**(13): p. 1953-61.
119. Mori, H., et al., *Deficiency of the oxidative damage-specific DNA glycosylase NEIL1 leads to reduced germinal center B cell expansion.* DNA Repair (Amst), 2009. **8**(11): p. 1328-32.
120. Kiebler, M.A., et al., *A putative nuclear function for mammalian Staufen.* Trends Biochem Sci, 2005. **30**(5): p. 228-31.
121. Seong, Y., et al., *Global identification of target recognition and cleavage by the Microprocessor in human ES cells.* Nucleic Acids Res, 2014. **42**(20): p. 12806-21.
122. Huppertz, I., et al., *iCLIP: protein-RNA interactions at nucleotide resolution.* Methods, 2014. **65**(3): p. 274-87.
123. Zarnegar, B.J., et al., *irCLIP platform for efficient characterization of protein-RNA interactions.* Nat Methods, 2016. **13**(6): p. 489-92.
124. Naik, E. and V.M. Dixit, *Usp9X Is Required for Lymphocyte Activation and Homeostasis through Its Control of ZAP70 Ubiquitination and PKCbeta Kinase Activity.* J Immunol, 2016. **196**(8): p. 3438-51.
125. Shukla, V., et al., *TET deficiency perturbs mature B cell homeostasis and promotes oncogenesis associated with accumulation of G-quadruplex and R-loop structures.* Nat Immunol, 2022. **23**(1): p. 99-108.
126. Cumano, A. and K. Rajewsky, *Structure of primary anti-(4-hydroxy-3-nitrophenyl)acetyl (NP) antibodies in normal and idiotypically suppressed C57BL/6 mice.* Eur J Immunol, 1985. **15**(5): p. 512-20.
127. Bothwell, A.L., et al., *Heavy chain variable region contribution to the NPb family of antibodies: somatic mutation evident in a gamma 2a variable region.* Cell, 1981. **24**(3): p. 625-37.
128. Heise, N. and U. Klein, *Somatic Hypermutation and Affinity Maturation Analysis Using the 4-Hydroxy-3-Nitrophenyl-Acetyl (NP) System.* Methods Mol Biol, 2017. **1623**: p. 191-208.
129. Muramatsu, M., et al., *Class switch recombination and hypermutation require activation-induced cytidine deaminase (AID), a potential RNA editing enzyme.* Cell, 2000. **102**(5): p. 553-63.
130. Muto, A., et al., *The transcriptional programme of antibody class switching involves the repressor Bach2.* Nature, 2004. **429**(6991): p. 566-71.
131. Sonoda, E., et al., *B cell development under the condition of allelic inclusion.* Immunity, 1997. **6**(3): p. 225-33.
132. Jin, H.Y. and C. Xiao, *An Integrated Polysome Profiling and Ribosome Profiling Method to Investigate In Vivo Translatome.* Methods Mol Biol, 2018. **1712**: p. 1-18.
133. Petrovas, C., et al., *CD4 T follicular helper cell dynamics during SIV infection.* J Clin Invest, 2012. **122**(9): p. 3281-94.
134. Shulman, Z., et al., *T follicular helper cell dynamics in germinal centers.* Science, 2013. **341**(6146): p. 673-7.
135. Duan, L., et al., *Follicular dendritic cells restrict interleukin-4 availability in germinal centers and foster memory B cell generation.* Immunity, 2021. **54**(10): p. 2256-2272 e6.
136. Ochi, K., et al., *Non-conditioned bone marrow chimeric mouse generation using culture-based enrichment of hematopoietic stem and progenitor cells.* Nat Commun, 2021. **12**(1): p. 3568.
137. Robbiani, D.F., et al., *AID is required for the chromosomal breaks in c-myc that lead to c-myc/IgH translocations.* Cell, 2008. **135**(6): p. 1028-38.

138. Niu, H., G. Cattoretti, and R. Dalla-Favera, *BCL6 controls the expression of the B7-1/CD80 costimulatory receptor in germinal center B cells.* J Exp Med, 2003. **198**(2): p. 211-21.
139. Pang, S.H., S. Carotta, and S.L. Nutt, *Transcriptional control of pre-B cell development and leukemia prevention.* Curr Top Microbiol Immunol, 2014. **381**: p. 189-213.
140. Wohner, M., et al., *Molecular functions of the transcription factors E2A and E2-2 in controlling germinal center B cell and plasma cell development.* J Exp Med, 2016. **213**(7): p. 1201-21.
141. Minnich, M., et al., *Multifunctional role of the transcription factor Blimp-1 in coordinating plasma cell differentiation.* Nat Immunol, 2016. **17**(3): p. 331-43.
142. Obrdlik, A., et al., *The Transcriptome-wide Landscape and Modalities of EJC Binding in Adult Drosophila.* Cell Rep, 2019. **28**(5): p. 1219-1236 e11.
143. Ishimaru, D., et al., *RNA dimerization plays a role in ribosomal frameshifting of the SARS coronavirus.* Nucleic Acids Res, 2013. **41**(4): p. 2594-608.
144. Ko, P., et al., *Probing the importance of clonality: Single cell subcloning of clonally derived CHO cell lines yields widely diverse clones differing in growth, productivity, and product quality.* Biotechnol Prog, 2018. **34**(3): p. 624-634.
145. Tharmalingam, T., et al., *Characterization of phenotypic and genotypic diversity in subclones derived from a clonal cell line.* Biotechnol Prog, 2018. **34**(3): p. 613-623.